ABSTRACT

DIRECT NUMERICAL SIMULATIONS AND EXPERIMENTAL INVESTIGATION OF DIELECTROPHORESIS

by

Arun Thankamony John-Kadaksham

This dissertation deals with the numerical and experimental studies of the phenomenon of dielectrophoresis, i.e., the motion of neutral particles in nonuniform electric fields. Dielectrophoresis is the translatory motion of neutral particles suspended in a dielectric medium when they are subjected to an external nonuniform electric field. The translatory motion occurs because a force called the dielectrophoretic force, which depends on the spatial variation of the electric field, acts on the particles. As the generation of force involves no moving parts and the particles can be moved without touching them, dielectrophoresis can be used in many applications, including manipulation and separation of biological particles, manipulation of nanoparticles, etc.

In the present study, the numerical simulations of the fluid-particle system are performed using a direct numerical simulation scheme based on the distributed Lagrange multiplier method. In this scheme, the fluid flow equations are solved both inside and outside the particle boundaries and flow inside the particle boundary is forced to be a rigid body motion by using the distributed Lagrange multiplier. The electrostatic force acting on the particles is computed using the point dipole method. The scheme is used to study the behavior of particles in the suspension under the influence of a nonuniform electric field.

The numerical scheme is used to study the influence of a dimensionless parameter, which is the ratio of electrostatic particle-particle interactions and dielectrophoretic force, in the dynamics of particle structure formation and the eventual particle collection. When this parameter is of order one or greater, which corresponds to the regime where particle-particle interactions are comparable in magnitude to the dielectrophoretic force, simulations reveal that the particles form interparticle chains and the chains then move to the electrode edges in the case of positive dielectrophoresis. When this parameter is of order ten the particles collect in the form of chains extending from one electrode to the opposite one clogging the entire domain. On the other hand, when this parameter is less than order one, particles move to the electrode edges individually and agglomerate at the edges of the electrodes.

The results of numerical simulations are verified experimentally using a suspension of viable yeast cells subjected to dielectrophoresis using microelectrodes. The experiments show that at frequencies much smaller than the crossover frequency where the value of the above parameter is greater than order one, the yeast particles form chains and then move and collect at the electrode edges. Where as, at frequencies closer to the crossover frequency where the value of the parameter is less than order one, particles move individually without forming chains and agglomerate at the electrode edges.

The numerical simulation scheme is also used to study the dielectrophoresis of nanoparticles. Simulations show that in a uniform electric field the Brownian force is dominant and results in the random scattering of the particles. In the case of nonuniform electric field, it is possible to overcome the Brownian force and collect the particles at

pre-determined locations, even though the trajectories of the particles are influenced by Brownian motion.

Finally, the method of images is used to improve the electric field solution when the particles are close to the domain walls. Simulations performed for uniform electric fields with the method of images shows that when the distance between the particle and domain boundary is of the order of particle diameter the influence of the particles on the electric field boundary conditions is significant.

DIRECT NUMERICAL SIMULATIONS AND EXPERIMENTAL INVESTIGATION OF DIELECTROPHORESIS

by

Arun Thankamony John-Kadaksham

A Dissertation
Submitted to the Faculty of
New Jersey Institute of Technology
in Partial Fulfillment of the Requirements for the Degree of
Doctor of Philosophy in Mechanical Engineering

Department of Mechanical Engineering

May 2005

APPROVAL PAGE

DIRECT NUMERICAL SIMULATIONS AND EXPERIMENTAL INVESTIGATION OF DIELECTROPHORESIS

Arun Thankamony John-Kadaksham

Dr. Pushpendra Singh, Dissertation Advisor — Date
Associate Professor, Department of Mechanical Engineering, NJIT

Dr. Nadine Aubry, Co-Advisor — Date
Distinguished Professor, Department of Mechanical Engineering, NJIT

Dr. I. Joga Rao, Committee Member — Date
Assistant Professor, Department of Mechanical Engineering, NJIT

Dr. Christopher E. Elmer, Committee Member — Date
Assistant Professor, Department of Mathematical Sciences, NJIT

Dr. Moses Faynglod, Committee Member — Date
Special Lecturer, Department of Physics, NJIT

BIOGRAPHICAL SKETCH

Author: Arun Thankamony John-Kadaksham

Degree: Doctor of Philosophy

Date: May 2005

Undergraduate and Graduate Education:

- Doctor of Philosophy in Mechanical Engineering,
  New Jersey Institute of Technology, Newark, NJ, 2005
- Master of Science in Mechanical Engineering,
  New Jersey Institute of Technology, Newark, NJ, 2003
- Bachelor of Science in Mechanical Engineering,
  University of Kerala, India, 1998

Major: Mechanical Engineering

Publications:

1. Kadaksham, J., Singh, P., and Aubry, N., (2004). Dynamics of electrorheological suspensions subjected to spatially varying electric fields, Journal of Fluids Engineering, 126, 170 –179.
2. Kadaksham, J., Singh, P., and Aubry, N., (2004). Manipulation of particles using dielectrophoresis, Mechanics Research Communications, to appear.
3. Kadaksham, J., Singh, P., and Pillapakkam, S., (2004). Permeability of periodic arrays of spheres, Mechanics Research Communications, to appear.
4. Kadaksham, J., Singh, P., and Aubry, N., (2004). Dielectrophoresis of nanoparticles, Electrophoresis, 25, 3625-3632.
5. Kadaksham, J., Singh, P., and Aubry, N., (2004). Dielectrophoresis induced clustering regimes of viable yeast cells, Electrophoresis, to appear.
6. Kadaksham, J., Singh, P. and Aubry, N., (2005), Simulation of Multi-particle interactions in electrorheological fluids using the method of images, Manuscript in preparation.
7. Kadaksham, J., Singh, P., and Aubry, N., (2002). Particle structure evolution in microflow of electrorheological suspensions in nonuniform electric fields, American

Society of Mechanical Engineers, Fluids Engineering Division (Publication), FED 258.

8. Kadaksham, J., Singh, P., and Aubry, N., (2002). Direct simulation of electrorheological suspensions subjected to spatially nonuniform electric field, American Society of Mechanical Engineers, Fluids Engineering Division (Publication) FED 258, 221-226.
9. Kadaksham, J., Batton, J., Singh, P., and Aubry, N., (2003). Micro fluidic platform for the manipulation of micro and nanoscale particles, American Society of Mechanical Engineers, EEP 3, 835-840.
10. Kadaksham, J., Singh, P., and Aubry, N., (2003). Particle separation using dielectrophoresis, American Society of Mechanical Engineers, Fluids Engineering Division (Publication) FED 259, 45-49.
11. Kadaksham, J., Batton, J., Singh, P., and Aubry, N., (2003). Particle structure evolution in micro flow of electrorheological suspensions in nonuniform electric fields, Proceedings of the ASME/JSME Joint Fluids Engineering Conference 2C, 2411-2416.
12. Kadaksham, J., Batton, J., Singh, P., Golubovic-Liakopoulos, N. and Aubry, N., (2003). Dielectrophoretic manipulation of micro- and nanoscale particles in microchannels, Nanotechnology World Forum, 2003, Marlborough, Massachusetts, June 23 – 25.
13. Kadaksham, J., Singh, P., and Aubry, N., (2004). Dielectrophoresis of nanoparticles, Proceedings of ASME International Mechanical Engineering Conference and RD&D Expo, Anaheim, California, USA, November 13-19.
14. Batton, J., Kadaksham, J., Nzihou, A., Singh, P., and Aubry, N., (2005). Preconcentration of heavy metals adsorbed in hydroxyapatite particles using a dielectrophoretic micro-device, Proceedings of Wasteeng 05: Conference on engineering for waste treatment.

Conference Presentations:

1. Kadaksham, J., Singh, P., and Aubry, N., (2002). Dynamics of electrorheological suspensions subjected to spatially nonuniform electric fields, 14th US National Congress of Theoretical and Applied Mechanics Proceedings, Virginia Polytechnic Institute and State University, Blacksburg, VA, June 23-28.
2. Kadaksham, J., Singh, P., and Aubry, N., (2002). Direct simulation of electrorheological suspensions subjected to spatially non uniform electric field, American Physical Society, Division of Fluid Dynamics, 55th Annual Meeting.
3. Kadaksham, J., Singh, P., and Aubry, N., (2003). Separation of micron sized particles using dielectrophoresis, 56th Annual Meeting of the Division of Fluid Dynamics, American Physical Society, Nov. 23-25, 2003, New Jersey.
4. Kadaksham, J., Singh, P., and Aubry, N., (2004). Electrorheological suspensions of Brownian particles, 57th Annual Meeting of the Division of Fluid Dynamics, Nov. 21-23, 2004, Seattle, WA.

To

My wife and parents

ACKNOWLEDGEMENT

I would like to express my thanks and appreciation to Dr. Pushpendra Singh, Associate Professor, Department of Mechanical Engineering at NJIT, for all his help and guidance over the duration of my graduate program and for paving the way for my future success.

I would like to express my gratitude to Dr. Nadine Aubry, Distinguished Professor and Chair of the Department of Mechanical Engineering, for her encouragement in my numerical and experimental work, and the number of opportunities she has provided me for the presentation of my efforts at conferences.

I also extend my thanks to Dr. I. Joga Rao, Assistant Professor, Department of Mechanical Engineering, NJIT, Dr. Christopher E. Elmer, Assistant Professor, Department of Mathematical Sciences, NJIT and Dr. Moses Fayngold, Special Lecturer, Department of Physics, NJIT for taking interest in my research and contributing to its success.

I would also like to thank John Batton and George Barnes at the New Jersey Center for Micro Flow Control, NJIT. Without their help my experimental research would have remained unfinished.

This research was supported by the National Science Foundation KDI Grand Challenge grant (NSF/CTS-98-73236), the New Jersey Commission on Science and Technology through the New-Jersey Center for Micro-Flow Control under Award Number 01-2042-007-25, the W.M. Keck Foundation by providing support for the establishment of the NJIT Keck laboratory for Electrohydrodynamics of Suspensions and the Office of Naval Research under Award Number 992294.

TABLE OF CONTENTS

Chapter **Page**

TABLE OF CONTENTS
(Continued)

Chapter **Page**

CHAPTER 1

INTRODUCTION

The aim of this research is to study the motion of electrically neutral particles suspended in a liquid in uniform and spatially varying electric fields. The suspended particles become polarized and interact with each other electrostatically, and also with the applied electric field when the electric field is spatially varying. The electrostatic interaction with the spatially varying electric field results in a force to act on the suspended particles. This force is called the dielectrophoretic (DEP) force and the phenomenon is called dielectrophoresis. The dielectrophoretic force results in a translational motion of the particle. The magnitude and direction of the force experienced by the particle depends on the strength and spatial variation of the applied electric field.

The study of dielectrophoresis is important, as it can be used for a variety of practical applications. Some of the applications include filtration of fluids, separation of particles with different polarizabilities, manipulation of nanoparticles, and lab-on-a-chip type applications. One of the features that make dielectrophoresis a good particle manipulation force is the fact that there are no moving parts involved and the particles can be moved without touching them. This makes the force a suitable one for manipulating biological particles in various applications such as cell sorting, cell lysing, cell fusion etc.

Before moving into the details of the numerical simulations and the results of simulations and experiments, let us get familiarized with the basics of the theory of

dielectrophoresis and see how the force can be efficiently used for particle manipulation in practical devices.

1.1 Theory of Dielectrophoresis

As discussed before, a polarizable particle suspended in a nonuniform electric field experiences a force called the dielectrophoretic force due to the interaction between the electric field and the induced dipole moment. The resulting translational motion of the particle is referred to as dielectrophoresis. The direction of motion is either towards the region of maximum electric field in the case where the particle is more polarizable than the suspending medium or towards the region of minimum electric field in the case where the particle is less polarizable than the medium. The direction of the force remains the same even if the polarity of the external field is reversed as the direction depends only on the magnitude of the electric field (see Figure 1.1). Consequently, the DEP force also acts in an AC electric field. But, as discussed later, the magnitude of the force depends on the rms value of the electric field.

The above behavior of a neutral particle in a spatially varying electric field has to be distinguished from that of a charged particle in an electric field. In the case of a charged particle, the particle will always move to the electrodes having the opposite polarity. Therefore, if the polarity of the external electric field is reversed, the direction of motion of a charged particle will also be reversed. This motion of a charged particle is termed "*electrophoresis.*"

Electrorheological (ER) suspensions are suspensions whose properties can be altered by the application of an electric field. It is well known that when an ER liquid is

subjected to a spatially uniform electric field the particles form chains and columns that align parallel to the electric field direction [1]. The effective viscosity of the ER suspension increases dramatically because the length of these chains and columns can be of the same order as the gap between the electrodes, and their distribution on the planes perpendicular to the electric field direction is approximately uniform.

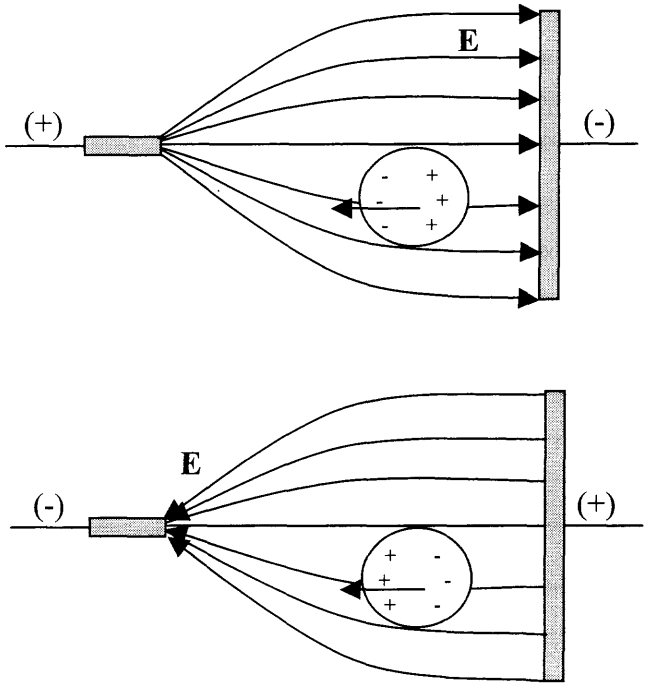

Figure 1.1 A schematic of the dielectrophoretic force acting on a neutral particle in the case of positive dielectrophoresis. The particle being neutral gets polarized with equal amount of charge at both ends. However, the dielectrophoretic force depends on the spatial variation of the electric field, and therefore a net force acts in the direction of more intense electric field. The direction of force remains the same even if the field is reversed.
The above picture is taken from "Dielectrophoresis," Pohl, H.A., Cambridge University Press.

In spatially varying electric fields, on the other hand, the particles collect either near the local maxima or local minima of the electric field magnitude because of an electrostatic force, which depends on the gradient of the electric field that acts on the particles [2, 3]. Since, in a nonuniform electric field no domain sized structures are

formed, the change in the effective viscosity of the ER suspension is relatively small. The electrostatic forces exerted by a nonuniform electric field on the particles of the suspension can be effectively utilized in various applications such as filtration of dirty fluids, manipulation of biological cells in micro total analysis systems, and separation of different kinds of cells, etc.

The polarized particle can be approximated by a dipole placed at the centre of the particle when the length scale of the spatial variation of the external electric field is much greater than the particle size. Then the dielectrophoretic force experienced by the dipole of dipole moment **m**, in a nonuniform electric field is given by:

$$\mathbf{F}_{DEP} = \mathbf{m} \cdot \nabla \mathbf{E} \tag{1.1}$$

where **m** is the dipole moment of the particle and **E** is the electric field. In arriving at Equation (1.1), only the dipole contribution is taken into account without considering the quadrupole and the other higher-order terms.

If the dipole is replaced by a dielectric sphere of radius a and permittivity ε_p, at the same position as the dipole, then the dielectrophoretic force on the dielectric sphere in a dielectric medium is given by:

$$\mathbf{F}_{DEP} = 4\pi a^3 \varepsilon_0 \varepsilon_c \beta \mathbf{E} \cdot \nabla \mathbf{E} \tag{1.2}$$

where a is the particle radius, ε_c is the permittivity of the fluid, $\varepsilon_0 = 8.8542\text{x}10^{-12}$ F/m is the permittivity of free space and **E** is the electric field, β is the real part of the complex frequency dependent Clausius-Mossotti factor $\dfrac{\varepsilon_p^* - \varepsilon_c^*}{\varepsilon_p^* + 2\varepsilon_c^*}$, i.e., $\beta(f) = \mathrm{Re}\left(\dfrac{\varepsilon_p^* - \varepsilon_c^*}{\varepsilon_p^* + 2\varepsilon_c^*}\right)$,

ε_p^* and ε_c^* being the complex permittivity of the particles and the fluid, and $\varepsilon^* = \varepsilon - j\frac{\sigma}{f}$,

where σ is the conductivity, ε is the permittivity and f is the angular frequency of the applied electric field.

The value of β is limited in the range -0.5 to 1.0 and it takes negative values when the dielectric constant of the suspending fluid is greater than that of the particles and takes positive values when the dielectric constant of the suspending fluid is less than that of the particles. Since β is frequency dependent, it is possible in theory for every fluid particle system that is not a perfect dielectric system, to have a frequency at which β goes to zero. This frequency at which the Clausius-Mossotti factor, β, is zero is called the crossover frequency (see Figure 1.2). At frequencies above and below the crossover frequency β will have opposite signs.

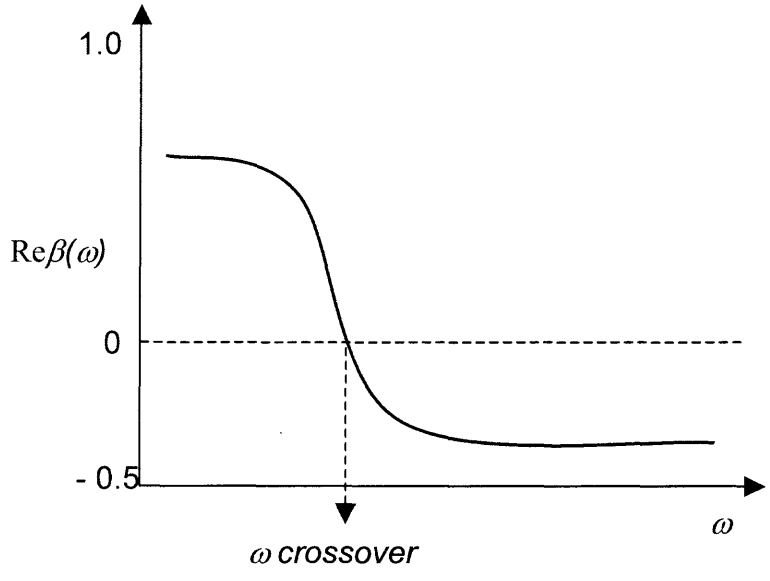

Figure 1.2 A typical curve for Clausius-Mossotti factor, showing the crossover frequency.

From the expression for the dielectrophoretic force we also notice that when β is positive the direction of the dielectrophoretic force is along the gradient of the electric field magnitude and when β is negative, the force acts in the opposite direction. In the simulations, it is assumed that both fluid and suspended particles are nonconductive or ideal dielectrics. Notice that in this case the Clausius-Mossotti factor is real as the conductivities of both mediums are zero. The equations used in such a case are however applicable even for lossy dielectrics, provided the frequency of the applied AC electric field is sufficiently large such that $\varepsilon >> \frac{\sigma}{f}$.

It follows that the direction of the dielectrophoretic force determines the regions in which the particles collect. For example, when β is positive, the dielectrophoretic force moves the particles into the regions where the electric field strength is locally maximum which is normally on the electrode surfaces, while when β is negative, it moves the particles into the regions where the electric field strength is locally minimum. The dielectrophoretic force, therefore, makes the particle distribution less uniform and thus, as mentioned above, can have a dramatic impact on the particle scale suspension structure. Such a force can also be used for removing particles from a suspending liquid, as well as for separating particles for which the sign of β is different. For a given particle, the sign of β depends on the dielectric constant of the fluid, as well as the frequency of the applied AC field. Therefore, at least in principle, any two sets of particles with different dielectric constants can be separated, provided a suitable fluid is used, such that the sign of β for them is different.

The polarized particles of a suspension are not only subjected to the applied external electric field, but also interact with each other electrostatically. These electrostatic interparticle interactions appear in the form of bunching effect holding the particles in the form of long chains. These interparticle attractions are sometimes referred to as *'mutual dielectrophoresis'* in the literature. The mutual dielectrophoresis arises because the particles which have a different polarizability than the medium distort the electric field around them. Each particle therefore experiences a nonuniform electric field near the other and is attracted to the regions of high electric field intensity near each other, resulting in particle bunches or chains.

This interaction among particles can be of the same order as the dielectrophoretic force when particles are close to each other, as is the case when they collect in the high or in the low electric field regions.

Thus, the total electrostatic force acting on the i^{th} particle $\mathbf{F}_{E,i}$, is given by the sum of these two forces,

$$\mathbf{F}_{E,i} = \mathbf{F}_{DEP,i} + \mathbf{F}_{D,i} \tag{1.3}$$

where $\mathbf{F}_{DEP,i} = 4\pi a^3 \varepsilon_0 \varepsilon_c \beta \mathbf{E}_i \cdot \nabla \mathbf{E}_i$ is the DEP force acting on the i^{th} particle and $\mathbf{F}_{D,i}$ is the net electrostatic particle interaction force acting on the i^{th} particle, given by $\mathbf{F}_{D,i} = \sum_{i=1, i\neq j}^{N} \mathbf{F}_{D,ij}$. Here, within the framework of the point dipole approximation

$$\mathbf{F}_{D,ij} = \frac{1}{4\pi\varepsilon_0\varepsilon_c}\frac{3}{r^5}\left(\mathbf{r}_{ij}\left(\mathbf{p}_i \cdot \mathbf{p}_j\right) + \left(\mathbf{r}_{ij} \cdot \mathbf{p}_i\right)\mathbf{p}_j + \left(\mathbf{r}_{ij} \cdot \mathbf{p}_j\right)\mathbf{p}_i - \frac{5}{r^2}\mathbf{r}_{ij}\left(\mathbf{p}_i \cdot \mathbf{r}_{ij}\right)\left(\mathbf{p}_j \cdot \mathbf{r}_{ij}\right)\right), \tag{1.4}$$

where $\mathbf{p}_i$ denotes the dipole moment of particle i. Notice that $F_{D,ij}$ varies inversely as the fourth power of the distance between the particles.

As already noted, the direction of the dielectrophoretic force is independent of the sign of the applied electric field, making it a versatile force in the manipulation of particles. The force would be most prominent in low viscous suspensions having large difference in the dielectric constants of the fluid and the particle.

However, dielectrophoresis as a deterministic force has a few drawbacks. The dielectrophoretic force is proportional to the volume of the particle and therefore as the size of the particle decreases, the effect also decreases, making it difficult to manipulate smaller sized particles. Also, as the size of the particles decreases, the intensity of Brownian motion increases, making it difficult to manipulate particles through pre determined trajectories. The effect of Brownian motion was first thought to overcome any deterministic motion due to the dielectrophoretic force on sub micrometer particles [3] and the minimum particle size required for dielectrophoretic motion was estimated to be around 4000–6000 $\mathring{A}$ under reasonable physical conditions.

Also, for the dielectrophoretic force to be effective, it requires a quite divergent electric field. The electric field strength required for the effective manipulation of particles is also quite high usually in the range of 10^4 V/m.

Until recently, the above constraints limited the minimum radius of the particles that could be manipulated by dielectrophoresis to 1μm [4]. With the advent of MEMS manufacturing processes, it is now possible to manufacture microelectrodes capable of generating high divergent electric fields capable of manipulating sub micrometer particles. Recent experimental observations in such devices, that have been possible due to advances in microfabrication and optical techniques, have demonstrated that the force required to produce a deterministic motion of the particles capable of overcoming the

Brownian force is much lower than that previously estimated based on rough diffusion arguments [3]. For example, it has been demonstrated that the force required to manipulate Herpes simplex virus in a microelectrode array is in the range $1 - 2 \times 10^{-14}$ N [5]. Such results have led to a renewed interest in the dielectrophoretic manipulation of small particles such as viruses, DNA, latex spheres, etc. [5-8]. The renewed interest in dielectrophoresis is mainly due to the ability to manipulate biological particles and other biotechnology related applications.

Dielectrophoresis is now widely used for cell manipulation, cell lysing, cell sorting and cell fusion applications. One of the dielectrophoretic devices used for the manipulation of cells is a dielectrophoretic trap or "cage" [9]. The DEP traps are used to capture and position single cells for further manipulation. They can be either positive DEP traps attracting cells towards the electrodes, or negative DEP traps pushing cells away from the electrodes towards regions of low magnitude of electric field. Negative DEP traps are more desirable as they involve no touching of the cells during the manipulation process. Two of the popular negative DEP cages are the quadrupole cage and the octupole cage.

Even though, there had been a lot of experimental research in the past on the phenomena of dielectrophoresis, and a number of dielectrophoretic devices and applications have been developed, there exist no thorough numerical simulation studies of the phenomena in the past. Some of the major problems encountered in experiments are the visualization of the movement of particles in the microdevices and the isolation of particle movements due to dielectrophoresis. It is well established now that the particles undergoing dielectrophoresis in microdevices are also subjected to a number of other

forces that results in observable and deterministic particle motion [10]. Numerical simulations are important especially in the case of manipulation of micro and nanoscale particles because it helps to study the particle dynamics and to isolate the effects of dielectrophoresis from that of other forces that may be present in the dielectrophoretic devices. Numerical simulations also help to predict the behavior of particles under various physical conditions, which in turn help to better understand the phenomena and also in better design of the devices. Keeping this in mind, a direct numerical simulation method has been developed to study the phenomena of dielectrophoresis, which involves solving an initial value problem of a fluid-particle system. In the next section, the reasons for choosing a direct simulation scheme and the basics of the simulation technique are discussed in detail.

In order to investigate the problem numerically, a direct numerical simulation (DNS) scheme based on the distributed Lagrange multiplier (DLM) method is used [11]. The numerical simulation scheme is mainly used to study the motion of particles under the action of a nonuniform applied electric field. However, it is also applied to study the behavior of particles under pressure driven flows, uniform electric fields and also Brownian force.

Experimental studies are also performed to verify the results obtained from numerical simulations. The experimental studies are performed in microelectrodes fabricated using MEMS manufacturing processes and using live yeast cells suspended in deionized water. Comparisons are drawn between the results of the numerical simulations and the experiments, and different regimes are identified for the effective manipulation of the particles for various applications.

The rest of the manuscript is organized as follows. In the next section, a review of the literature that talks about the immense research, that has been done and also ongoing, in the area of dielectrophoresis is presented. In the second chapter the governing equations for the system and the nondimensional analysis and the dimensionless parameters of importance that arise out of the analysis are described. In the third chapter the finite element method used is described, and the time-discretization using the Marchuk-Yanenko operator splitting technique is explained. In the fourth chapter some of the interesting results of the numerical simulations are presented. Fifth chapter compares the results of experiments performed using yeast suspension to that of the numerical simulations. The sixth chapter deals entirely about the numerical simulation of dielectrophoresis of nanoparticles. The conclusions derived from the numerical and experimental research is presented in the last chapter.

1.2 Literature Review

The study of nonuniform electric field deserves special interest because of the unique effects it can produce, and the variety of applications it can be used for. Applications such as pumping of fluids, classification and separation of minerals, removal of particulate matter from liquid suspensions, classification of microorganisms, self-assembly of nanoparticles etc. are just to name a few.

The first experimental recordings of the effect of nonuniform electric field on neutral matter can be dated back to 600 B.C when Thales of Miletus in Turkey noted that amber when rubbed attracted small light particles. We now know that this attractive force arises because amber when rubbed gets electrically charged, and when this electrically

charged amber is brought near small neutral particles, they in turn get polarized and gets attracted by the nonuniform electric field existing around amber. This is indeed, "*dielectrophoresis*."

More serious experimental studies on dielectrophoresis and its applications were performed only during the second half of the last century. This was mainly done by Herbert A. Pohl [3], whose book "Dielectrophoresis," published by Cambridge University Press is one of the pioneering works and serves as a guide to all the research on dielectrophoresis conducted today. His book deals with the theory of dielectrophoresis based on the polarization of matter. The book also explains in detail the various mechanisms of polarization in neutral matter and also the dielectrophoresis in real dielectrics where the conductivity of matter has to be taken into account along with the permittivity. He performed extensive experiments with colloidal suspensions and biological particles and enumerated the various factors that affect the particle separation or "yield" during dielectrophoresis

If we examine the research that has been conducted before 1980's, it can be observed that the bulk of the research was on the manipulation of biological cells. For example, Chen, C.S. and Pohl, H.A examined the behavior of single cells under dielectrophoresis [12]. Gvozdiak, P.I., and Chekhovckaia, T.P., studied the separation of microorganisms from water with the help of dielectrophoresis [13]. From their experiments they came to the conclusion that separation efficiency increases with increase in the applied voltage and decrease in the flow rate of the suspending fluid. Again, dielectrophoresis of cell suspensions was studied by Fomcenko et al. [14]. Fomchenkov et al. studied the dielectrophoresis of cells using optical measurements [15].

The principle of dielectrophoresis was used as a cell separation technique in [16]. Here the cells were collected on a coaxial wire electrode, which was moved at a constant rate so that the attached cells were continuously removed to a filtration chamber. In addition to the above studies on the biological cells, the dielectrophoresis of bubbles, spheres and shells were examined by Jones et al. [17, 18]

In the early half of the 1980's also, bulk of the research being conducted was on the use of dielectrophoresis for biological applications. However, now the focus was on more sophisticated applications such as cell sorting, cell lysing, cell fusion etc. [19 - 27]. Also to be mentioned is the research by Zimmermann et al. [28]. It deals with electro rotation of particles, which depends on the imaginary part of the Clausius-Mossotti factor. He used the method of electro rotation to extract the dielectric properties of particles.

A treatment of dielectrophoresis considering the particles to be lossy ones was given by Gherardi et al. and Mognaschi et al. in their papers [29] and [30] respectively. In this approach, instead of considering the particles to be pure dielectrics, their conductivity is also taken into account (which is true for a real particle) before analyzing the experimental results.

A few computational studies were also reported during this period, like the "Computer aided analysis of dielectrophoretic force calculations" by Goossens et al. [31] and "Numerical calculation of particle collection in electrically enhanced fibrous filters" by Henry et al. [32]. In the latter one, numerical investigations were performed on the particle collection efficiency of a fibrous filter. Their model took into account the effect of various forces like dielectrophoresis, electrophoresis, Brownian motion and particle

inertia and predicts the collection efficiency of the filter under the influence of these forces.

Till this period dielectrophoresis was performed using electrodes made using conventional manufacturing processes. For example, the pin-plate or the wire-wire arrangement used by Pohl in his experiments or the more sophisticated "isomotive" electrode geometry manufactured by numerically controlled milling machines, as used in [33]. The technology of manufacturing dielectrophoretic devices and therefore the research in dielectrophoresis was revolutionized by Washizu et al. [34, 35, and 36] who introduced a novel device called the "fluid integrated circuit, (FIC)." In this device all the components were integrated into a single substrate using photolithography techniques. These were the first dielectrophoretic devices manufactured using MEMS manufacturing processes. Using FIC, they were able to accurately control the electrostatic and hydrodynamic forces and therefore the manipulation of single cells. The flow channels in the device were as narrow as a little more than the diameter of the cells, so that only single cells were able to pass through it.

As already mentioned, Pohl led the way in experimental research of dielectrophoresis in the modern era. However, the devices he was using in his experiments limited his ability to explore into the manipulation of submicro and nanoscale particles; as such manipulations require strongly divergent high electric fields, which he was unable to create in his devices. This fact and the dielectric force calculations using the electric fields that existed in his devices led him to believe that dielectrophoresis will not lead to any deterministic motion in submicro and nanoscale particles, and the motion of such particles will be random governed by Brownian force.

In fact, he calculated the minimum size of the particles that could be manipulated by dielectrophoresis to be 400 – 600 μm. This belief led to a deceleration in the research and limited the applications of dielectrophoresis.

However, the development of microfabrication techniques and microelectro mechanical devices resulted in a renewed interest in dielectrophoretic manipulation of particles, as it became possible using these devices to produce accurate high gradient electric fields of large magnitude capable of manipulating submicron and nanoscale particles by applying voltages of the order 1volt.

Pethig, who was involved in biological dielectrophoresis [37, 38] was quick to cash on this new development of using microelectrodes for dielectrophoresis and designed a new microelectrode structure for biological dielectrophoresis [39, 40]. His device had interdigitated castellated microelectrode design and he used the device for the dielectrophoresis of live yeast suspension [41, 42]. Using his device he observed positive dielectrophoresis for the yeast cells above 10 kHz and negative dielectrophoresis below 500 Hz. Another important contribution by Pethig, R., and his research group was the unified studies of dielectrophoresis and electrorotation [43, 44, and 45]. Even though these two phenomena are closely related by the fact that they depend on the real and imaginary parts of the induced dipole moment respectively, the two phenomenona were investigated separately till then. He derived new theoretical relationships linking the dielectric properties of a colloidal suspension to both dielectrophoresis and electrorotation. Again, the experiments conducted for substantiating the theory were done using the interdigitated castellated microelectrode arrays newly developed.

While Pethig et al. were concentrating on the unified theory for dielectrophoresis and electro rotation; Fuhr et al. at the Department of Biology, Humboldt-University of Berlin, in Germany were investigating the phenomena of traveling wave dielectrophoresis, which is the linear analog of dielectrophoresis [46, 47, and 48]. This phenomenon was originally observed by Batchelder in 1983 [49]. In order to obtain traveling wave dielectrophoresis microelectrodes were arranged linearly with each electrode 90^{o} phase advanced than the last. This produces and electric field that travels with the electrodes and the polarized particle will also move along with this field. One has to keep in mind that this phenomenon like the electrorotation, also depends on the imaginary part of induced dipole moment. Fuhr et al. developed practical applications like micropumps using traveling wave dielectrophoresis.

Pehig et al. added their own contributions to the field of traveling wave dielectrophoresis [50, 51, 52, 53]. They used yeast particles [50] to study the phenomenon and conducted experiments in the range of frequency 1 kHz - 10 MHz and explained the dependence of the phenomenon on the dielectric properties of the particles and the suspending medium, the size of the particles, and the magnitude and frequency of the applied electric field. They found from their experiments, that the phenomenon was dependent on the imaginary component of the induced dipole moment.

The developments in the area of electro rotation and traveling wave dielectrophoresis are mentioned in this manuscript, as these forces together with dielectrophoresis and other electrokinetic forces are used for the manipulation of particles in modern dielectrophoretic devices such as micro total analysis systems and lab-on-a-chip type applications.

Another researcher who has contributed to the development of theoretical and experimental aspects of dielectrophoresis is Jones, T. B. His book "Electromagnetics of particles," [2] gives insight into the various theoretical aspects of dielectrophoresis. The conventional dielectrophoretic theory based on the dipole approximation is insufficient to explain the observed dielectrophoretic phenomena in regions of highly divergent electric field and in microchannels where the domain dimensions are comparable to that of the particle dimensions. Jones along with Washizu developed an easily interpretable dielectrophoretic theory which includes multipole terms for the dielectrophoretic force calculations [54, 55, 56]. He later on concentrated on the study of microfluidic systems like micro total analysis systems and lab-on-a-chip. These systems rely on various electrostatic forces to move small volumes of fluid samples around. His study was focused on the use of dielectrophoresis for controlling the movement of water in such devices [57]. In the past, dielectrophoretic manipulation of water was considered impossible because of the high conductivity of water and the corresponding Joule heating associated. However, in microelectrode structures the governing equations scale in such a way that the dielectrophoretic manipulation of water is possible. The scaling laws for the various electrostatic forces in a lab-on-a-chip, which is a microdevice is given in [58, 59]. He demonstrated high speed dielectrophoretic actuators including "wall-less" flow structures, siphons and nanodroplet dispensers that operate with water [60, 61].

When it comes to the contemporary research in dielectrophoresis and its applications, there are two groups that are prominent. The first one is the dielectrophoresis group at the M.D. Anderson Cancer Center at the University of Texas, Houston. The main focus of this group is to develop molecular diagnostic methods in

small clinical and research laboratory environments, primarily for cancer research, and other medical applications. One of the ongoing research interests of this group is the separation and characterization of cells. The results of dielectrophoretic characterization studies conducted in friend murine erythroleukaemic cells can be seen in reference [62]. One of the major contributions of the group was the separation of cancer cells from good cells in the blood [63, 64, 65].

They combined conventional dielectrophoresis and traveling wave dielectrophoresis in their microdevices [66], which were used for applications such as cell separation, levitation etc. A discussion of the importance of the particle-particle interactions on the pearl chain formation of particles can be seen in [67]. They also employed the Maxwell stress tensor method for the rigorous calculation of dielectrophoretic force and electrorotational torque on a homogeneous spherical dielectric particle and compared their results with that obtained from the effective moment method [68].

Traditionally, the dielectrophoretic separation of particles was done using two approaches. The first one is the DEP migration technique, which relies on the opposing polarities of the particles, by which they are separated into two regions; the high field regions in the case of particles experiencing positive dielectrophoresis, and the low field regions in the case of particles experiencing negative dielectrophoresis. The second method is the DEP retention technique in which the competition between the dielectrophoretic force and fluid flow forces is utilized to separate the particles. Here, the particles experiencing strong dielectrophoretic force will be retained at the electrode edges, where as the particles experiencing weak dielectrophoretic force will be carried

away with the flowing fluid. Both these methods require that the dielectric property difference between the different species of particles to be separated be large, and therefore it is difficult to separate particles with small dielectric differences. Huang et al. of the above group combined field flow fractionation (FFF) technique with dielectrophoretic levitation to develop a robust method for the particle separation of the latter kind [69]. FFF relies on the velocity gradient of a parabolic flow established in a thin chamber. In DEP-FFF method, dielectrophoretic levitation force is in competition with gravitational force and results in particles being positioned at different levels in the chamber, which will then be carried away at different velocities by the parabolic flow. This research, later on culminated in the development of DEP-FFF microelectrode devices for the separation of cells and particles [70, 71, 72], which was later on improved by introducing magnetophoretic force along with the other forces [73]. Presently, the group is focused in applying the various techniques developed for particle manipulation in micro total analysis systems [74] and developing programmable general-purpose sample analysis processors [75].

The second group is the Bioelectronics Research Center at the Department of Electronics and Electrical Engineering situated in the University of Glasgow. This group is mostly involved in the experimental and theoretical research of dielectrophoresis in microelectrode structures. They explore the dielectrophoresis of submicron and nanosized particles in microdevices and analyze the various forces experienced by the particles in such devices. They demonstrated the separation of submicron bioparticles and latex spheres by dielectrophoresis in microelectrodes [76], and the trapping of a single submicron bioparticle by negative dielectrophoresis against the action of Brownian force

[5]. They noted that the submicron particles undergoing dielectrophoresis in micro electrodes are not only subjected to dielectrophoretic force, but also to various other forces like Brownian force, Joule heating, electro-osmosis and electrothermal forces. These findings and the theoretical development for the AC electro-osmotic force and the relative importance of the various forces at different frequency regimes are published in various papers [77-83]. Hughes, M. P., later on studied the application of AC electrokinetics for the manipulation of nanoparticles [84].

Recently, the focus of the dielctrophoresis research is on the dielectrophoresis of nanoparticles as it can be used for the self-assembly and other manipulation of nano particles without any touching of the particles involved and also on the development of sophisticated particle handling devices such as micro total analysis systems and lab-on-a-chip.

There had been three main analytical approaches in calculating the dielectrophoretic force experienced by particles in a suspension. The first one is the energy variation principle in which the particles and the suspending medium are treated as loss free dielectrics [85, 86]. The second approach is the effective dipole method [87]. The third approach is based on the Maxwell stress tensor method, which involves the integration of the stress tensor on the entire particle surface [88, 89]. Of the above three methods, the one based on effective dipole moment of the particles is the most widely used one for practical applications, as it is easy to use and approximates the physical situation with reasonable accuracy.

When it comes to the numerical simulations of dielectrophoresis, there had been relatively few studies compared to the experimental and analytical studies. Most of these

studies are limited to the prediction of the electric field developed in the dielectrophoretic devices and the trajectories of the particle motion, without simulating the actual fluid-particle system and the particle motion [90-93]. There had been some multi particle simulation studies of dielectrophoresis in the past. However, the electrostatic particle-particle interactions were ignored and fluid particle interactions were modeled in those studies, and the simulations were conducted for negligibly small Reynold's numbers [94]. Recently, Morgan et al. conducted Brownian dynamic simulations of nanoparticle manipulation in experimental devices using 250 particles [95]. Here also, the electrostatic particle-particle interactions were ignored and the Langevin equation is used for the modeling.

Finally, the details of the numerical simulation method followed in this work can be obtained from references [11, 96] and also from the e-book "Interrogations of Direct Numerical Simulation of Solid-Liquid Flow," by Joseph, D. D. The results of the numerical simulations of dielectric suspensions under the influence of nonuniform electric field using this method can be obtained from references [97, 98, and 99].

As can be noticed from the literature review, even though there had been a lot of experimental and theoretical studies of dielectrophoresis, there had been no attempts in the past to accurately simulate the phenomena using numerical simulation techniques. A numerical study is important, especially in the case of micro and nanoparticles, as it will help visualize the particle motion under the action of dielectrophoresis and isolate the effects of dielectrophoresis from that of the other forces that may be present. This study is one such attempt to accurately track the motion of particles under the action of dielectrophoretic force.

CHAPTER 2

GOVERNING EQUATIONS AND DIMENSIONLESS PARAMETERS

In this chapter, the electrostatic forces that arise in a nonuniform electric field due to the polarization of particles are described and the governing, dimensional and dimensionless, equations for both the particles and the fluid are stated.

Let us denote the domain containing a Newtonian fluid and N solid particles by Ω, the interior of the i^{th} particle by $P_i(t)$, and the domain boundary by Γ. The governing equations for the fluid-particle system are:

$$\rho_L\left(\frac{\partial \mathbf{u}}{\partial t}+\mathbf{u}\cdot\nabla\mathbf{u}\right)=\rho_L\mathbf{g}-\nabla p+\nabla\cdot(2\eta\mathbf{D}) \qquad \text{in } \Omega\backslash\overline{P(t)}$$

$$\nabla\cdot\mathbf{u}=0 \qquad \text{in } \Omega\backslash\overline{P(t)} \qquad (2.1)$$

$$\mathbf{u}=\mathbf{u}_L \qquad \text{on } \Gamma$$

$$\mathbf{u}=\mathbf{U}_i+\boldsymbol{\omega}_i\times\mathbf{r}_i \qquad \text{on } \partial P_i(t),\ i=1,\ldots,N \qquad (2.2)$$

Here $\mathbf{u}$ is the fluid velocity, p is the pressure, η is the dynamic viscosity of the fluid, ρ_L is the density of the fluid, $\mathbf{D}$ is the symmetric part of the velocity gradient tensor, $\mathbf{U}_i$ and ω_i are the linear and angular velocities of the i^{th} particle, and $\mathbf{g}$ is the acceleration due to gravity. The above equations are solved using the following initial conditions $\mathbf{u}|_{t=0}=\mathbf{u}_0$, where $\mathbf{u}_0$ is the known initial value of the velocity.

The linear velocity $\mathbf{U}_i$ and angular velocity ω_i of the i^{th} particle are governed by

$$m_i\frac{d\mathbf{U}_i}{dt}=\mathbf{F}_i+\mathbf{F}_{E,i}$$

$$I_i\frac{d\boldsymbol{\omega}_i}{dt}=\mathbf{T}_i \qquad (2.3)$$

$$\mathbf{U}_i \mid_{t=0} = \mathbf{U}_{i,0}$$

$$\boldsymbol{\omega}_i \mid_{t=0} = \boldsymbol{\omega}_{i,0} \tag{2.4}$$

where m_i and I_i are the mass and moment of inertia of the i^{th} particle, $\mathbf{F}_i$ and $\mathbf{T}_i$ are the hydrodynamic force and torque acting on the i^{th} particle and $\mathbf{F}_{E,i} = \mathbf{F}_{DEP,i} + \mathbf{F}_{D,i}$ is the net electrostatic force acting on the i^{th} particle. The dielectrophoretic force $\mathbf{F}_{DEP,i}$ acting on the i^{th} particle is given by (1.2) and $\mathbf{F}_{D,i}$ is the particle-particle interaction force on the i^{th} particle. In this study it is assumed that the particle density is equal to that of the fluid and thus the gravity term is dropped from the equations.

In a nonuniform electric field, the particle interaction force on the i^{th} particle due to the j^{th} particle is given by equation (1.4) and is:

$$\mathbf{F}_{D,ij} = \frac{1}{4\pi\varepsilon_0\varepsilon_c}\frac{3}{r^5}\left(\mathbf{r}_{ij}(\mathbf{p}_i \cdot \mathbf{p}_j) + (\mathbf{r}_{ij} \cdot \mathbf{p}_i)\mathbf{p}_j + (\mathbf{r}_{ij} \cdot \mathbf{p}_j)\mathbf{p}_i - \frac{5}{r^2}\mathbf{r}_{ij}(\mathbf{p}_i \cdot \mathbf{r}_{ij})(\mathbf{p}_j \cdot \mathbf{r}_{ij})\right)$$

where $\mathbf{p}_i$ and $\mathbf{p}_j$ are the dipole moments of the i^{th} and the j^{th} particles given by $\mathbf{p}_i = 4\pi\varepsilon_0\varepsilon_c\beta a^3\mathbf{E}_i$ and $\mathbf{p}_j = 4\pi\varepsilon_0\varepsilon_c\beta a^3\mathbf{E}_j$. The net electrostatic interaction force acting on the i^{th} particle is the sum of the interaction forces with all other particles of the suspension:

$$\mathbf{F}_{D,i} = \sum_{i=1, i\neq j}^{N} \mathbf{F}_{D,ij} \tag{2.5}$$

As mentioned above, the particles are considered to be spherical, and therefore we do not need to keep track of the particle orientation. The particle positions are obtained from

$$\frac{d\mathbf{X}_i}{dt} = \mathbf{U}_i \tag{2.6}$$

$$\mathbf{X}_i \mid_{t=0} = \mathbf{X}_{i,0} \tag{2.7}$$

where $\mathbf{X}_{i,0}$ is the position of the i^{th} particle at time $t = 0$. In this work, it is assumed that all particles have the same density ρ_p, and since they have the same radius, they also have the same mass, m.

Equations (2.1) and (2.3) are nondimensionalized by assuming that the characteristic length, velocity, time, stress, angular velocity and electric field scales are a, U, a/U, $\eta U/a$, U/a and E_0, respectively. The gradient of the electric field is assumed to scale as E_0/L, where L is the distance between the electrodes which is of the same order as the domain width. The nondimensional equations, after using the same symbols for the dimensionless variables, are:

$$Re\left(\frac{\partial \mathbf{u}}{\partial t}+\mathbf{u}\cdot\nabla\mathbf{u}\right)=-\nabla p+\nabla\cdot\boldsymbol{\sigma} \qquad \text{in } \Omega\backslash\overline{P(t)}$$

$$\nabla\cdot\mathbf{u}=0 \qquad \text{in } \Omega\backslash\overline{P(t)} \tag{2.8}$$

$$\frac{d\mathbf{U}}{dt}=\frac{6\pi\eta a^2}{m\mathbf{U}}\int\left(\frac{-p\mathbf{I}+\boldsymbol{\sigma}}{6\pi}\right)\cdot\mathbf{n}ds+\frac{4\pi a^4\varepsilon_0\varepsilon_c\beta|E_0|^2}{m\mathbf{U}^2L}(\mathbf{E}\cdot\nabla\mathbf{E})+\frac{3\pi\varepsilon_0\varepsilon_c a^3\beta^2|E_0|^2}{4m\mathbf{U}^2|r_{ij}|^4}(\mathbf{F}_D) \tag{2.9}$$

$$\frac{d\boldsymbol{\omega}}{dt}=\frac{5\eta a^2}{2m\mathbf{U}}\int(x-X)\times\left[(-p\mathbf{I}+\boldsymbol{\sigma})\cdot\mathbf{n}\right]ds \tag{2.10}$$

Notice that in the first term on the right hand side of (2.9) a factor of 6π is introduced to ensure that for an isolated particle the quantity inside the integral in the Stokes flow limit is equal to one.

The above equations contain the following dimensionless parameters:

$$Re=\frac{\rho_L \mathrm{U}a}{\eta},\ P_1=\frac{6\pi\eta a^2}{mU},\ P_2=\frac{3\pi\varepsilon_0\varepsilon_c\beta^2a^3|E_0|^2}{4mU^2},\ P_3=\frac{4\pi\varepsilon_0\varepsilon_c\beta a^4|E_0|^2}{mU^2L}$$

$$\text{and } h'=\frac{L}{a}. \tag{2.11}$$

Here *Re* is the Reynolds number, which determines the relative importance of the fluid inertia and viscous forces, P_1 is the ratio of the viscous and inertia forces, P_2 is the ratio of the electrostatic particle-particle interaction and inertia forces and P_3 is the ratio of the dielectrophoretic and inertia forces. Another important parameter, which does not appear directly in the above equations, is the solids fraction of the particles; the rheological properties of ER suspensions depend strongly on the solids fraction. We define another Reynolds number $Re_L = \frac{\rho_L L U}{\eta}$ based on the channel width L.

In order to investigate the relative importance of the electrostatic particle-particle and dielectrophoretic forces, we define the parameter

$$P_4 = \frac{P_2}{P_3} = \frac{3\beta L}{16a}. \tag{2.12}$$

In most applications of dielectrophoresis $L>>a$ because L is comparable to the domain size and the particle radius a is smaller than the domain size. However, there are applications in which L is only a few times larger than a. Expression (2.12) implies that if β= O(1) and $L>>a$, the particle-particle interaction forces will dominate, which is the case in most applications of dielectrophoresis. On the other hand, if $\beta << 1$ and $\frac{3\beta L}{16a} << 1$, the dielectrophoretic force dominates. In this limit, the particles move to the regions of local maxima or minima of the electric field without forming chains even when they are close to each other.

If the particle and fluid inertia can be set to zero, i.e., $Re = 0$, the number of dimensionless parameters reduce to three. The dimensionless parameters in this case are the Mason number *Ma*, P_5, and h'.

$$Ma = \frac{P_1}{P_2} = \frac{8\eta U}{\varepsilon_0 \varepsilon_c \beta^2 a |E_0|^2},$$

$$P_5 = \frac{P_3}{P_1} = \frac{2\varepsilon_0 \varepsilon_c \beta a^2 |E_0|^2}{3\eta UL}, \tag{2.13}$$

and $h' = \frac{L}{a}$. The Mason number determines the relative importance of the viscous force and the electrostatic particle-particle interaction force, and P_5 determines the relative importance of the electrostatic dielectrophoretic and viscous forces.

If there is no imposed bulk flow and the particle motion is caused by the dielectrophoretic force, an obvious choice of the characteristic velocity in this case is obtained by equating the dielectrophoretic force and viscous drag terms, which gives

$$U = \frac{2\varepsilon_0 \varepsilon_c \beta a^2 |E_0|^2}{3\eta L}. \tag{2.14}$$

If (2.14) is taken to be the characteristic velocity, the dimensionless parameters P_1 and P_3 are the same: $P_1 = P_3 = \frac{9\pi\eta^2 L}{m\varepsilon_0 \varepsilon_c \beta |E_0|^2}$, and $P_5 = 1$. The other parameters are thus:

$$\mathrm{Re} = \frac{2\rho_L \varepsilon_0 \varepsilon_c \beta a^3 |E_0|^2}{3\eta^2 L}, \quad P_2 = \frac{27\pi\eta^2 L^2}{16 m\varepsilon_0 \varepsilon_c a |E_0|^2}, \text{ and } P_4 = \frac{3\beta L}{16a} = \frac{1}{Ma}.$$

Assuming that the electric field $E_0 = \frac{V}{L}$, where V is the voltage applied to the electrodes, expression (2.14) for the characteristic velocity can be written as

$$U = \frac{2\varepsilon_0 \varepsilon_c \beta V^2}{3\eta L}\left(\frac{a}{L}\right)^2. \tag{2.15}$$

The above expression implies that if a/L, V and the material parameters are held constant, U increases with decreasing L. The ratio a/L is considered constant because the device size is decided by the size of the particles that need to be manipulated. Let us

consider the case where $\eta = 0.01$ Poise, $\beta = 1.0$, $\varepsilon_c = 80$, $\rho_L = 10^3$ kg/m^3, $a/L = 0.1$ and $V = 10$ volts. Substituting these values into (2.15) for a device with $L = 10$ μm, we obtain $U = 4.72 \times 10^4$ μm/s. On the other hand, for a device with $L = 1$ mm, $U = 472$ μm/s. Therefore, the velocity is *hundred* times larger in the smaller device. Since the particles must be moved over a larger distance in the larger device, we may conclude that the larger sized devices are less effective! This is the case because with increasing particle size the magnitude of the dielectrophoretic force becomes small compared to that of the viscous drag. In order to overcome this problem, a higher voltage is usually applied in a larger sized device. For example, for the device with $L = 20$ mm, the applied voltage is as large as $V = 10{,}000$ volts. The applied voltage, however, must be less than the critical voltage at which the electric discharge occurs.

CHAPTER 3

FINITE ELEMENT METHOD

3.1 Fluid and Particle Equations of Motion

Before proceeding to the governing equations for the liquid-particle system and the details of the numerical scheme and experiments, it is worthwhile to spend time here to discuss the basics of the direct numerical simulation scheme.

Denote the entire computational domain including the interior of the particles by Ω, and denote the domain boundary by Γ. Let $P(t)$ denote the interior of a particle (Figure 3.1).

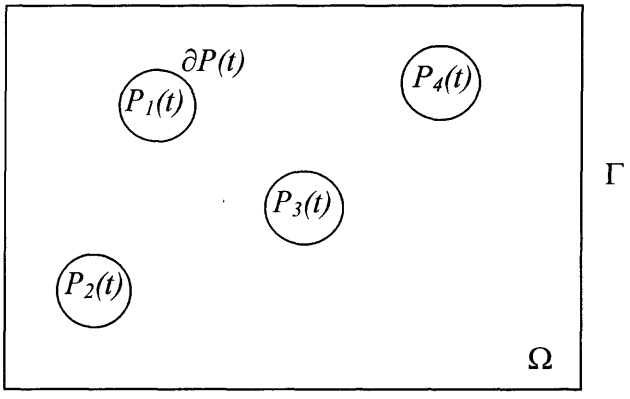

Figure 3.1 Figure showing the entire computational domain, including the particle.

The governing equations for the case of a Newtonian fluid are:

$$\nabla \cdot \mathbf{u} = 0 \qquad \text{in } \Omega \backslash \overline{P(t)} \tag{3.1}$$

$$\rho_L \left(\frac{\partial \mathbf{u}}{\partial t} + \mathbf{u} \cdot \nabla \mathbf{u} \right) = \rho_L \mathbf{g} - \nabla p + \nabla \cdot (2\eta \mathbf{D}) \qquad \text{in } \Omega \backslash P(t) \tag{3.2}$$

$$\mathbf{u} = \mathbf{u}_\Gamma(t) \qquad \text{on } \Gamma \tag{3.3}$$

$$\mathbf{u} = \mathbf{U} + \omega \times \mathbf{r} \qquad \text{on } \partial P(t) \tag{3.4}$$

$$\mathbf{u}|_{t=0} = \mathbf{u}_0 \qquad \text{in } \Omega\backslash\overline{P(0)} \tag{3.5}$$

The particle equations of motion, for the case of spherical particles are as follows:

$$m\frac{d\mathbf{U}}{dt} = m\mathbf{g} + \mathbf{F}[\mathbf{u}], \qquad I\frac{d\omega}{dt} = \mathbf{T}[\mathbf{u}] \tag{3.6}$$

$$\mathbf{U}|_{t=0} = \mathbf{U}_0, \qquad \omega|_{t=0} = \omega_0 \tag{3.7}$$

$$\frac{d\mathbf{X}}{dt} = \mathbf{U}, \qquad \frac{d\boldsymbol{\theta}}{dt} = \omega \tag{3.8}$$

$$\mathbf{X}|_{t=0} = \mathbf{X}_0, \qquad \Theta|_{t=0} = \Theta_0 \tag{3.9}$$

Here **F[u]** and **T[u]** are the hydrodynamic force and torque on the particle. The fluid and particle velocities on the surface of the particle are the same and is given by:

$$\mathbf{u} = \mathbf{U} + \boldsymbol{\omega} \times \mathbf{r} \tag{3.10}$$

The hydrodynamic force acting on the particle is given by the integral over the particle surface of the traction,

$$\sigma \cdot \mathbf{n} = -p\mathbf{n} + 2\eta\mathbf{D}[\mathbf{u}] \cdot \mathbf{n} \tag{3.11}$$

where

$\mathbf{D}[\mathbf{u}] = \frac{1}{2}(\nabla\mathbf{u} + \nabla\mathbf{u}^T)$ is the rate of strain tensor and **n** is the outward normal.

3.2 Direct Numerical Simulation Scheme

A direct numerical simulation scheme is one in which the governing equations of motion are solved exactly without using any models. For a fluid-particle system, such as an electrorheological fluid, the hydrodynamic forces are calculated from the numerical solution of the fluid equations which is in turn used to find the force acting on the

particles. In the present study of the electrorheological system, the fluid is considered to be Newtonian and the particles are treated as rigid bodies. Therefore, to perform the DNS, the governing equations for the fluid (Navier-Stokes equations in this case) and the governing equations for the particles (rigid-body motion) have to be simultaneously integrated. The governing equations are coupled through the no slip boundary condition on the particle surface and also through the hydrodynamic forces and torques that acts on the particle surface.

To perform the numerical simulation of the dielectrophoresis of electrorheological suspensions, the simulation scheme used is a DNS scheme utilizing the fictitious-domain method based on the distributed Lagrange multiplier (DLM), as developed by Glowinski et al. [11]. One of the core features of the method is that the fluid and particle equations of motion are combined into a combined weak equation of motion, which helps eliminate the hydrodynamic forces and torques acting on the particle surface. This is achieved by using a DLM, which helps ensure rigid-body motion inside and on each particle boundary. In this sense, the DLM represents an additional body force per unit volume required to maintain the rigid-body motion inside the particle boundary, and is analogous to pressure in incompressible fluid flow, whose gradient is the force required to maintain the constraint of incompressibility.

For efficient solution of the equations, the current method uses a finite element discretization in space using a regular tetrahedral mesh and time is discretized using an operator-splitting method using the Marchuk-Yanenko operator splitting technique.

3.2.1 Total Momentum Equation and Weak Formulation

In the present method, the hydrodynamic forces and torques acting on the particles are completely eliminated by combining the fluid and particle equations of motion into a single weak equation of motion for the combined fluid-particle system. This combined equation is called the combined equation of motion or the total momentum equation.

Define the combined velocity space

$$\begin{aligned}\mathbf{V}_{\mathbf{u}_\Gamma}(t) = \{(\mathbf{v},\mathbf{V},\xi) \mid \mathbf{v} \in \mathbf{H}^1(\Omega \setminus \overline{P(t)})^2, \mathbf{V} \in \mathbf{R}^2, \xi \in \mathbf{R}, \\ \mathbf{v} = \mathbf{V} + \xi \times \mathbf{r} \text{ on } \partial P(t), \text{ and } \mathbf{v} = \mathbf{u}_\Gamma(t) \text{ on } \Gamma\}\end{aligned} \tag{3.12}$$

The combined fluid-particle velocity (**u**, **U**, Ω) must lie in the combined velocity space, $\mathbf{V}_{\mathbf{u}_\Gamma}(t)$. The combined equation of motion is derived by taking a combined variation $(\mathbf{v},\mathbf{V},\xi)$ from the combined variation space

$$\begin{aligned}\mathbf{V}_0(t) = \{(\mathbf{v},\mathbf{V},\xi) \mid \mathbf{v} \in \mathbf{H}^1(\Omega \setminus \overline{P(t)})^2, \mathbf{V} \in \mathbf{R}^2, \xi \in \mathbf{R}, \\ \mathbf{v} = \mathbf{V} + \xi \times \mathbf{r} \text{ on } \partial P(t), \text{ and } \mathbf{v} = \mathbf{0} \text{ on } \Gamma\}\end{aligned} \tag{3.13}$$

The single weak equation can then be stated as follows:

Find **u**, p, **U**, ω satisfying

$$\begin{aligned}\int_{fluid} \rho_L \left(\frac{d\mathbf{u}}{dt} - \mathbf{g}\right) \cdot \mathbf{v} d\mathbf{x} + m\left(\frac{d\mathbf{U}}{dt} - \mathbf{g}\right) \cdot \mathbf{V} + I\frac{d\omega}{dt} \cdot \xi \\ = \int_{fluid} \sigma : \mathbf{D}(\mathbf{v}) d\mathbf{x} \qquad \text{for all } (\mathbf{v}, \mathbf{V}, \xi) \in \mathbf{V}_0\end{aligned} \tag{3.14}$$

$$\int_{fluid} q \nabla \cdot \mathbf{u} d\mathbf{x} = 0 \qquad \text{for all } q \tag{3.15}$$

Here **u** and **v** are both required to satisfy the no slip condition at the particle boundaries. That is:

$$\begin{aligned}\mathbf{u} &= \mathbf{U} + \omega \times \mathbf{r} \qquad \text{in } \partial P(t) \\ \mathbf{v} &= \mathbf{V} + \xi \times \mathbf{r} \qquad \text{in } \partial P(t)\end{aligned} \tag{3.16}$$

Once the combined weak form is obtained, the next step is to extend the problem from the domain excluding the particles, i.e. from $\Omega \setminus \overline{P(t)}$ to the whole of the domain, Ω. This is achieved by making use of the fictitious-domain method. The basic idea behind the fictitious domain method is to imagine that the fluid fills the space inside as well as outside the particle boundaries. The domain obtained as a result of this is simpler, which enables the use of a more simple regular mesh. Moreover, the extended domain being time-independent allows the use of the same mesh for the entire simulation.

In making use of the fictitious domain method, it is still taken care that the constraint of rigid-body motion is satisfied on the particle boundaries, $\partial P(t)$. In order to eliminate the hydrodynamic forces and torques the constraint of rigid-body motion has to be satisfied inside the particle boundaries. This is achieved by the use of a distributed Lagrange multiplier.

The extension of the problem to the entire domain is done in two steps. In the first step an equivalent combined equation is obtained for $P(t)$ and is added to the equation (3.14) to obtain a combined equation of motion for the whole of Ω. In the second step, the constraint of rigid-body motion is relaxed by removing it from the combined velocity spaces, and enforcing it as a side constraint using the Lagrange multiplier.

In order to achieve the first step, the constraint of rigid-body motion has to be satisfied for both $\mathbf{u}$ and $\mathbf{v}$ in the whole of $P(t)$, and not just on the boundary of the particle, $\partial P(t)$. That is we require:

$$\begin{aligned} \mathbf{u} &= \mathbf{U} + \omega \times \mathbf{r} \quad \text{in } P(t) \\ \mathbf{v} &= \mathbf{V} + \xi \times \mathbf{r} \quad \text{in } P(t) \end{aligned} \tag{3.17}$$

This will yield for *P(t)* the following:

$$\int_{P(t)} \rho_L \left(\frac{d\mathbf{u}}{dt} - \mathbf{g} \right) \cdot \mathbf{v} d\mathbf{x} - \frac{\rho_L}{\rho_d} m \left(\frac{d\mathbf{U}}{dt} - \mathbf{g} \right) \cdot \mathbf{V} - \frac{\rho_L}{\rho_d} I \frac{d\omega}{dt} \cdot \xi = -\int_{P(t)} \sigma : \mathbf{D}(\mathbf{v}) d\mathbf{x} \tag{3.18}$$

In order to obtain the combined weak equation of motion for the entire domain Ω, extend the combined velocity and combined variation spaces to *P(t)*, using the extended rigid-body motion constraint (3.17).

$$\mathbb{V}_{\mathbf{u}_\Gamma}(t) = \{ (\mathbf{v}, \mathbf{V}, \xi) \mid \mathbf{v} \in \mathbf{H}^1(\Omega)^2, \mathbf{V} \in \mathbf{R}^2, \xi \in \mathbf{R}, \; \mathbf{v} = \mathbf{V} + \xi \times \mathbf{r} \text{ in } P(t), \text{ and } \mathbf{v} = \mathbf{u}_\Gamma(t) \text{ on } \Gamma \} \tag{3.19}$$

$$\mathbb{V}_0(t) = \{ (\mathbf{v}, \mathbf{V}, \xi) \mid \mathbf{v} \in \mathbf{H}^1(\Omega)^2, \mathbf{V} \in \mathbf{R}^2, \xi \in \mathbf{R}, \; \mathbf{v} = \mathbf{V} + \xi \times \mathbf{r} \text{ in } P(t), \text{ and } \mathbf{v} = \mathbf{0} \text{ on } \Gamma \} \tag{3.20}$$

The extended fluid-particle velocity (**u**, **U**, ω) must lie in $\mathbb{V}_{\mathbf{u}_\Gamma}(t)$. The combined weak equation of motion for the entire domain Ω is obtained by adding equation (3.14) to equation (3.18), which takes the following form:

$$\int_\Omega \rho_L \left(\frac{d\mathbf{u}}{dt} - \mathbf{g} \right) \cdot \mathbf{v} d\mathbf{x} + \left(1 - \frac{\rho_L}{\rho_d} \right) \left(m \left(\frac{d\mathbf{U}}{dt} - \mathbf{g} \right) \cdot \mathbf{V} + I \frac{d\omega}{dt} \cdot \xi \right) = -\int_\Omega \sigma : \mathbf{D}(\mathbf{v}) d\mathbf{x} \quad \text{for all } (\mathbf{v}, \mathbf{V}, \xi) \in \mathbb{V}_0. \tag{3.21}$$

The constraint of rigid body motion that the solution function **u** and the variation **v** are required to satisfy throughout *P(t)* in equation (3.21) is relaxed by removing it from the combined velocity spaces and enforcing it as a side constraint in the weak sense and adding an appropriate distributed Lagrange multiplier term to the right hand side of equation (3.21). This results in the following weak formulation of the problem in the extended domain:

Find $\mathbf{u} \in \mathbf{W}_{u_\Gamma}, p \in L_0^2(\Omega), \lambda \in \Lambda(t), \mathbf{U} \in \mathbf{R}^2, \omega \in \mathbf{R}$ satisfying

$$\int_\Omega \rho_L \left(\frac{\partial \mathbf{u}}{\partial t} + (\mathbf{u} \cdot \nabla)\mathbf{u} - \mathbf{g} \right) \cdot \mathbf{v} d\mathbf{x} - \int_\Omega p \nabla \cdot \mathbf{v} d\mathbf{x} + \int_\Omega 2\eta \mathbf{D}[\mathbf{u}] : \mathbf{D}[\mathbf{v}] d\mathbf{x}$$
$$+ \left(1 - \frac{\rho_L}{\rho_d} \right) \left(m \left(\frac{d\mathbf{U}}{dt} - \mathbf{g} \right) \cdot \mathbf{V} + I \frac{d\omega}{dt} \cdot \xi \right) \tag{3.22}$$
$$= \left\langle \lambda, \mathbf{v} - (\mathbf{V} + \xi \times \mathbf{r}) \right\rangle_{P(t)} \quad \text{for all } \mathbf{v} \in \mathbf{W}_0, \mathbf{V} \in \mathbf{R}^2, \xi \in \mathbf{R}.$$

where $\frac{d\mathbf{u}}{dt} = \frac{\partial \mathbf{u}}{\partial t} + (\mathbf{u} \cdot \nabla)\mathbf{u}$ and $\sigma = -p\mathbf{I} + 2\eta \mathbf{D}[\mathbf{u}]$

$$\int_\Omega q \nabla \cdot \mathbf{u} d\mathbf{x} = 0 \quad \text{for all } q \in L^2(\Omega) \tag{3.23}$$

$$\left\langle \mu, \mathbf{u} - (\mathbf{U} + \omega \times \mathbf{r}) \right\rangle_{P(t)} = 0 \quad \text{for all } \mu \in \Lambda(t) \tag{3.24}$$

$$\mathbf{u}|_{t=0} = \mathbf{u}_0 \quad \text{in } \Omega \tag{3.25}$$

In addition to the above, the kinematic equation (3.8) and the initial conditions (3.7) and (3.9) are to be satisfied.

Here, $\mathbf{u}_0$ satisfies the compatibility conditions,

$$\nabla \cdot \mathbf{u}_0 = 0 \qquad \text{in } \Omega \setminus \overline{P(0)}$$
$$\mathbf{u}_0 = U_0 + \omega_0 \times r_0 \qquad \text{in } P(0)$$

Here,

$$\mathbf{r}_0 = \mathbf{x} - \mathbf{X}(0),$$
$$\mathbf{W}_{u_\Gamma} = \left\{ \mathbf{v} \in H^1(\Omega)^2 \mid \mathbf{v} = \mathbf{u}_\Gamma(t) \text{ on } \Gamma \right\},$$
$$\mathbf{W}_0 = H_0^1(\Omega)^2,$$
$$L_0^2(\Omega) = \left\{ q \in L^2(\Omega) \mid \int_\Omega q d\mathbf{x} = 0 \right\},$$

and $\Lambda(t)$ is $H^1(P(t))^2$, with $\langle .,. \rangle_{P(t)}$ denoting an appropriate inner product.

3.2.2 Collision Strategy

In order to prevent the particles from penetrating each other and the boundary of the domain, an additional short-range repulsive force is introduced. When this additional force is included the particle equation of motion for the i^{th} particle will take the form:

$$m_i \frac{\mathrm{d}\mathbf{U}_i}{\mathrm{dt}} = m_i \mathbf{g} + \mathbf{F}_i + \mathbf{F}_i'$$

where

$\mathbf{F}_i' = \sum_{\substack{j=1 \\ j \neq i}}^{N} \mathbf{F}_{i,j}^P + \sum_{j=1}^{4} \mathbf{F}_{i,j}^W$ is the short-range repulsive force acting on the i^{th} particle which is due to the presence of the other particles and due to the four boundary walls.

The particle-particle repulsive force is given by:

$$\mathbf{F}_{i,j}^P = \begin{cases} 0, & d_{i,j} > R_i + R_j + \rho, \\ \dfrac{1}{\varepsilon_P}(\mathbf{X}_i - \mathbf{X}_j)(R_i + R_j + \rho - d_{i,j})^2 & d_{i,j} \leq R_i + R_j + \rho \end{cases}$$

where $d_{i,j} = |\mathbf{X}_i - \mathbf{X}_j|$ is the distance between the i^{th} and the j^{th} particle, R_i is the radius of the i^{th} particle, ρ is the force range, and ε_p is a small positive stiffness parameter.

The particle-wall repulsive force is given by:

$$\mathbf{F}_{i,j}^W = \begin{cases} 0, & d_{i,j}' > 2R_i + \rho, \\ \dfrac{1}{\varepsilon_W}(\mathbf{X}_i - \mathbf{X}_{i,j}')(2R_i + \rho - d_{i,j}')^2 & d_{i,j}' \leq 2R_i + \rho \end{cases}$$

where $d_{i,j}' = |\mathbf{X}_i - \mathbf{X}_{i,j}'|$ is the distance between the i^{th} particle and an imaginary particle $P_{i,j}'$ located on the other side of the boundary (refer Figure 3.2), Γ_j and ε_W is a small stiffness parameter.

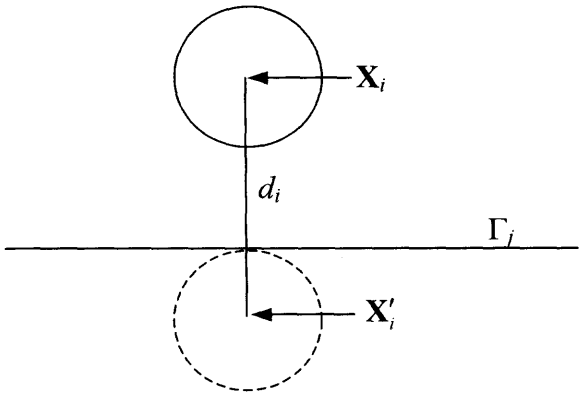

Figure 3.2 Figure showing particle-wall repulsion introduced through the imaginary particle.

The above DLM scheme uses operator-splitting for time discretization. More details on the time discretization and the finite element method used are given in the following section. The above method as developed by Glowinski et al. has been applied to a variety of problems involving particulate flows. How ever, this is the first time the direct simulation method is applied to study the particle structure formation in electrorheological suspensions under the action of dielectrophoretic force.

3.3 Computational Scheme

The computational scheme used in this work is a generalization of the DLM finite-element scheme described in [11, 96]. In this scheme, the fluid flow equations are solved on the combined fluid-solid domain, and the motion inside the particle boundaries is forced to be rigid-body motion using a distributed Lagrange multiplier. The fluid and particle equations of motion are combined into a single combined weak equation of motion, eliminating the hydrodynamic forces and torques, which helps ensure the

stability of the time integration. For the sake of simplicity, in this section, we assume that there is only one particle. The extension to the multi-particle case is straightforward.

The solution and variation are required to satisfy the strong form of the constraint of rigid body motion throughout *P(t)*. In the distributed Lagrange multiplier method, this constraint is removed from the velocity space and enforced weakly as a side constraint using a distributed Lagrange multiplier term. It was shown in [11, 96] that the following weak formulation of the problem holds in the extended domain:

For a.e. $t > 0$, find $\mathbf{u} \in \overline{W}_{u\Gamma}$, $p \in L_0^2(\Omega)$, $\lambda \in \Lambda(t)$, $\mathbf{U} \in \mathbf{R}^3$ and $\omega \in \mathbf{R}^3$, satisfying

$$\int_\Omega \rho_L \left(\frac{d\mathbf{u}}{dt} - \mathbf{g} \right) \cdot \mathbf{v} d\mathbf{x} - \int_\Omega p \nabla . \mathbf{v} \, d\mathbf{x} + \int_\Omega 2\eta \mathbf{D}[\mathbf{u}] : \mathbf{D}[\mathbf{v}] d\mathbf{x}$$
$$+ \left(1 - \frac{\rho_L}{\rho_d} \right) \left(M \left(\frac{d\mathbf{U}}{dt} - \mathbf{g} \right) \cdot \mathbf{V} + I \frac{d\omega}{dt} \xi \right) - \mathbf{F}' . \mathbf{V} = \left\langle \boldsymbol{\lambda}, \mathbf{v} - (\mathbf{V} + \xi \times \mathbf{r}) \right\rangle_{P(t)}$$

$$\text{for all } \mathbf{v} \in \overline{W}_0, \mathbf{V} \in \mathbf{R}^3, \text{ and } \xi \in \mathbf{R}^3, \tag{3.26}$$

$$\int_\Omega q \nabla . u \, dx = 0 \qquad \text{for all } q \in L^2(\Omega), \tag{3.27}$$

$$\left\langle \boldsymbol{\mu}, \mathbf{u} - (\mathbf{U} + \omega \times \mathbf{r}) \right\rangle_{P(t)} = 0 \qquad \text{for all } \mu \in \Lambda(t), \tag{3.28}$$

$$\mathbf{u}|_{t=0} = \mathbf{u}_0 \qquad \text{in } \Omega, \tag{3.29}$$

as well as the kinematic equations and the initial conditions for the particle linear and angular velocities. Here $\mathbf{F}'$ is the additional body force applied to the particles to limit the extent of overlap (see equation (19) in Glowinski, et al. (1999)) and λ is the distributed Lagrange multiplier,

$$\overline{W}_{u\Gamma} = \{ \mathbf{v} \in H^1(\Omega)^3 \mid \mathbf{v} = \mathbf{u}_\Gamma(t) \quad \text{on} \quad \Gamma \},$$

$$\overline{W}_0 = H_0^1(\Omega)^3,$$

$$L_0^2(\Omega) = \{q \in L^2(\Omega) \mid \int_\Omega q \, d\mathbf{x} = 0 \}, \tag{3.30}$$

and $\Lambda(t)$ is $L^2(P(t))^3$, with $\langle .,. \rangle_{P(t)}$ denoting the L^2 inner product over the particle, where Γ^- is the upstream part of Γ. In our simulations, since the velocity and μ are in L^2, we will use the following inner product

$$\langle \boldsymbol{\mu}, \mathbf{v} \rangle_{P(t)} = \int_{P(t)} (\boldsymbol{\mu}.\mathbf{v}) \, d\mathbf{x}. \tag{3.31}$$

In order to solve the above problem numerically, we will discretize the domain using a regular tetrahedral mesh T_h for the velocity, where h is the mesh size, and a regular tetrahedral mesh T_{2h} for the pressure. The following finite dimensional spaces are defined for approximating $\overline{W}_{u\Gamma}$, $\overline{W}_0$, $L^2(\Omega)$ and $L_0^2(\Omega)$:

$$W_{u\Gamma,h} = \{\mathbf{v}_h \in C^0(\overline{\Omega})^3 \mid \mathbf{v}_h|_T \in P_1 \times P_1 \times P_1 \text{ for all } T \in T_h, \mathbf{v}_h = \mathbf{u}_{\Gamma,h} \text{ on } \Gamma\},$$

$$W_{0,h} = \{\mathbf{v}_h \in C^0(\overline{\Omega})^3 \mid \mathbf{v}_h|_T \in P_1 \times P_1 \times P_1 \text{ for all } T \in T_h, \mathbf{v}_h = 0 \text{ on } \Gamma\} \quad , \tag{3.32}$$

$$L_h^2 = \{q_h \in C^0(\overline{\Omega}) \mid q_h|_T \in P_1 \text{ for all } T \in T_{2h}\}, \text{ and}$$

$$L_{0,h}^2 = \{q_h \in L_h^2 \mid \int_\Omega q_h \, d\mathbf{x} = 0\}. \tag{3.33}$$

The particle inner product terms in (3.26) and (3.28) are obtained using the discrete L^2 inner product defined in Glowinski, et al. (1999). Specifically, we choose M points, $\mathbf{x}_1, \ldots, \mathbf{x}_M$ that uniformly cover $\overline{P}(t)$, and define

$$\Lambda_h(t) = \left\{ \boldsymbol{\mu}_h \;\middle|\; \boldsymbol{\mu} = \sum_{i=1}^{M} \boldsymbol{\mu}_{h,i} \, \delta(\mathbf{x} - \mathbf{x}_i), \quad \boldsymbol{\mu}_{h,1}, \ldots, \boldsymbol{\mu}_{h,M} \in \mathbf{R}^3 \right\}.$$

Using these finite dimensional spaces, it is straightforward to discretize equations (3.26-3.29).

3.4 Time Discretization Using the Marchuk-Yanenko Operator Splitting Scheme

The initial value problem (3.26-3.29) is solved by using the Marchuk-Yanenko operator-splitting scheme, which allows us to decouple its three primary difficulties:

1. The incompressibility condition, and the related unknown pressure p_h,
2. The nonlinear advection term,
3. The constraint of rigid-body motion in $P_h(t)$, and the related distributed Lagrange multiplier λ_h.

The Marchuk-Yanenko operator-splitting scheme can be applied to an initial value problem of the form

$$\frac{d\phi}{dt} + A_1(\phi) + A_2(\phi) + A_3(\phi) = f$$

where the operators A_1, A_2 and A_3 can be multi-valued. Let Δt be the time step. We use the following version of the Marchuk-Yanenko operator splitting scheme to simulate the motion of particles in an ER fluid:

Set $\mathbf{u}^0 = \mathbf{u}_{0,h}$, $\mathbf{U}^0 = \mathbf{U}_0$, $\mathbf{X}^0 = \mathbf{X}_0$ and $\omega^0 = \omega_0$, and calculate $\mathbf{E}$ by solving $\nabla^2\varphi = 0$, subjected to the electric potential boundary conditions, and then calculate $\mathbf{E} = \nabla\varphi$.

For n = 0, 1, 2,... assuming $\mathbf{u}^n$, $\mathbf{U}^n$, $\mathbf{X}^n$, and ω^n are known, we find the values for the $(n+1)^{th}$ time step using the following steps:

STEP 1:

Find $\mathbf{u}^{n+1/4} \in W^{n+1}_{u\Gamma,h}$ and $p^{n+1/4} \in L^2_{0,h}$, by solving

$$\int_\Omega \rho_L \frac{\mathbf{u}^{n+1/4} - \mathbf{u}^n}{\Delta t}.\mathbf{v}\, d\mathbf{x} - \int_\Omega p^{n+1/4} \nabla.\mathbf{v}\, d\mathbf{x} + \alpha \int_\Omega 2\eta_s \mathbf{D}[\mathbf{u}^{n+1/4}] : \mathbf{D}[\mathbf{v}] d\mathbf{x} = \mathbf{0}$$

for all $\mathbf{v} \in W_{0,h}$,

$$\int_\Omega q \nabla.\mathbf{u}^{n+1/4} d\mathbf{x} = 0 \qquad \text{for all } q \in L_h^2, \tag{3.34}$$

STEP 2:

Find $\mathbf{u}^{n+2/4} \in W_{u\Gamma,h}^{n+1}$, by solving

$$\int_\Omega \rho_L \frac{\mathbf{u}^{n+2/4} - \mathbf{u}^{n+1/4}}{\Delta t}.\mathbf{v} d\mathbf{x} + \int_\Omega \rho_L (\mathbf{u}^{n+2/4}.\nabla \mathbf{u}^{n+2/4}).\mathbf{v}\, d\mathbf{x} + \beta \int_\Omega 2\eta_s \mathbf{D}[\mathbf{u}^{n+2/4}] : \mathbf{D}[\mathbf{v}] d\mathbf{x} = 0$$

$$\text{for all } \mathbf{v} \in W_{0,h} \tag{3.35}$$

STEP 3:

Compute $\mathbf{U}^{n+2/4}$ and $\mathbf{X}^{n+2/4}$ using the prediction procedure

Set $\mathbf{U}^{n,0} = \mathbf{U}^n$, $\mathbf{X}^{n,0} = \mathbf{X}^n$.

Do k = 1,K

Calculate $\mathbf{F}_E\left(X^{n,k-1}\right)$

$$\mathbf{U}^{*n,k} = \mathbf{U}^{n,k-1} + \left(\mathbf{g} + \left(1 - \frac{\rho_L}{\rho_d}\right)^{-1} M^{-1}\left[\mathbf{F}'(X^{n,k-1}) + \mathbf{F}_E\left(X^{n,k-1}\right)\right]\right)\frac{\Delta t}{K}$$

$$\mathbf{X}^{*n,k} = \mathbf{X}^{n,k-1} + \left(\frac{\mathbf{U}^{n,k-1} + \mathbf{U}^{*n,k}}{2}\right)\frac{\Delta t}{K}$$

$\mathbf{U}^{n,k} = \mathbf{U}^{n,k-}$

$$^1 + \left(\mathbf{g} + \left(1 - \frac{\rho_L}{\rho_d}\right)^{-1} M^{-1} \frac{\mathbf{F}'(X^{n,k-1}) + \mathbf{F}'(X^{*n,k-1}) + \mathbf{F}_E(X^{n,k-1}) + \mathbf{F}_E(X^{*n,k-1})}{2}\right)\frac{\Delta t}{K}$$

$$\mathbf{X}^{n,k} = \mathbf{X}^{n,k-1} + \left(\frac{\mathbf{U}^{n,k-1} + \mathbf{U}^{n,k}}{2}\right)\frac{\Delta t}{K}$$

end do

Then set $\mathbf{U}^{n+2/4} = \mathbf{U}^{n,K}$, $\mathbf{X}^{n+2/4} = \mathbf{X}^{n,K}$. (3.36)

The next step consists of finding $\mathbf{u}^{n+1} \in W_{u\Gamma,h}^{n+1}$, $\lambda^{n+1} \in \Lambda_h((n+2/4)\Delta t)$, $\mathbf{U}^{n+1} \in \mathbf{R}^3$, and $\omega^{n+1} \in \mathbf{R}^3$, satisfying

$$\int_\Omega \rho_L \frac{\mathbf{u}^{n+1}-\mathbf{u}^{n+2/4}}{\Delta t}.\mathbf{v}\,dx + \left(1-\frac{\rho_L}{\rho_d}\right)\left(M\frac{\mathbf{U}^{n+1}-\mathbf{U}^{n+2/4}}{\Delta t}.\mathbf{V} + I\frac{\boldsymbol{\omega}^{n+1}-\boldsymbol{\omega}^{n+2/4}}{\Delta t}\xi\right) +$$
$$= \left\langle \lambda^{n+1}, \mathbf{v}-(\mathbf{V}+\xi\times\mathbf{r}^{n+2/4})\right\rangle_{P((n+2/4)\Delta t)}$$

for all $\mathbf{v} \in W_{0,h}$, $\mathbf{V} \in \mathbf{R}^2$, and $\xi \in \mathbf{R}$ (3.37)

where the center of the particle $P((n+2/4)\Delta t)$ is at the location $X^{n+2/4}$.

Then set $\mathbf{X}^{n+1,0} = \mathbf{X}^n$.

For k = 1, K, follow the do-loop

$$\mathbf{X}^{*n+1,k} = \mathbf{X}^{n+1,k-1} + \left(\frac{\mathbf{U}^n + \mathbf{U}^{n+1}}{2}\right)\frac{\Delta t}{K}$$

$$\mathbf{X}^{n,k} = \mathbf{X}^{*n,k-1} + \left(1-\frac{\rho_L}{\rho_d}\right)^{-1} M^{-1}\left(\frac{F'(X^{n+1,k-1}) + F'(X^{*n+1,k})}{2}\right)\frac{(\Delta t)^2}{2K}$$

end do

Then set $\mathbf{X}^{n+1} = \mathbf{X}^{n+1,K}$. (3.38)

Then set $p^{n+1} = p^{n+1/4}$, and go back to the first step.

Remarks:

1. The problems arising in the first and second steps are solved using the conjugate gradient algorithm described in [11].

2. α_1 and α_2 are assumed to be the same and its value is 0.5.

3. The third step is used to obtain the distributed Lagrange multiplier that enforces rigid body motion inside the particles. This problem is solved by using the conjugate

gradient method described in [11, 96]. In this step, we account for the electrostatic forces that arise due to the dielectrophoretic effect and the particle-particle interactions.

CHAPTER 4

RESULTS OF NUMERICAL SIMULATIONS

4.1 Typical Domain for the Simulations

Figure 4.1 shows a typical domain, the initial arrangement of the particles and the coordinate system used in the simulations. The dimensions of the box shaped domain are 1.6 mm x 0.8 mm x 2.4 mm in the *x*-, *y*- and *z*-directions. The fluid velocity is assumed to be zero on the sidewalls of the domain and periodic along the *z*-direction. The electric field is also assumed to be periodic in the *z*-direction. The electrostatic and hydrodynamic forces include contributions from the periodic images in the *z*-direction. The imposed fluid velocity and the pressure gradient in the *z*-direction are assumed to be zero.

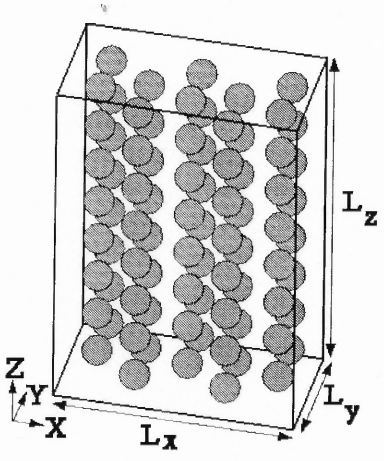

Figure 4.1 An oblique view of a typical domain used for simulations.

The nonuniform electric field is generated by placing one or two pairs of electrodes on the domain side walls parallel to the *yz*-coordinate plane. In order to generate a nonuniform electric field the electrodes are made shorter than the side walls so that they do not cover the side walls entirely. The electrodes are placed so that they do not affect the fluid boundary conditions, by embedding them into the side walls. The

generated nonuniform electric fields vary at scales comparable to the domain size since the electrodes are separated by distances which are comparable to the length of the electrodes. The width of the electrodes in the y-direction is equal to the domain width and hence the electric field does not vary in the y-direction. The fluid and particle velocities, and particle-particle interaction forces, however, vary in the y-direction.

For the simulations discussed in this chapter, we assume that the dynamic fluid viscosity is $\eta = 1.0$ Poise, the particle diameter and density are 0.2 mm and 1.01 g/cm^3, respectively and the fluid density is $\rho_L = 1.0$ g/cm^3. Gravity is ignored, because the density of particles is quite close to that of the fluid and the particle diameter is small. The initial fluid and particle velocities are set to zero. The domain is discretized using a regular pseudo P2-P1 tetrahedral mesh, as described in the previous chapter.

4.2 Convergence Study

To show that the results converge with mesh and time step refinements, let us consider the transient motion of two particles subjected to the nonuniform electric field shown in Figures 4.3 and 4.4. The applied pressure gradient is assumed to be zero. Notice that even though the pressure gradient is zero, the fluid velocity and the electric field are assumed to be periodic in the z-direction, and the electrostatic particle-particle interaction force is computed by accounting for the periodicity.

The domain used in this study is 1.6 mm x 0.4 mm x 1.6 mm. At $t = 0$, two particles with $\beta = 0.297$ are placed at the initial positions (0.4 mm, 0.2 mm, 1.4 mm) and (1.2 mm, 0.2 mm, 1.4 mm) respectively, as shown in Figure 4.2. The electric field is generated by placing two 0.4 mm long electrodes in the domain walls parallel to the yz-

coordinate plane, as shown in Figure 4.2. The left side electrode is grounded and the electric potential for the right side electrode is assumed to be 1.0. Isovalues of the electric field magnitude and the magnitude of $\mathbf{E}.\nabla\mathbf{E}$ are shown in Figures 4.3 and 4.4. The values of dimensionless parameters are: $Re = 40.03$, $P_1 = 0.111$, $P_2 = 0.0992$ and $P_3 = 0.111$. The Mason number is 1.12, P_4 is 0.892 and P_5 is 1.0. Since the parameters P_2 and P_3 are approximately equal, the electrostatic particle-particle interaction and dielectrophoretic forces acting on the particles are of the same order of magnitude.

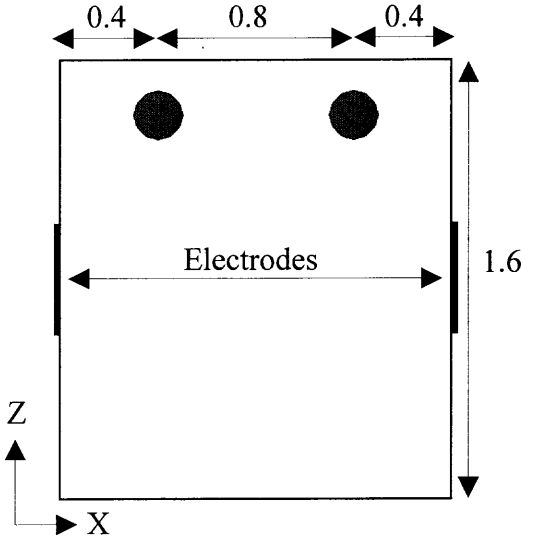

Figure 4.2 The domain midsection normal to the y-axis is shown. Illustrated are the electrode locations and the initial positions of the two particles. The potential is prescribed on the electrode surfaces and the normal derivative of the potential is assumed to be zero on the rest of the boundary. The velocity is assumed to be periodic in the *z*-direction and zero on the other domain surfaces.

The initial positions of the two particles in this case were selected such that the magnitudes of the electrostatic particle-particle interaction force and the dielectrophoretic force are comparable. Thus, once the simulation is started, the particles move toward

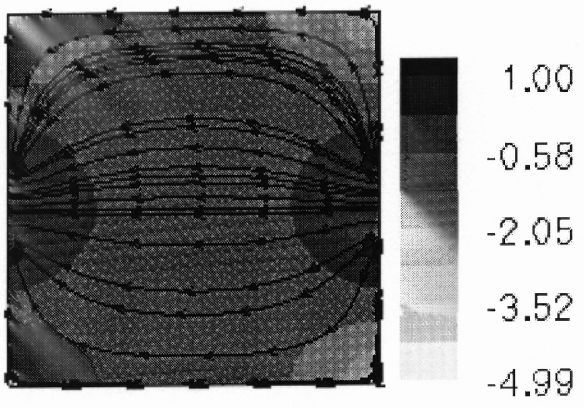

Figure 4.3 Isovalues of log (|**E**|) and the direction of **E** at the domain midsection are shown. The electric field is maximum on the electrode tips and does not vary with y.

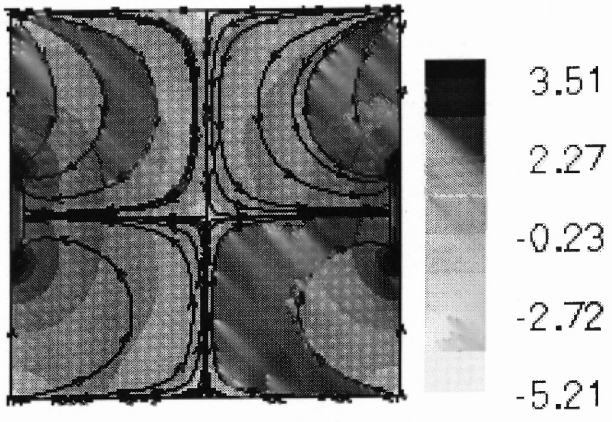

Figure 4.4 Isovalues of log (|**E**.∇**E**|) and the lines of dielectrophoretic force are shown. **E**.∇**E** does not vary with y.

each other, and at the same time, each one moves towards the electrode closer to it due to the dielectrophoretic force. The particle on the left side moves towards the left electrode and the right side particle moves towards the right electrode. As the distance between the particles and the electrodes decreases, the dielectrophoretic force becomes greater than the electrostatic particle-particle interaction force. This causes the particles to move away

from each other and toward the edges of the electrodes where they are collected approximately at $t = 0.5$ s.

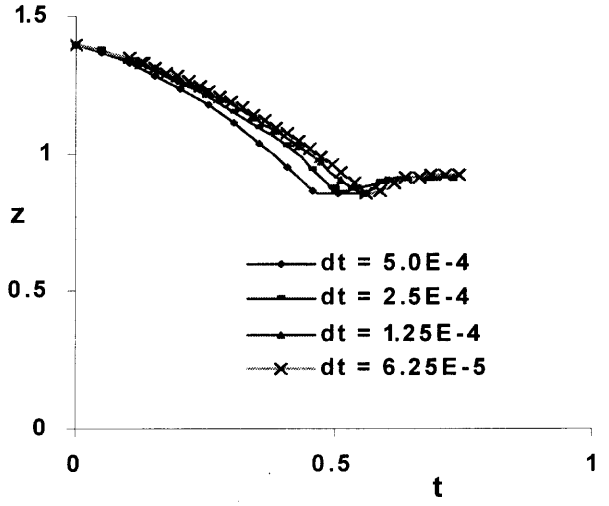

Figure 4.5 The z-coordinate of the second particle is plotted as a function of time for four different time steps.

To show that the results converge when the time step size is reduced, the z-coordinate of the second particle is plotted as a function of time for four different values of the time step: $5\text{x}10^{-4}$ s, $2.5\text{x}10^{-4}$ s, $1.25\text{x}10^{-4}$ s and $0.625\text{x}10^{-4}$ s (see Figure 4.5). The number of velocity nodes for all four cases is 71,825. Since the trajectories for the smallest two time steps are approximately the same, we conclude that the results converge as the time step is reduced.

In order to show that the results also converge with mesh refinement, simulations were performed for three different mesh sizes. The number of velocity nodes for the three cases are 71,825, 137,781 and 549,153. The time step used for these calculations was $5\text{x}10^{-4}$ s. For the three mesh refinements, the z-coordinate of the second particle is plotted as a function of time in Figure 4.6. As the trajectories of the particles for the two finer

meshes are approximately the same, it may be concluded that the results are also independent of mesh resolution.

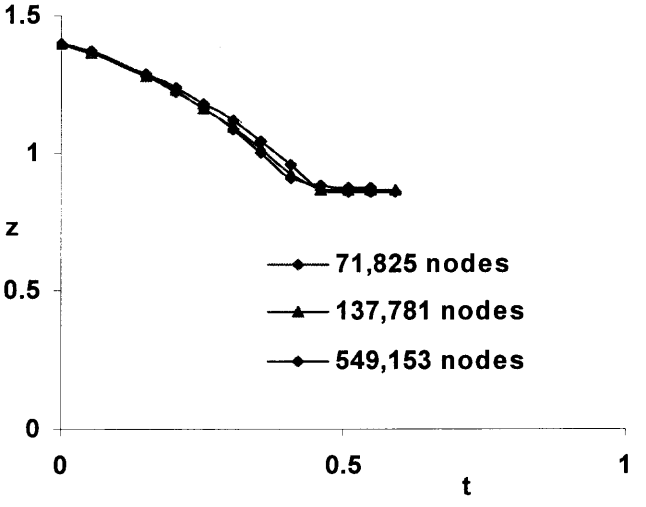

Figure 4.6 The z-coordinate of the second particle plotted as a function of time for three different mesh sizes.

4.3 Influence of parameter P_4

As discussed in chapter 2, parameter $P_4 = \frac{P_2}{P_3} = \frac{3\beta L}{16a}$ determines the relative importance of the electrostatic particle-particle and dielectrophoretic forces. As the dielectrophoretic force dominates when $P_4 < O(1)$, the particles are easily separated from neighbors and move individually to the maxima or minima of the electric field. On the other hand, when $P_4 > O(1)$, the particle-particle interactions dominate which results in the formation of the particle chains which then move relatively slowly towards the minima or maxima of the electric field. In fact, when $P_4 > O(1)$ and the particle concentration is sufficiently large, the particles form chains extending from one electrode to the opposite one, preventing the removal of particles.

The numerical simulations were performed in a domain as shown in Figure 4.1, the electric field and the log of ($|\mathbf{E}.\nabla\mathbf{E}|$) are shown in Figures 4.7 and 4.8 respectively. In the numerical simulations discussed, the value of P_4 is varied using two different approaches. In both approaches, only those dimensionless parameters that depend on the electrostatic forces are varied and the remaining parameters are held fixed. In the first approach, P_4 is varied by changing β and in the second by changing P_2 and P_3. Even though P_2 and P_3 cannot be varied independently for a real ER fluid, the approach is useful for analyzing the mathematical nature of equations.

First, two cases where the value of $\beta = 0.5$ and 0.01 are discusssed. The particle-particle interaction force is expected to dominate in the first case and the dielectrophoretic force is expected to dominate in the second. For $\beta = 0.5$, the dielectric constants of the particles and fluid are 10 and 2.5, respectively. The left electrodes are grounded whereas the right ones are at 2000 Volts. Eighty particles are arranged in the box shaped domain in a periodic manner as shown in Figure 4.1.

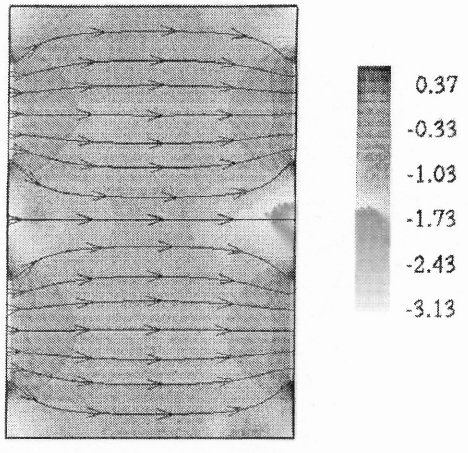

Figure 4.7 Isovalues of log ($|\mathbf{E}|$) and the direction of **E** on the domain midsection are shown. Notice that the electric field is maximum at the electrode tips. The electric field does not vary with y.

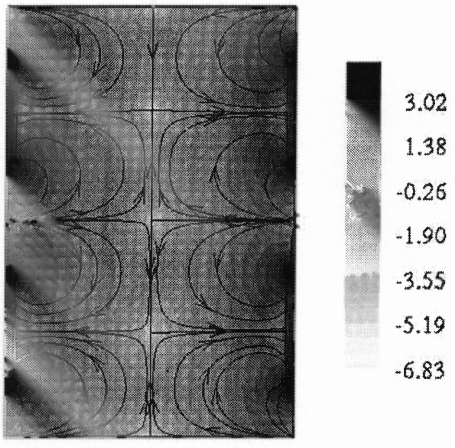

Figure 4.8 Isovalues of log (|**E**.∇**E**|) and the lines of dielectrophoretic force are shown. **E**.∇**E** does not vary with y.

The solids fraction is 0.118. The values of dimensionless parameters in this case are Re = 7.2, P_1 = 0.618, P_2 = 0.927, P_3 = 0.618, Ma = 0.67, and P_4 = 1.5. Simulations show that at $t \sim 0.9$ s the particle chains are formed (see Figure 4.9) and then these chains move toward the electrode edges at a smaller speed than of individual particles. The positions of the particles at t = 3.0 s is shown in Figure 4.10.

For β = 0.01, the dielectric constants of the particles and fluid are 2.576 and 2.5. In order to ensure that the magnitude of the dielectrophoretic force, which depends on β, is the same as for the case described above, i.e., P_3 remains 0.618, the electric field strength is increased. The values of dimensionless parameters are Re = 7.2, P_1 = 0.618, P_2 = 0.0185, P_3 = 0.618, Ma = 33.3, and P_4 = 0.03. Figure 4.11 shows the positions of the particles at t = 0.9 s from which it can be seen that the particles in the middle have already started moving to the electrodes, without forming chains. The position of the particles at time, t = 3.0 s is shown in Figure 4.12. Notice that most particles, except those in the middle, are attached to the edges of the electrodes by this time. The vertical

chains of particles seen at the middle of the domain are formed due to the presence of the saddle points at (x = 0.8, z = 0.6), (x = 0.8, z = 1.2) and (x = 0.8, z = 1.8). As can be observed from Figures 4.7 and 4.8, at these points the dielectrophoretic force is zero, but the magnitude of the electric field is not locally minimum.

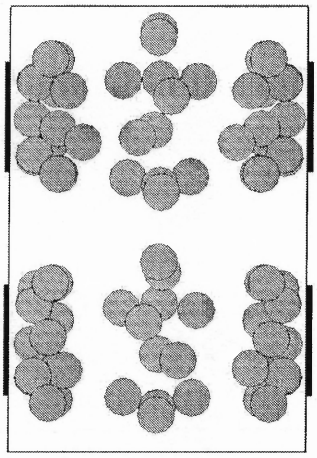

Figure 4.9 The front view of the particle distribution at t = 0.9 s for P_4 = 1.5. The particles come together as chains in the middle of the domain, and then move toward the electrode edges.

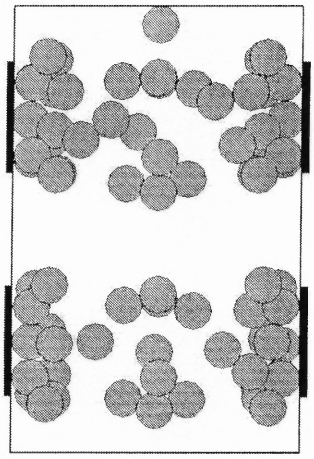

Figure 4.10 The front view of the particle distribution at time t = 3.0 s for P_4 = 1.5. Notice that the chains fill the gap between the electrodes.

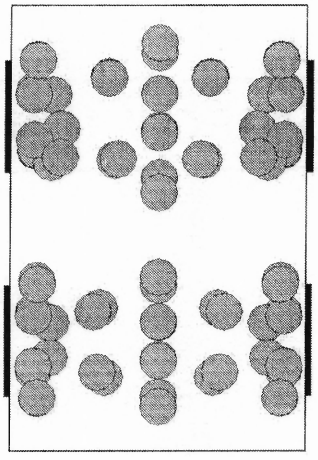

Figure 4.11 The front view of the particle distribution at $t = 0.9$ s for $P_4 = 0.03$. In this case the particles in the middle are seen to move to the electrodes edges without forming chains. The particles in the middle are not collected at this time.

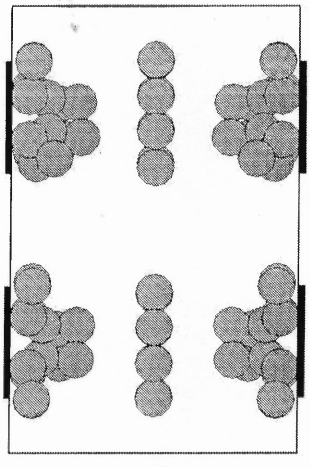

Figure 4.12 The front view of the particle distribution at $t = 3.0$ s for $P_4 = 0.03$

Next, two cases where the values of parameters P_2 and P_3 are changed independently are considered. First, the case for which P_2 is 99.26 is described. The other dimensionless parameters in this case are $Re = 0.40$, $P_1 = 11.12$, $P_3 = 11.12$, $Ma = 0.112$, and $P_4 = 8.92$, respectively. As P_4 is greater than one, the particle-particle interactions dominate and the particles form chains, as can be seen in Figure 4.13 at $t = 3.0$ s. The

chains of particles rearrange and some chains even merge to form longer chains. Notice that some chains extend from one electrode to the other, and after they are formed remain almost stationary, and the particles do not collect at the electrode edges.

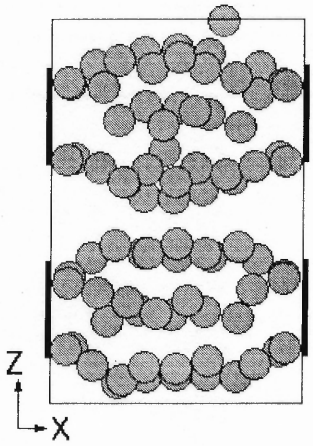

Figure 4.13 The front view of particles at $t = 3.0$ s. The parameters are $P_2 = 99.26$ and $P_4 = 8.92$. The chains extend from one electrode to the other on the opposite side.

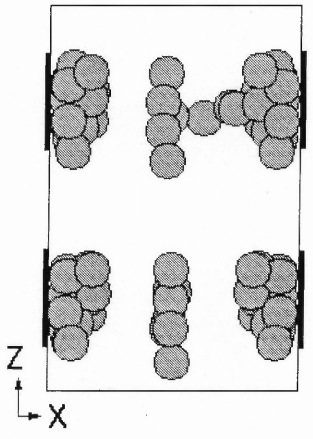

Figure 4.14 The side view of particles collected near the electrode edges at $t = 3.0$ s. The parameters are $P_2 = 0.99$ and $P_4 = 0.089$.

Next, the magnitude of the parameter P_2 is decreased to 0.99. The other dimensionless parameters for this case are $Re = 0.40$, $P_1 = 11.12$, $P_3 = 11.12$, $Ma = 11.2$, and $P_4 = 0.089$. The particles move relatively quickly toward the edges of the electrodes

without forming chains, as can be seen in Figure 4.14 at $t = 3.0$ s. Here also, as in Figure 4.12, the particles in the middle of the domain are not collected.

We may therefore conclude that for $P_4 > O(1)$ it may not be possible to remove particles because of the formation of particle chains. Of course, these results are for modestly concentrated suspensions and the particle-particle interaction force decreases with decreasing solids fraction. Therefore this effect may not be present in very dilute systems.

CHAPTER 5

EXPERIMENTS: DIELECTROPHORETIC CLUSTERING REGIMES OF VIABLE YEAST CELLS – PARTICLE CHAINS AND AGGLOMERATES

In this chapter, the results of the experimental study that shows the transient clustering behavior of viable yeast cells in a dilute suspension suddenly subjected to a nonuniform AC electric field of a microelectrode device are presented. The aim of the experiment is to identify the two regimes, as discussed in the previous chapter, where particle chaining will and will not occur. The frequency of the applied electric field is varied to identify the two distinct regimes of positive dielectrophoresis. In both regimes, the yeast cells eventually cluster at the electrodes' edges, but their transient behavior as well their final arrangement is quite different. Specifically, when the frequency is much smaller than the cross-over frequency, the nearby yeast cells quickly rearrange in well defined chains which then move toward the electrodes' edges and remain aligned as elongated chains at their final location. However, when the frequency is close to the cross-over frequency, cells move individually towards the regions of collection and simply agglomerate along the electrodes' edges. Analysis of the experiments show that in the first regime both the dielectrophoretic force and the mutual dielectrophoretic force, which arises due to the electrostatic particle-particle interactions, are important. In the second regime, on the other hand, the dielectrophoretic force dominates.

5.1 Experimental Setup and Materials

5.1.1 Microfluidic Device

The device used for the experiments is a microfluidic platform for manipulating micro and nanoscale particles. The device is an integrated dual-microelectrode array chamber which was designed and fabricated using standard micro-fabrication processing techniques. Starting with a silicon wafer, 50 nm of dry thermal oxide was grown onto the wafer followed by 150 nm of stoichiometric nitride for insulation purposes. Planar gold electrodes were then realized by evaporating a 20 nm chromium layer followed by a 250 nm gold thin film layer onto the insulating oxide layer of the wafer. Photo-resist was spun on the wafer and then lithographic patterning of the electrode geometry definition was performed using a photo mask plate (Compugraphics, CA). An acetone lift-off process was used to define the microelectrodes and remove excess gold and photoresist from the field area. Electrical connection pads were provided on the wafer in order to make external electrical connections while electrical connections to the pads were made by hand soldering 0.25 mm diameter wire to the 1 mm electrical connection busses on the chip. The device contains a total of sixteen different sets of microelectrodes, including four different geometrical designs with four different sizes of electrodes and spacing. The chip device can be enclosed in a chamber with inlet and outlet tubing to provide a fluid flow condition, or it can be operated in the static flow condition. The open static-flow condition was used for the study carried out in this paper.

The experiments reported below were performed using the periodic staggered microelectrode bar shown in Figure 5.1, with electrode width of 50 microns and an inter-electrode gap of also 50 microns. This microelectrode arrangement has well defined

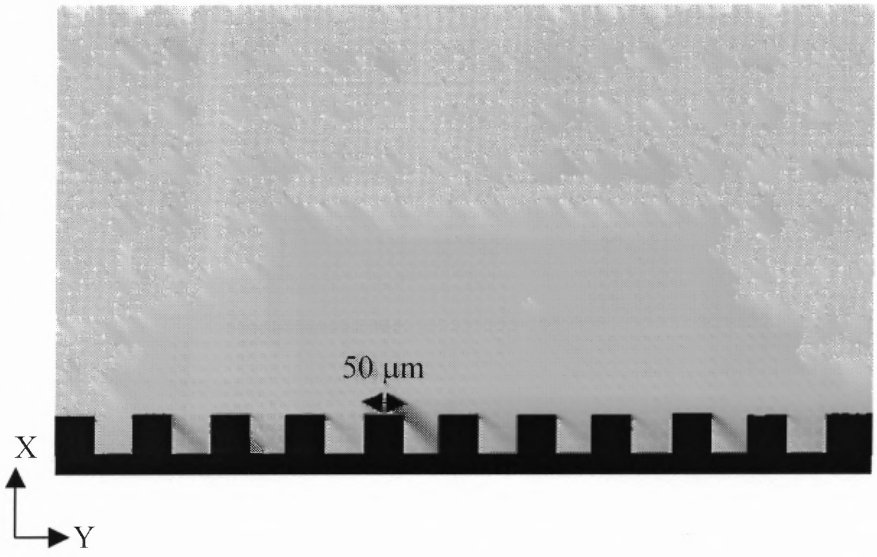

Figure 5.1 Schematic representation of the bottom surface of the device containing the microelectrode. The black geometry represents the electrode while the grey area corresponds to the silicon substrate. The yeast suspension is pipetted onto this surface.

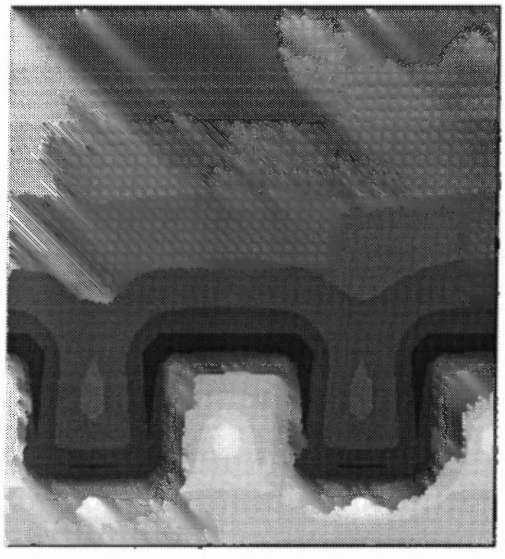

Figure 5.2 Contour plot of the log of the magnitude of the electric field on the bottom surface containing the electrode

electric field maxima at the edge of the electrodes and electric field minima in the bay regions between the edges, on top of the electrodes, as can be observed from the electric field contour plot displayed in Figure 5.2 (where only half of an electrode has been used for the computation). The electric field was computed using the numerical code presented in Chapter 3. The contour plot for log ($|\mathbf{E}.\nabla\mathbf{E}|$) and the lines of dielectrophoretic force for the device are shown in Figure 5.3.

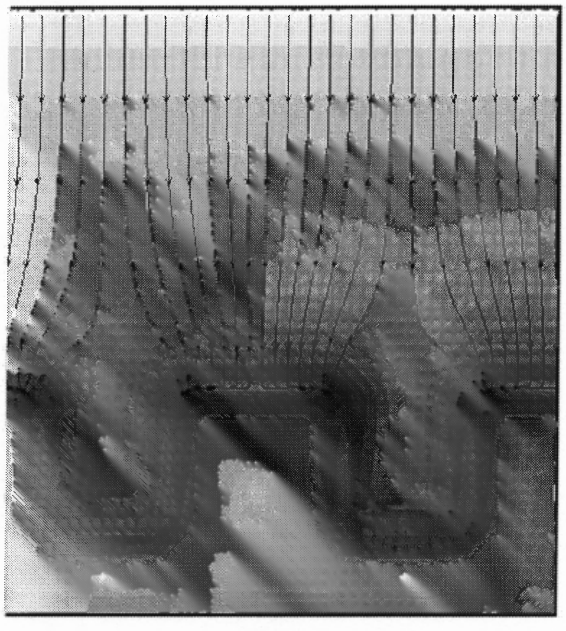

Figure 5.3 Contour plot of the electric field times the gradient of the electric field, also showing the dielectrophoretic force lines on the plane of the electrodes in the microdevice

5.1.2 Preparation of Viable Yeast Cell Suspension

The dielectric suspension to be used for the experimental study is a suspension of live yeast cells, as in references [3, 5, 41] and concentrate the analysis on the phenomenon of dielectrophoresis only, although other physical phenomena may be present as well [5]. Yeast cells, or *Saccharomyces cerevisiae*, were grown overnight at 32 ^{o}C in a dextrose

solution made with deionized water. The yeast cells were then harvested from the growing solution using a sterile pipette and resuspended in Millipore water. The suspension was then centrifuged and the supernatant liquid decanted. The cells were again resuspended in fresh Millipore water and centrifuged to isolate the cells. The process was repeated until the suspension conductivity was of the desired value of about 0.1 mS/m. The suspended live yeast cells had an average size of 2.5 micrometers.

5.1.3 Dependence of Dielectrophoretic Velocity on the Frequency of the Electric Field

In this section, the approach used for measuring the DEP force induced velocity of viable yeast cells from the video recordings made at a fixed location of the microdevice is decribed. The velocity was obtained for a set of frequencies between 500 Hz and 10 MHz. The time taken by an isolated cell to move over a fixed distance (between two fixed points) was measured and the average velocity was deduced by dividing the distance by the time taken. Cells close to others were excluded from this calculation so that electrostatic particle-particle interactions were negligible for the cells selected for the velocity calculation. For all frequencies investigated here particles move toward the electrode edges and therefore experience positive dielectrophoresis. Figure 5.4 reports velocity measurements averaged over a few cells, showing that the velocity of individual cells is about 6 μm/s at 1 kHz, and approximately zero at 10 MHz.

If we assume that the particle acceleration is negligible, equating the Stokes drag with the dielectrophoretic force gives

$$6\pi\eta\mathbf{a}\mathbf{U} = 2\pi a^3 \varepsilon_0 \varepsilon_c \beta \nabla \mathbf{E}^2$$

where U is the cell velocity. When the velocity of isolated cells is zero, the above equation implies that β is also zero, which, in our system, occurs at about 10 MHz. The latter frequency is then identified as being the cross-over frequency for the suspension. At low frequencies, the velocity of the cells is the highest, indicating strong β values as well, which then implies a dielectrophoresis force of large magnitude as well as strong electrostatic particle-particle interactions (mutual dielectrophoresis).

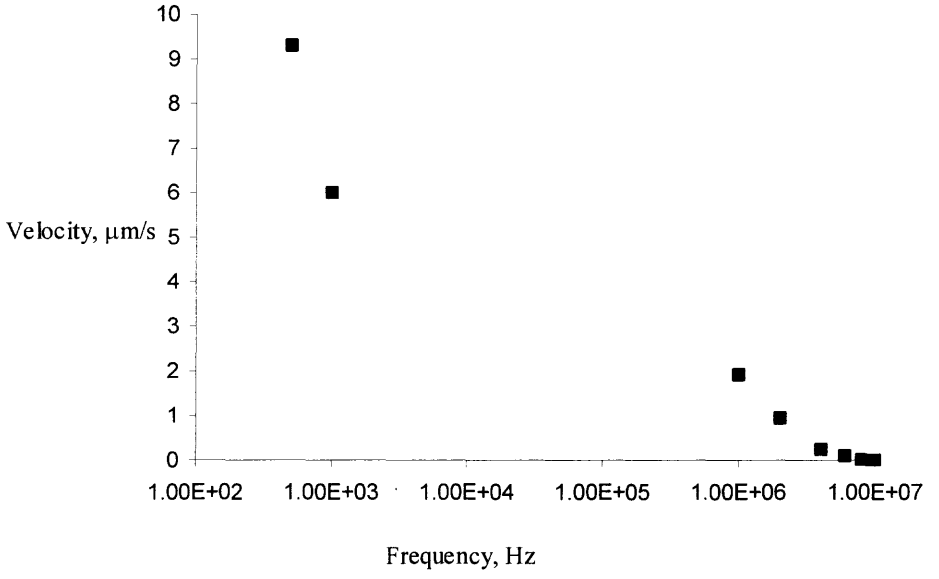

Figure 5.4 Measured averaged velocity of yeast cells as a function of the frequency of the applied electric field, showing high velocities at low frequencies and nearly zero velocities at about 10 MHz.

5.2 Results

A small volume of the yeast suspension prepared in the manner described above was pipetted and placed on the microelectrode structure. The suspension was then sealed with a cover slip and allowed to settle for a few seconds, and then the electrodes were energized. A variable frequency AC signal generator (BK Precision Model 4010A) was

used to apply a voltage to the electrodes over a frequency range of 200 Hz to 10 MHz. The applied voltage was 4 volt P/P (peak-to-peak). The applied voltage, frequency, and resulting current were monitored with an oscilloscope and digital voltmeter connected in parallel with the electrodes. Observations of the dielectrophoretic motion for the electrode at the edge of the device were made and recorded using a Digital Color CCD camera connected to a Nikon Metallurgical MEC600 microscope.

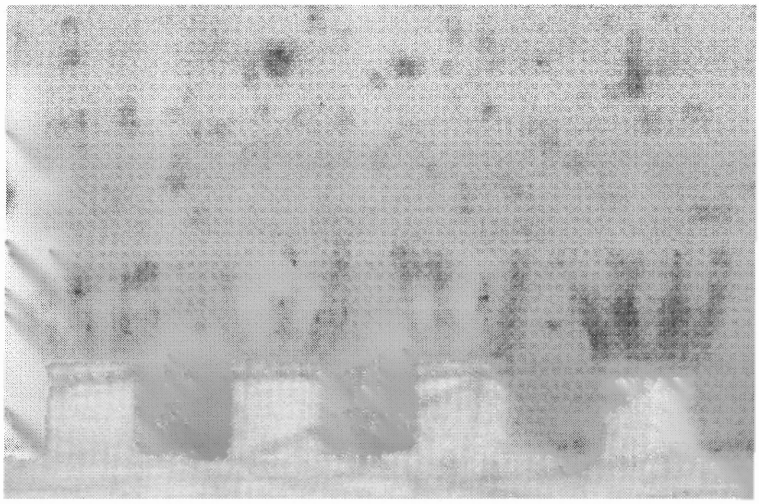

Figure 5.5 Visualization of the suspension after applying an electric field of frequency 500 Hz, at time $t = 5$ s,

First the results obtained for an applied frequency of 500 Hz are reported. In this case, the cells in the vicinity of the electrode start to collect at the electrode's edges immediately after the electric field is applied (Figure 5.5). The cells originally positioned away from the electrode also move towards the electrode, but in their transient motion,

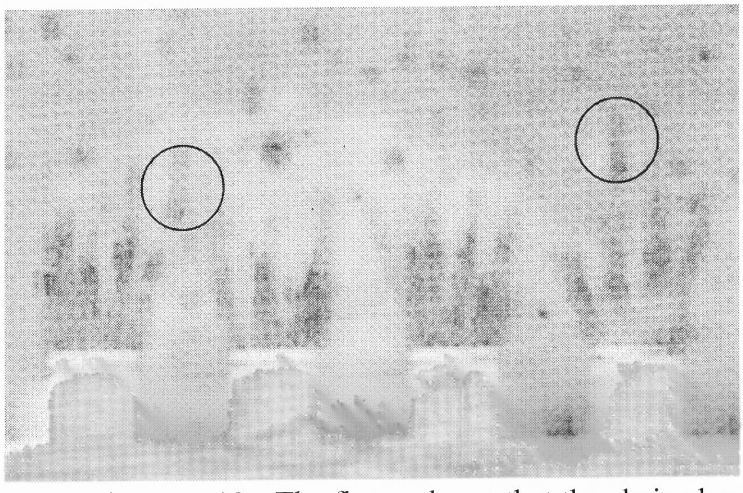

Figure 5.6 Chains at time, t = 10s. The figure shows that the chains have elongated in length and more chains are coming to join the chains at the electrodes

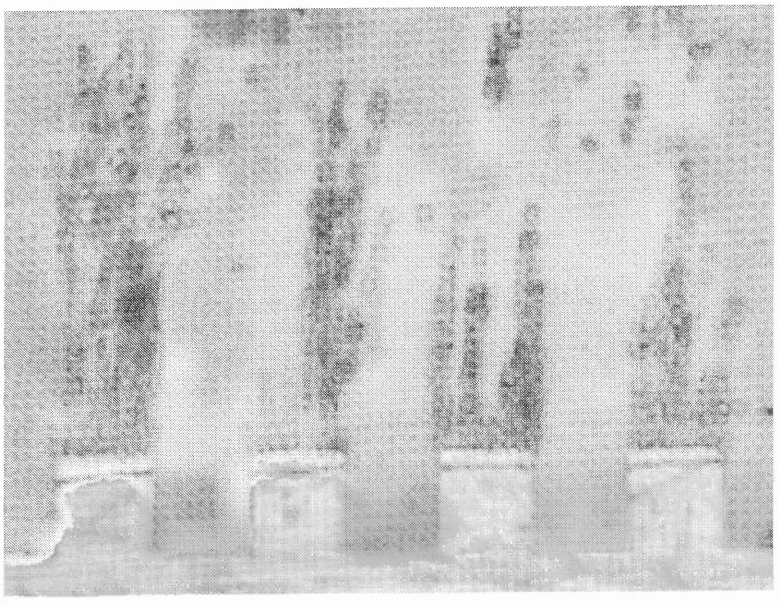

Figure 5.7 Particle chains at time t = 90 s

they come closer together and form chains parallel to the local electric field direction. Once the chains are formed, they move towards the edges of the electrode and are eventually collected. The chains at the edges of the electrode grow with time (clearly

seen in Figure 5.6 after 10s), as the smaller chains formed away from the edges merge with them. Some of the chains rearrange to form columns. After a certain time (see Figure 5.7 taken at t = 90 s), the chains and columns are very elongated. The average length of the chains at the electrode's edges at t = 90 s is about 175 μm, indicating that the chains contain approximately 35 cells at that time, while chains consisted of about 10 cells at t = 10 s.

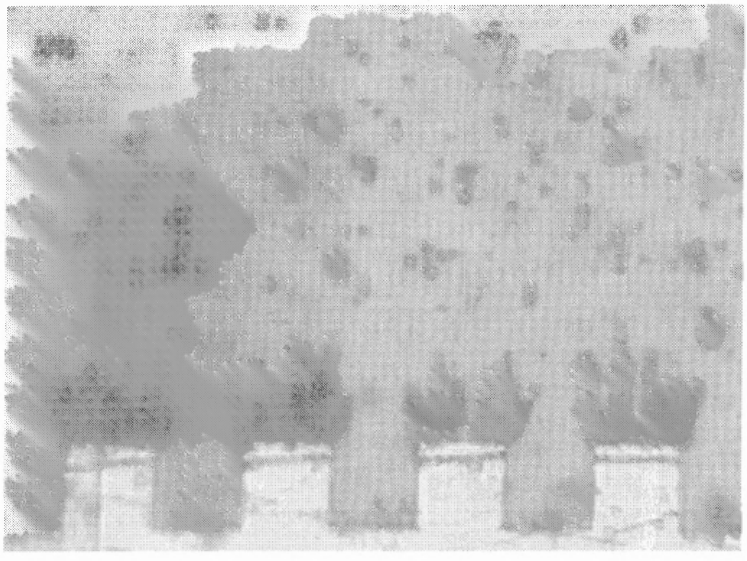

Figure 5.8. Particle chains at time, t = 5 s for frequency 1 kHz

Next, the results at the frequency of 1 kHz are described. Once the electric field is switched on, as expected, the cells near the electrode are immediately collected at the electrode's edges (Figures 5.8 - 5.10). The cells away from the electrode start moving towards the electrode while simultaneously forming chains by joining with neighboring cells as in the previous case. Although the cells and chains move more slowly than previously, they continue to move towards the electrodes' edges and eventually collect there. Some of the chains are also seen to realign as columns. The average length of the

chains at the electrode's edges at time t = 90 s is observed to about 150 μm (Figure 5.10), which is less than in the previous case at 1 kHz.

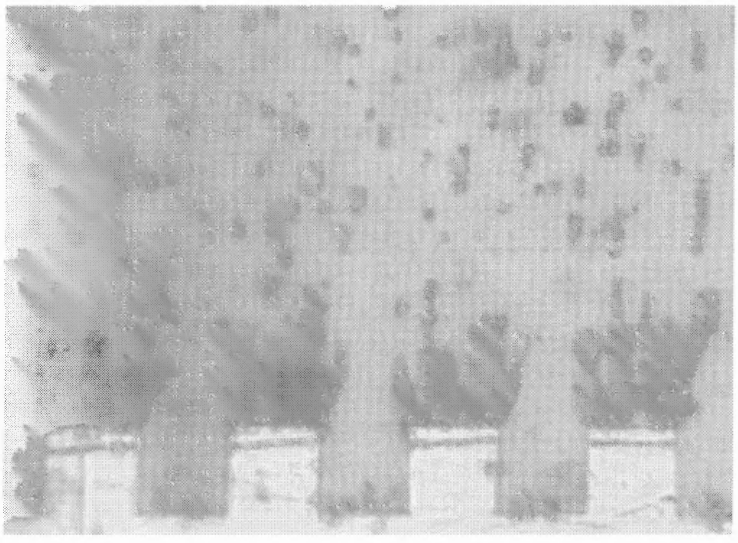

Figure 5.9 Particle chains at time, t = 10 s for frequency 1 kHz

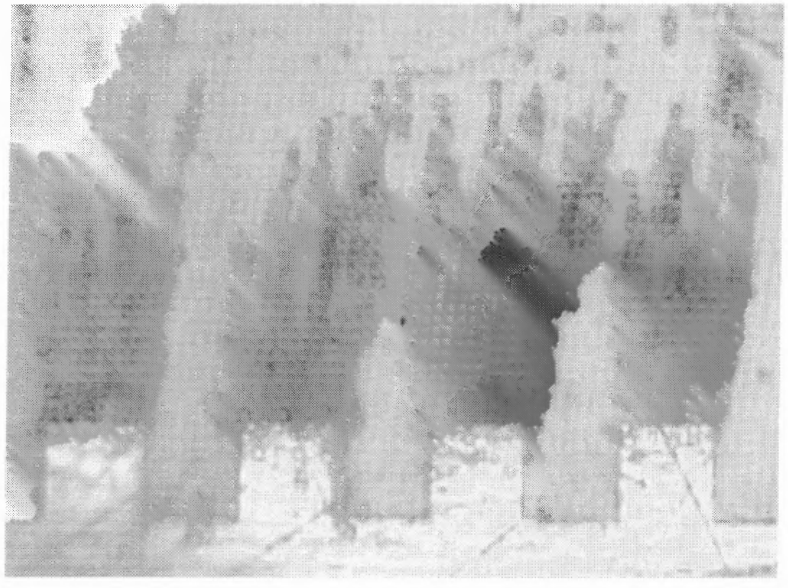

Figure 5.10 Particle chains at time, t = 90 s for frequency 1 kHz. The average chains length, however, is smaller than at 500 Hz at the same times.

Next, the results obtained at the frequency of 1 MHz are presented. Notice that the tendency of nearby cells to form chains is considerably diminished and the chains formed away from the electrode contain only 2-3 particles (Figure 5.11). The particles collected at the edges of the electrode at t = 90 s is shown in Figure 5.12. The average length of the chains at the edges of the electrode is approximately 40 μm.

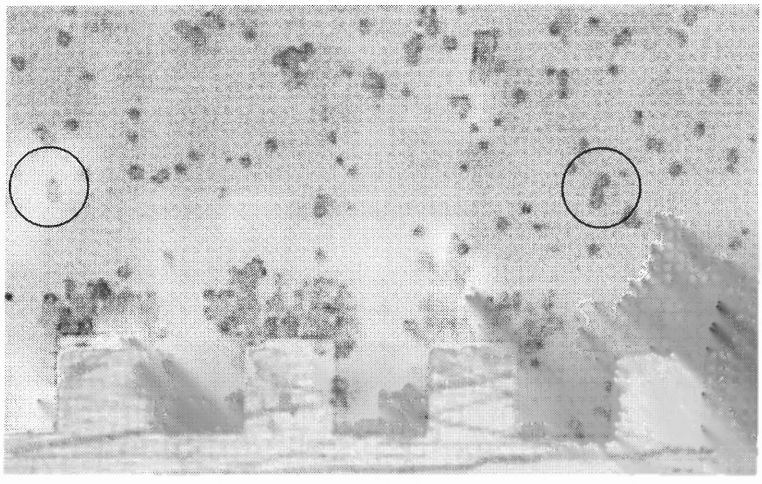

Figure 5.11 Particle chains formed at a frequency of 1 MHz at time t = 60 s, Clearly, the tendency for the cells to form chains is diminished considerably.

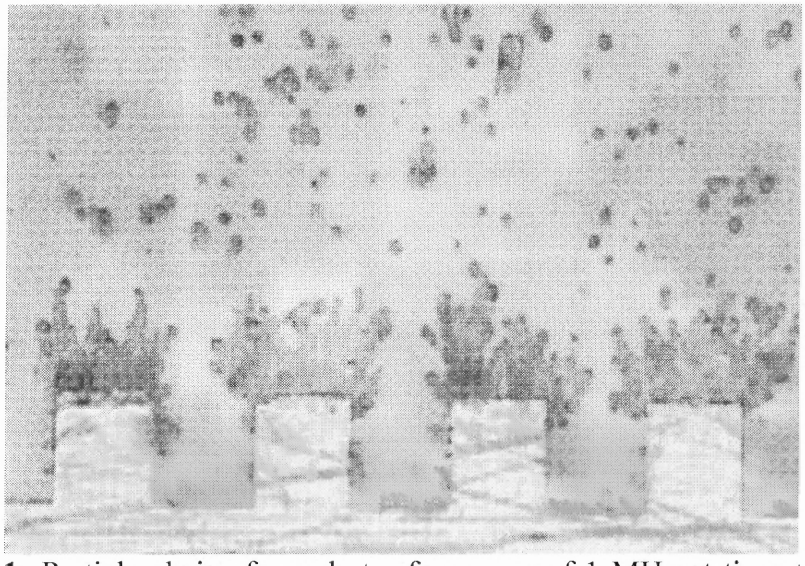

Figure 5.11 Particle chains formed at a frequency of 1 MHz at time t = 90 s, The average length of the chains formed at the edges of the electrodes is approximately 40 μm.

Next, let us consider the case where the applied electric field frequency is 2 MHz. Once the electric field is switched on, the cells close to the electrode get collected at the electrode's edges, but their velocities are much smaller than in the previous cases. The cells located far away from the electrode also move progressively towards the electrode, but they do not join together to form chains. Instead, they move individually, even when they are quite close to each other. The cells collected at the edges of the electrode at time t = 90 s are shown in Figure 5.13. From this figure it is clear that the cells collected at the electrode's edges do not regroup into chains. Instead, they are observed to agglomerate at the edges of the electrode with no clear structure, which demonstrates that the electrostatic particle-particle interactions are negligible.

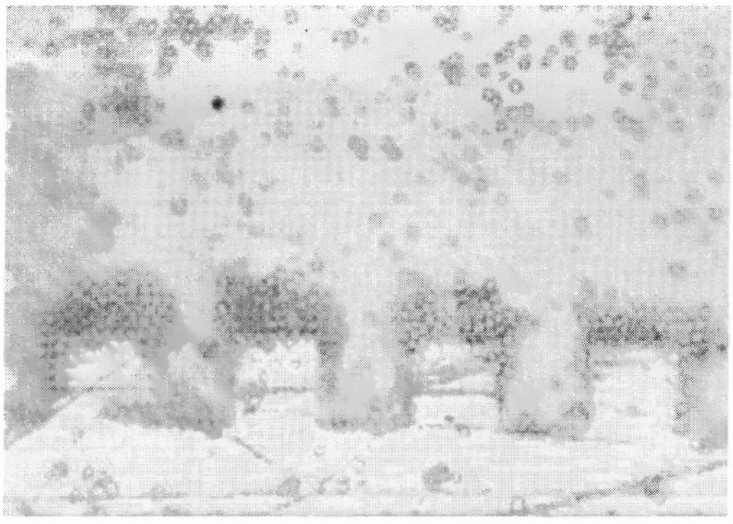

Figure 5.13 Particle collection for frequency 2 MHz at t = 90 s. While collection of particles is observed, particle chaining has mainly vanished, indicating that the electrostatic particle-particle interactions (mutual dielectrophoresis) are negligible.

As the frequency of the electric field is increased further, the dielectrophoretic force acting on the cells becomes very small and thus only a few cells are collected at the electrode's edges at t = 90 s. This can be observed in Figures 5.14 and 5.15 for the

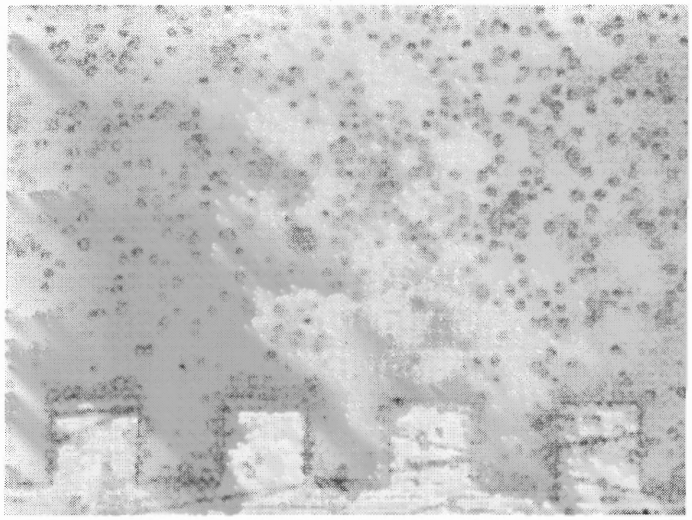

Figure 5.14 Particle collection for frequency 4 MHz at time, t = 90 s. The collection of particles is now weaker than in Figure 5.13, while no formation of chains is observed.

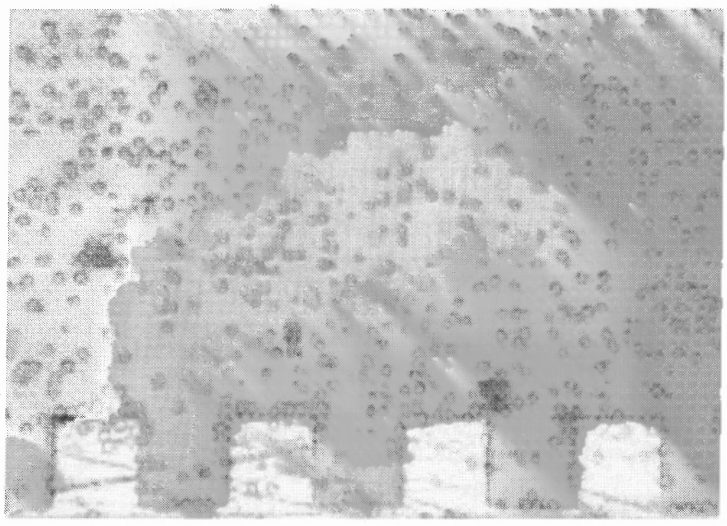

Figure 5.15 Particle collection for frequency 4 MHz at time, t = 90 s. Fewer particles are collected with no particle chains

frequencies of 4 MHz and 8 MHz, respectively. Finally, since the dielectrophoretic force becomes approximately zero at 10 MHz, no particle motion could be identified (see

Figure 5.16) as both the DEP and particle-particle interaction forces become approximately zero.

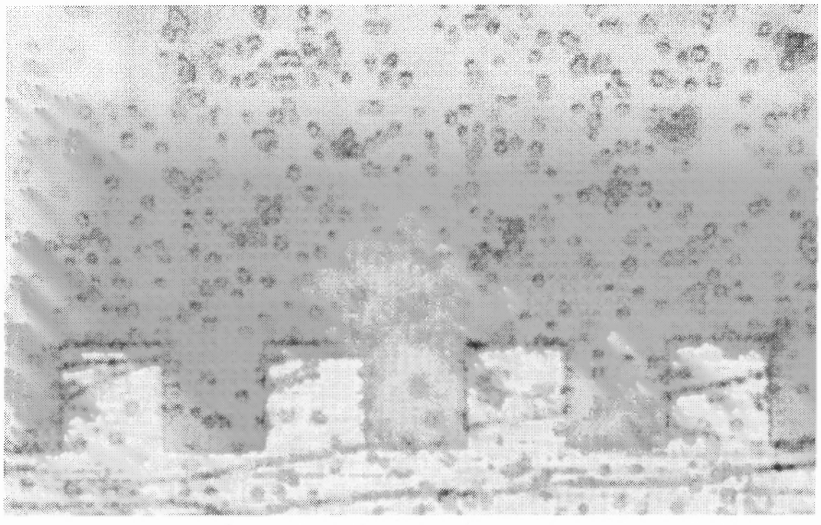

Figure 5.16 Particle collection at 10 MHz. Particles are hardly moving, and therefore not being collected on the electrodes' edges and not regrouping, indicating that both the dielectrophoretic force and the electrostatic particle-particle interactions are approximately zero in this case.

5.3 Discussion

The experiments show that when the frequency of the applied AC electric field is smaller than approximately 10 MHz the yeast cells are subjected to positive dielectrophoresis, and hence they cluster at the edges of the electrode. The nature of clusters, however, depends on the frequency of the electric field. When the frequency is around 1 kHz, the cells close to each other, including those away from the electrode, first organize in chains aligned parallel to the direction of the local electric field. Then these chains move towards the edges of the electrode and join with the chains already located at the edges of the electrode to form longer chains, which may contain as many as 35 cells.

On the other hand, when the frequency is around 4 MHz, which is close to the cross-over frequency of 10 MHz, cells move towards the edges of the electrodes individually; the tendency to form chains is not as noticeable. This shows that electrostatic particle-particle interactions do become negligible when the frequency is close to the cross-over frequency and β is much smaller than one.

These results are in agreement with the model presented in the Chapter 2 which predicts that the particle-particle interaction force depends on the second power of β, and therefore becomes negligible compared to the DEP force, which itself depends linearly on β, when β is small. We may therefore conclude that for frequencies close to the cross-over frequency it is possible to remove the particle-particle interaction force, and manipulate particles individually entirely by means of the dielectrophoresis force.

CHAPTER 6

DIELECTROPHORESIS OF NANOPARTICLES

6.1 Introduction

Dielectrophoresis as a means of manipulating nanoparticles is gaining popularity, as is evident from the increasing number of research papers published on the subject. The advantages of using dielectrophoresis for the purpose have already been explained in Chapter 1. Owing to this increasing interest in the subject, this entire chapter is dedicated to the numerical simulation of the dielectrophoresis of nanoparticles.

Here, the particles are subjected to electrostatic, hydrodynamic forces, and Brownian motion. Dielectric suspensions of nanoparticles subjected to both uniform and nonuniform electric fields are studied. The results of the simulations presented here show that in the case of uniform electric fields the evolution of the particle structures depends on the ratio of the electrostatic particle-particle interactions and Brownian forces. When this ratio is of the order of a hundred or more, particles form stable chains and columns whereas, when it is of the order of ten, the particle distribution is random. For the nonuniform electric field cases considered, the relative magnitude of Brownian forces is in the range such that it does not influence the eventual collection of particles by dielectrophoresis and the particular locations where the particles are collected. However, Brownian motion is observed to influence the transient particle trajectories. The deviation of the particle trajectories compared to those determined by the electrostatic and hydrodynamic forces alone is characterized by the ratio of Brownian and dielectrophoretic forces.

6.2 Brownian Force

One limitation of dielectrophoresis is that it requires an increase of the electric field intensity as the size of the particles decreases. This is due to the fact that the dielectrophoretic force acting on a particle is directly proportional to the volume of the particle. Therefore, as the particle size decreases, the dielectrophoretic force experienced by the particle also decreases. Meanwhile, it is well established that the intensity of the Brownian motion increases as particles become smaller. The effect of Brownian motion thus was first thought to overcome any deterministic motion due to the dielectrophoretic force on sub micrometer particles [3] and the minimum particle size required for dielectrophoretic motion was estimated to be around 4000–6000 $\mathring{A}$ under reasonable physical conditions.

Recent experimental observations, that have been possible due to advances in microfabrication and optical techniques, have demonstrated that the force required to produce a deterministic motion of the particles capable of overcoming the Brownian force is much lower than that previously estimated based on rough diffusion arguments [3]. For example, it has been demonstrated that the force required to manipulate Herpes simplex virus in a microelectrode array is in the range $1 - 2 \times 10^{-14}$ N [5]. Such results have led to a renewed interest in the dielectrophoretic manipulation of small particles such as viruses, DNA, latex spheres, etc. [5, 6]. More over, it is easy to generate the highly divergent strong electric fields required to manipulate the small particles in microdevices.

In addition to the dielectrophoretic force, there are other forces which need to be accounted for in determining the trajectory of particles suspended in a liquid medium and subjected to an electric field, as well as their time of collection. A detailed review of the various forces involved can be found in references [2, 5]. In this work, only Brownian, dielectrophoretic and hydrodynamic forces are considered.

As previously noted, the effect of dielectrophoresis is a translatory motion of the particles due to the nonuniformity in the applied electric field. However, if the externally applied electric field is uniform, it results in the formation of pearl-chains due to the mutual dielectrophoresis or interaction among the particles. The corresponding interaction force decays as r^{-4}, where r is the distance between the particles. Hence, when the distance between the particles is large, this force is negligible.

6.3 Governing Equations

In this section, the electrostatic forces that arise in uniform and nonuniform electric fields due to the polarization of particles are described, and the governing dimensional and dimensionless equations for both the particles and the fluid are stated. Also the approach used for modeling the Brownian force is discussed. Other than the Brownian force part, the governing equations are the same as in chapter 2 and Chapter 4 on numerical simulations. Nevertheless the complete governing equations and dimensionless equations are described, for the sake of completeness of this chapter.

Let us denote the domain containing a Newtonian fluid and N solid particles by Ω, the interior of the i^{th} particle by $P_i(t)$, and the domain boundary by Γ. The governing equations for the fluid-particle system are:

$$\rho_L\left(\frac{\partial \mathbf{u}}{\partial t}+\mathbf{u}\cdot\nabla\mathbf{u}\right)=\rho_L\mathbf{g}-\nabla p+\nabla\cdot(2\eta\mathbf{D}) \qquad \text{in } \Omega\backslash\overline{P(t)}$$

$$\nabla\cdot\mathbf{u}=0 \qquad \text{in } \Omega\backslash\overline{P(t)} \qquad (6.1)$$

$$\mathbf{u}=\mathbf{u}_L \qquad \text{on } \Gamma$$

$$\mathbf{u}=\mathbf{U}_i+\boldsymbol{\omega}_i\times\mathbf{r}_i \qquad \text{on } \partial P_i(t),\ i=1,\ldots,N \qquad (6.2)$$

Here $\mathbf{u}$ is the fluid velocity, p is the pressure, η is the dynamic viscosity of the fluid, ρ_L is the density of the fluid, $\mathbf{D}$ is the symmetric part of the velocity gradient tensor, $\mathbf{U}_i$ and ω_i are the linear and angular velocities of the i^{th} particle, and $\mathbf{g}$ is the acceleration due to gravity. The above equations are solved using the following initial conditions $\mathrm{u}|_{t=0}=\mathrm{u}_0$, where $\mathbf{u}_0$ is the known initial value of the velocity.

The linear velocity $\mathbf{U}_i$ and angular velocity ω_i of the i^{th} particle are governed by

$$m_i\frac{d\mathbf{U}_i}{dt}=\mathbf{F}_i+\mathbf{F}_{E,i}+\mathbf{F}_{B,i}$$

$$I_i\frac{d\boldsymbol{\omega}_i}{dt}=\mathbf{T}_i \qquad (6.3)$$

$$\mathbf{U}_i\,|_{t=0}=\mathbf{U}_{i,0}$$

$$\boldsymbol{\omega}_i\,|_{t=0}=\boldsymbol{\omega}_{i,0} \qquad (6.4)$$

where m_i and I_i are the mass and moment of inertia of the i^{th} particle, $\mathbf{F}_i$ and $\mathbf{T}_i$ are the hydrodynamic force and torque acting on the i^{th} particle, respectively, $\mathbf{F}_{E,i}=\mathbf{F}_{DEP,i}+\mathbf{F}_{D,i}$ is the net electrostatic force acting on the i^{th} particle and $\mathbf{F}_{B,i}$ is the Brownian force acting on the i^{th} particle. The dielectrophoretic force $\mathbf{F}_{DEP,i}$ acting on the i^{th} particle is given by (1.2) and $\mathbf{F}_{D,i}$ is the particle-particle interaction force on the i^{th} particle.

As noted above, Brownian motion becomes important as the size of the particle decreases to the submicrometer scale. This is due to thermal fluctuations at molecular-scales in the liquid medium which, in turn, induce random forces on the particles of a suspension. The standard approach for describing the Brownian motion is that derived from the Langevin equations (see, e.g., Ermak and McCammon [101]).

The motion of the i^{th} particle is described by the following Langevin equation

$$m\frac{d\mathbf{U}_i}{dt} = \mathbf{F}_{E,i} + \mathbf{F}_{H,i} + \mathbf{F}_{B,i}(t) \tag{6.5}$$

where $\mathbf{F}_{E,i}$ is the electrostatic force acting on the particle, $\mathbf{F}_{H,i}$ is the hydrodynamic force and $\mathbf{F}_{B,i}(t)$ represents the Brownian force on the particle. The Brownian force $\mathbf{F}_{B,i}(t)$ satisfies $\left\langle \mathbf{F}_{B,i,\alpha}(0)\mathbf{F}_{B,i,\beta}(t)\right\rangle = 12\pi\eta a k_B T\delta_{\alpha\beta}\delta(t)$ and $\left\langle \mathbf{F}_{B,i,\alpha}\right\rangle = 0$, where k_B is the Boltzmann's constant and T is the temperature.

In our numerical simulations, the time step dt is chosen so that it is greater than the momentum relaxation time, i.e., $dt >> \frac{mD}{k_B T}$ where m is the mass of the particle and $D = \frac{k_B T}{6\pi\eta a}$ is the diffusivity. The momentum relaxation time for our system is of the order of 10^{-9} s.

In the simulations the Brownian force on the i^{th} particle is given by (see [102])

$$F_{B,i} = \xi(12\pi\eta a k_B T/\tau)^{1/2} \tag{6.6}$$

where $\tau = dt$ is the time step used in the numerical integration scheme and ξ is a Gaussian random vector.

As mentioned above, this work is restricted to the case where the particles are spherical, and therefore it is not required to keep track of the particle orientation. The particle positions are obtained from

$$\frac{d\mathbf{X}_i}{dt} = \mathbf{U}_i \tag{6.7}$$

$$\mathbf{X}_i\,|_{t=0} = \mathbf{X}_{i,0} \tag{6.8}$$

where $\mathbf{X}_{i,0}$ is the position of the i^{th} particle at time $t = 0$. Furthermore, it is assumed that all particles have the same density ρ_p, and since they have the same radius, they also have the same mass, m.

The above equations can be nondimensionalized by assuming that the characteristic length, velocity, time, stress, angular velocity and electric field scales are a, U, a/U, $\eta U/a$, U/a and E_0, respectively. The gradient of the electric field is assumed to scale as E_0/L, where L is the distance between the electrodes which is the same as the domain width. The Brownian force is assumed to scale as $(12\pi\eta a k_B T/\tau)^{1/2}$. The nondimensional equations, after using the same symbols for the dimensionless variables, are:

$$Re\left(\frac{\partial \mathbf{u}}{\partial t} + \mathbf{u}\cdot\nabla\mathbf{u}\right) = -\nabla p + \nabla\cdot\boldsymbol{\sigma} \qquad \text{in } \Omega\backslash\overline{P(t)}$$

$$\nabla\cdot\mathbf{u} = 0 \qquad \text{in } \Omega\backslash\overline{P(t)} \tag{6.9}$$

$$\frac{d\mathbf{U}}{dt} = \frac{6\pi\eta a^2}{mU}\int\left(\frac{-p\mathbf{I}+\boldsymbol{\sigma}}{6\pi}\right)\cdot\mathbf{n}\,ds + \frac{4\pi a^4\varepsilon_0\varepsilon_c\beta\,|E_0|^2}{mU^2L}(\mathbf{E}\cdot\nabla\mathbf{E}) + \frac{3\pi\varepsilon_0\varepsilon_c a^3\beta^2\,|E_0|^2}{4mU^2\,|r_{ij}|^4}(\mathbf{F}_D) + \frac{(12\pi\eta a k_B T/\tau)^{1/2}a}{mU^2}\xi \tag{6.10}$$

$$\frac{d\boldsymbol{\omega}}{dt} = \frac{5\eta a^2}{2m\mathbf{U}}\int(x-X)\times\left[(-p\mathbf{I}+\boldsymbol{\sigma})\cdot\mathbf{n}\right]ds \tag{6.11}$$

The above equations contain the following dimensionless parameters:

$$Re = \frac{\rho_L U a}{\eta}, \qquad P_1 = \frac{6\pi\eta a^2}{mU}, \qquad P_2 = \frac{3\pi\varepsilon_0\varepsilon_c\beta^2 a^3 \mid E_0 \mid^2}{4mU^2}, \qquad P_3 = \frac{4\pi\varepsilon_0\varepsilon_c\beta a^4 \mid E_0 \mid^2}{mU^2 L},$$

$$P_6 = (12\pi\eta a k_B T/\tau)^{1/2}\frac{a\xi}{mU^2} \text{ and } h' = \frac{L}{a}.$$

In Chapter 4, the evolution of particle scale structures for different relative magnitudes of the parameters P_1, P_2 and P_3 were discussed. Specifically, the influence of the parameter P_4 (that is the ratio of P_2 and P_3) on the particle structure was studied. In this chapter, the influence of Brownian forces on the particle structure formation is analyzed numerically. Hence, the parameter that is of primary interest to us is P_6. Also, three additional parameters $P_7 = P_2/P_6$, $P_8 = P_3/P_6$, and $P_9 = P_1/P_6$, are also defined. The parameters P_7 and P_9 are related to the parameters λ and Peclet number Pe defined for uniform electric fields in [103, 104], and the parameter P_7 is the inverse of the parameter B defined in [105].

6.4 Results

In this section, the results obtained from the numerical simulations for electrorheological suspensions of nanoparticles are discussed. Results are presented for both uniform electric field and nonuniform electric field cases. The results obtained are used to study the importance of the Brownian force in determining the particle scale structure formation and to study the conditions under which the Brownian force can be ignored. The results discussed in this chapter are for cases with no bulk fluid flow and therefore the primary interest is in studying the particle structure evolution upon variation of the parameters P_7 and P_8.

The domain used for the simulations is the same as used for the simulations to study the importance of parameter P_4 in chapter 4. The fluid velocity is assumed to be zero on the sidewalls of the domain and periodic along the z-direction. The electric field is also assumed to be periodic in the z-direction. The electrostatic and hydrodynamic forces include contributions from the periodic images in the z-direction.

The dynamic fluid viscosity η is assumed to be 0.01 Poise and the particle diameter and density are 200 nm and 1.01 g/cm^3, respectively. The fluid density is ρ_L = 1.0 g/cm^3. Gravity is ignored, as the density of particles is close to that of the fluid and the particle diameter is small. The initial fluid and particle velocities are set to zero. The domain is discretized using a regular pseudo P2-P1 tetrahedral mesh and the number of nodes used is 208,065. The time step used is $5\text{x}10^{-4}$ s, which is greater than the momentum relaxation time.

6.4.1 Uniform Electric Field

It is well known that when electrorheological fluids are subjected to a uniform electric field, the particles align in the direction of the electric field forming first chains and then columns as two or more chains merge together. This rearrangement of the particles into chains and columns results in a dramatic increase in the viscosity of the fluid. Brownian forces can however hinder the formation of the particle chains. This is more prominent for small particles, particularly nanometer-sized particles, as the relative magnitude of the Brownian force increases with decreasing particle size. In order to study this phenomenon, simulations were performed by varying the parameter P_7, which is the ratio of electrostatic particle-particle interactions and Brownian force.

First, case where the value of the parameter P_7 is 95.2 is discussed. The values of the other parameters for this case are Re = 1.78 x 10^{-3}, P_1 = 2.53, P_2 = 12.8, P_6 = 0.135,

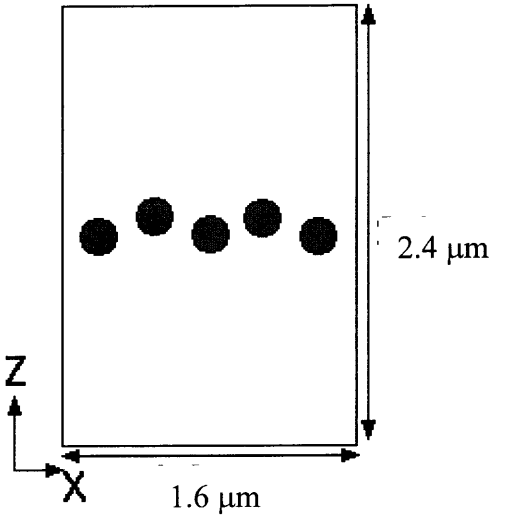

Figure 6.1 Initial arrangement of the particles in the uniform electric field

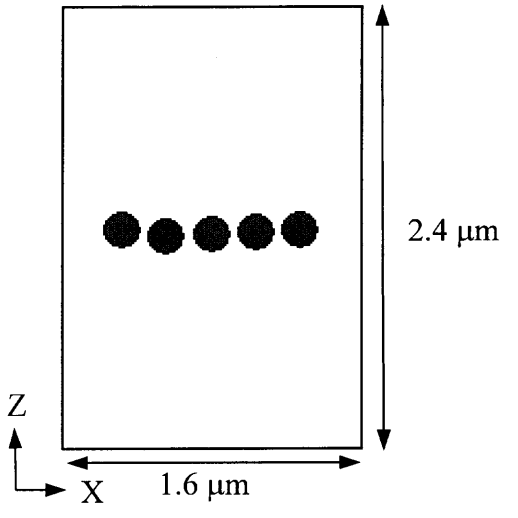

Figure 6.2 Chain formation for P_7 = 95.2 shown at t = 0.5 s

and P_9 = 18.8. Five particles are arranged in a staggered manner in a domain of size 1.6 μm x 0.4 μm x 2.4 μm as shown in the Figure 6.1. The uniform electric field is applied in the x direction. During the simulation, the particles are observed to exhibit a random motion due to the Brownian force. However, in this case the Brownian force is not sufficiently strong to overcome the particle-particle interaction force and the particles come together to form a chain parallel to the electric field at time t = 0.25 s. The chain formed does not break as time further increases and the particles stay together for the rest of the simulation. The position of the particles at time t = 0.5 s is shown in Figure 6.2.

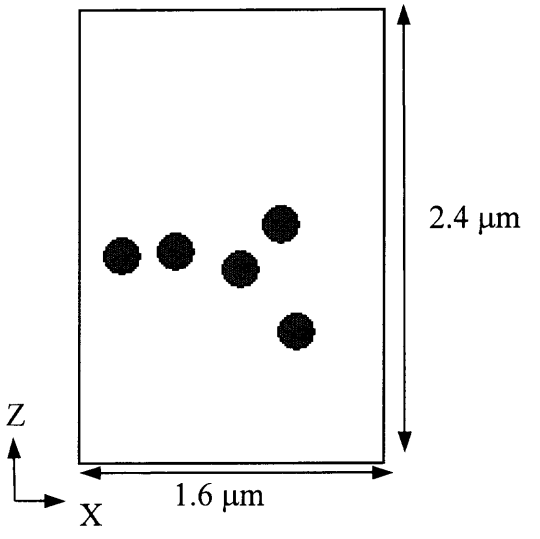

Figure 6.3 Random position of the particles for the case with P_7 = 12 at t = 0.5 s

Next, simulations were performed with the same number of particles in the domain, but this time the value of the parameter P_7 is decreased by a factor ten so that it is now 9.52. The values of the other parameters are Re = 1.78 x 10^{-3}, P_1 = 2.53, P_2 = 12.8, P_6 = 1.35, and P_9 = 1.88. In this case, although the particles tend to come together as chains as in the previous case, the Brownian force overcomes this tendency and the

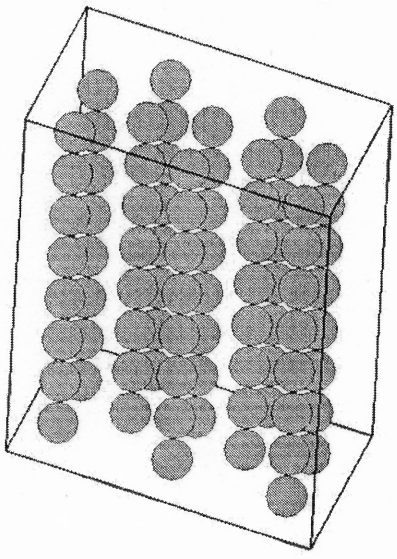

Figure 6.4 Initial periodic arrangement of the particles in the domain for the study of importance of parameter P_7

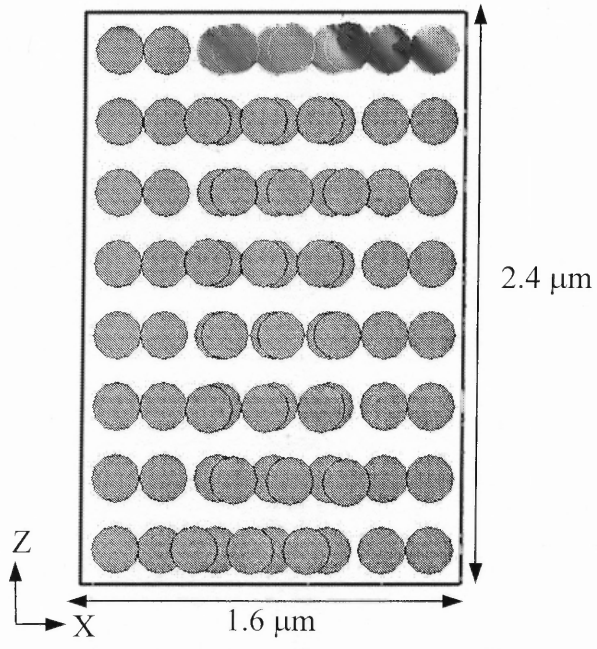

Figure 6.5 Straight chains of particles formed at time $t = 0.7$ s, in the direction of electric field in the case of no Brownian force

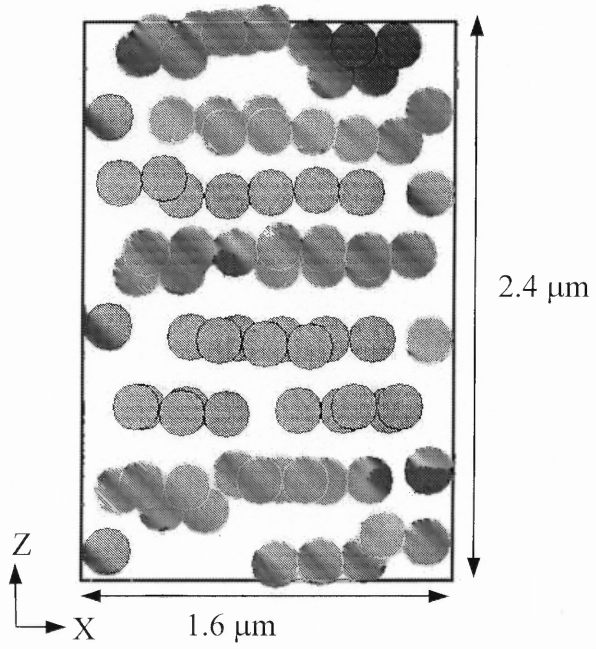

Figure 6.6 Random arrangement of the particles where $P_7 = 9.52$ and $t = 0.7$ s

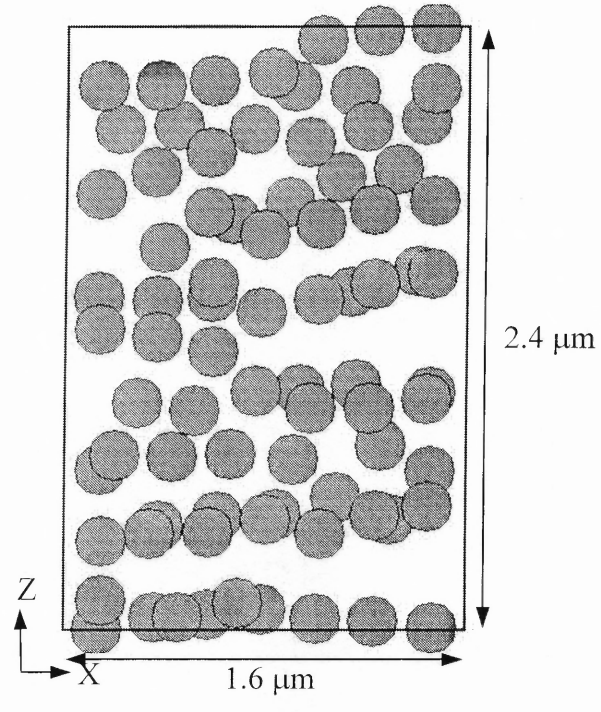

Figure 6.7 Random arrangement of the particles in the case where $P_7 = 95.2$ and $t = 0.7$ s. As can be noticed from the figure, the randomness of the particles has increased

particles are thrown randomly in the domain. The position of the particles at time $t = 0.5$ s is displayed in Figure 6.3, which shows the random arrangement of the particles in the domain.

Additional simulations were performed with more particles in the domain, of which results for cases with 80 particles for which the ratio P_7 is 9.52 and 95.2 are presented here. In this study, comparisons of the results of a simulation taking into account only particle-particle interactions and no Brownian force are performed with those obtained where both the particle-particle interactions and Brownian force are present. As before, the electric field is applied in the x direction. In a domain of size 1.6 μm x 0.8 μm x 2.4 μm, the particles are initially arranged in a periodic manner as shown in Figure 6.4. As time increases, we observe that in the first case the particles come together and arrange themselves as chains in the x- direction, as shown in Figure 6.5 for time, $t = 0.7$ s. On the other hand, in the other cases with $P_7 = 9.52$ and $P_7 = 95.2$ we obtain a random arrangement of the particles. The particle structure for both cases at time $t = 0.7$ s is shown in Figure 6.6 and Figure 6.7, respectively.

The above simulations show that P_7 determines the distribution of particles in the domain and the particle-particle interaction force and Brownian force are competing with each other. Depending on the relative strength of the two forces, the particles will either form chains or will be randomly distributed in the domain.

6.4.2 Nonuniform Electric Field

The analysis in the case of a nonuniform electric field is more difficult than in the case of a uniform field as two parameters (P_7 and P_8) are involved, instead of one. Upon the

action of the dielectrophoretic force the particles will either move to the regions of high electric field, in the case of positive dielectrophoresis, or move to the regions of low electric field, in the case of negative dielectrophoresis. In the previous simulations described in Chapter 4 it was shown that at sufficient strengths of particle-particle interactions, this behavior can be altered with particles forming chains spanning from one electrode to the opposite one, thus possibly clogging the entire domain. In this study, the simulations are restricted to a regime where the particle-particle interactions are relatively smaller than the dielectrophoretic force and hence the particles can be easily collected in the regions of high or low electric fields depending on their relative polarities. Specifically, the simulations are concentrated on varying the parameter P_8 only.

First, a case where the value of the parameter P_8 is 4.27×10^3 is presented. The values of P_7 and P_9 for this case are 3.81×10^3 and 5.57, respectively, while the Reynolds number is 5.27×10^{-2}. The values of other parameters are $P_1 = 85.4$, $P_2 = 5.84 \times 10^4$, $P_3 = 6.55 \times 10^4$ and $P_6 = 15.3$. Fourty particles are arranged in the domain in a periodic manner similar to the eighty particle case. The particles have a β value of -0.297 and the volume fraction is 0.16. There are two pairs of electrodes in the domain, each 0.6 μm long, located at z = 0.3 μm and z = 1.5 μm. The electrodes span the entire depth of the domain in the y- direction and thus the electric field does not vary in the y- direction. The dielectrophoretic force and the lines of force generated by this arrangement of the electrodes are shown in Figure 4.8, while the electric field generated for this arrangement of the electrodes is shown in Figure 4.7.

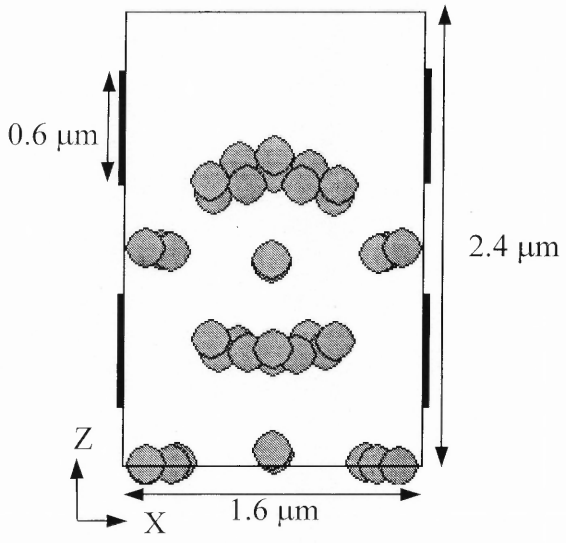

Figure 6.8 Particle positions at time $t = 0.2$ s for the case with $P_8 = 4.27 \times 10^3$ showing the organized motion of the particles along the lines of force

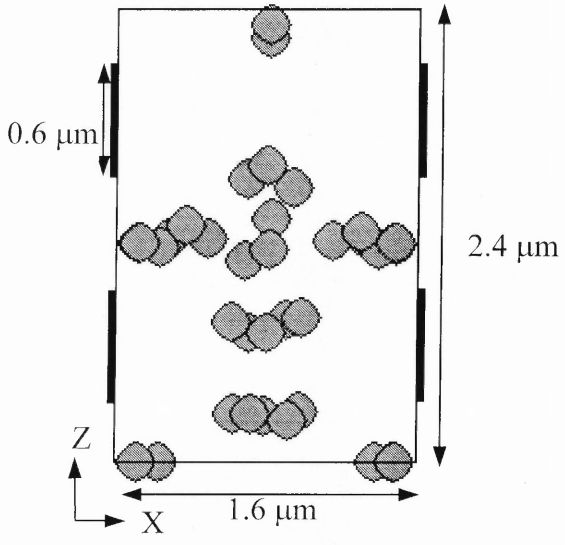

Figure 6.9 Particle positions at time $t = 0.75$ s for the case with $P_8 = 4.27 \times 10^3$

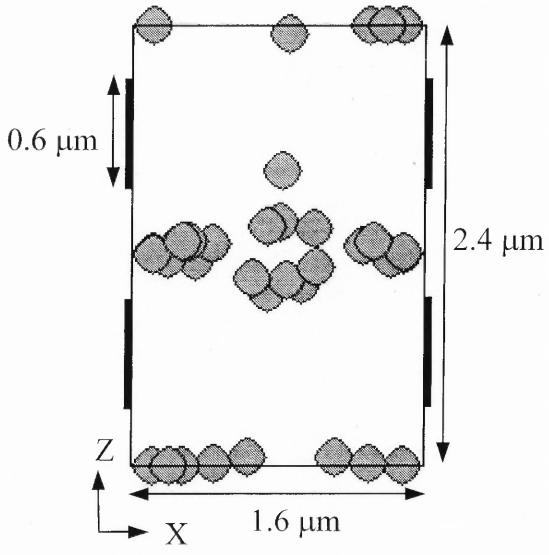

Figure 6.10 Particle positions at time t = 1.75 s for the case with $P_8 = 4.27 \times 10^3$

Upon simulation, it can be observed that the particles gather into chains under the influence of particle-particle interactions as well as follow the dielectrophoretic force lines, thus moving to the regions of minimum magnitude of the electric field located on the walls of the domain and defined by (x = 0, z = 1.2), (x = 1.6, z = 1.2), (x = 0, z = 0) and (x = 1.6, z = 0). The particle positions at time t = 0.2 s is displayed in Figure 6.8 which shows the organized motion of the particles along the lines of force as well as the particle chains. Even though the particles are able to come together as chains, they show small vibrations throughout their motion due to the random Brownian force. The latter, however, is not sufficiently strong to fully overcome the particle-particle interactions and therefore the particles stay together. The particles continue their motion towards the electric field minima in an organized manner as can be seen from Figures 6.9 and 6.10, and finally they all get collected at the electric field minima.

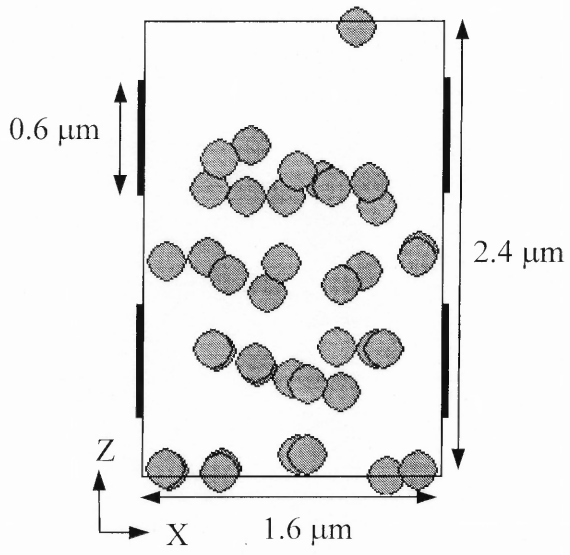

Figure 6. 11 The uncontrolled motion of the particles and the particle positions at t = 0.2s for $P_8 = 42.7$

Next, the previous case is repeated again, but this time with an increased Brownian force. The value of the parameter P_8 is now 42.7 while the values of P_7 and P_9 are 38.1 and 0.355, respectively. The Reynolds number is 0.336. The values of other parameters are P_1 = 13.4, P_2 = 1.43 x 10^3, P_3 = 1.61 x 10^3 and P_6 = 37.7. Once the simulations begin, the particles start moving towards the electric field minima in a random manner, without forming any particle chain. The particle positions at time t = 0.2 s is shown in Figure 6.11. For the parameter values considered, even though the final aggregation of particles in the regions of electric field minima is not altered by the increased Brownian force, their motion has a strong random component.

6.5 Discussion

In this chapter the numerical scheme based on the Distributed Lagrange multiplier method was used to study the dynamical behavior of dielectric suspensions of nano

particles subjected to both uniform and nonuniform electric fields. The simulation results are used to study the dependence of the particle scale structure evolution on the Brownian force. Comparisons are made based on the parameters P_7 and P_8 corresponding to the ratio of Brownian and electrostatic particle-particle interaction forces, and the ratio of the Brownian and dielectrophoretic forces, respectively. The results presented here show that in the case of a uniform electric field when P_7 is of order a hundred or more, the particles form chains parallel to the uniform electric field and when P_7 is of order ten, the particles are randomly distributed in the domain. In the case of a nonuniform electric field, the simulations show that the particles move either to the regions of maximum magnitude of the electric field or to the regions of minimum magnitude of the electric field depending on their polarities. However, for large values of the parameter P_8, the motion of the particles is nearly deterministic and strongly controllable, whereas for smaller values of this parameter a random motion of the particles is clearly superimposed on their deterministic trajectory, which render their guidance more difficult.

CHAPTER 7

IMPROVEMENT OF ELECTRIC FIELD SOLUTION BY METHOD OF IMAGES

7.1 Overview

In this chapter the method of images is used to correct the electric field distribution when the particles are close to the domain walls. This correction is needed because, when a particle, modeled as a dipole, comes close to the wall the electric field at the wall is modified, and is no longer the same as prescribed by the boundary conditions. The results of this numerical scheme are compared with those for the scheme described earlier, which does not account for the images. Simulations show that, as expected, more than a few diameters away from the sidewalls the effect of the images is negligible. Simulations also reveals that for suspensions of low concentrations, straight chains parallel to the applied electric field are formed when images are not accounted for and branched chains are formed when images are included. For suspensions of higher concentrations the particle chains and columns are seen to be broken in the former case, whereas in the latter case the chains and columns are seen to be stronger spanning the entire width of the domain.

7.2 Governing Equations

In this section, the electrostatic forces including the image forces that arise in uniform electric field due to the polarization of particles are discussed. The governing equations for the particles and fluid are the same as before.

As already mentioned, in this dissertation the method of images is used to ensure that the electric field at the domain boundaries do not deviate from the prescribed value when a polarized particle is placed close to the boundary.

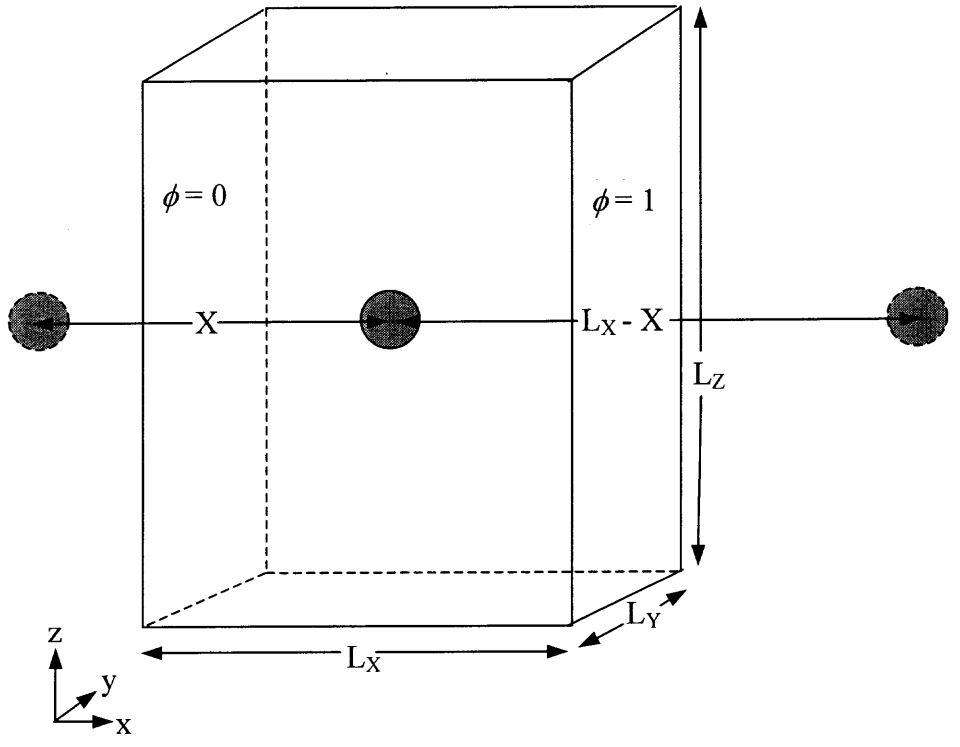

Figure 7.1 Figure showing the domain used for the simulation and the particle and the two images. The potential boundary condition on the left wall is $\phi = 0$, and on the right wall is $\phi = 1$.

Consider a dielectric particle of radius a, inside a box shaped domain as shown in figure 7.1. The particle situated inside the domain is considered to be a point dipole. The uniform electric field is applied in the x direction and the domain is considered to be periodic in the z- direction. The fluid velocity is assumed to be zero on the sidewalls of the domain and periodic along the z-direction. The electric field is also assumed to be periodic in the z-direction. The electrostatic and hydrodynamic forces include

contributions from the periodic images in the z-direction. The left wall is grounded whereas the right wall is at a potential of 1 volt. The particle inside the domain alters the potential boundary conditions on the left and right side walls. The boundary conditions on the left and right walls are restored by introducing images of the dipole on the other side of the boundaries as shown in figure 7.1. Only one image per side of the boundary is introduced for the present study.

Then, the net electrostatic force acting on a particle will be the force due to the presence of the other particles and also their images. Typically, the electric field at position x of particle i is given by

$$\mathbf{E}(x_i) = \mathbf{E}_0(x_i) + \mathbf{E}_p(x_i), \tag{7.1}$$

where $\mathbf{E}_0(x_i)$ is the applied electric field at x_i when no particles are present and $\mathbf{E}_p(x_i)$ is the electric field due to the other particles and images in the domain. Then the dipole moment of the particle at x_i can be written as:

$$\mathbf{p}_i = \left[4\pi\varepsilon_0\varepsilon_c\beta a^3 \mathbf{E}_0(x_i) + \sum_{\substack{j=1 \\ j\neq i}}^{N} \mathbf{p}_j \left(f(x_j, x_i) + f\left(x_j^{im1}, x_i\right) + f\left(x_j^{im2}, x_i\right) \right) \right]. \tag{7.2}$$

Here $f(x_j, x_i)$ is a known function of the particle positions. Similarly, $f\left(x_j^{im1}, x_i\right)$ and $f\left(x_j^{im2}, x_i\right)$ are known functions of the positions of the images of the particle at x_j and the particle at x_i.

Equation (7.2) represents a system of $3N$ equations with $3N$ unknowns, $\mathbf{p}_i$, which are the modified dipole moments of the particles. The above system is solved using Gauss elimination and the modified electrostatic interaction between the particles is

obtained from equation (1.4). The net electrostatic interaction is then obtained from equation (2.5).

7.3 Results

In this section the results obtained using the method of images for uniform electric field are discussed and they are compared with the results obtained from the point dipole approximation. The simulations are performed in a 3D box shaped domain similar to the one shown in figure 7.1. The domain is discretized using a regular pseudo P2-P1 tetrahedral mesh. The time step used for iterations is $5x10^{-4}$ s. Throughout this paper, we assume that the dynamic fluid viscosity η = 0.01 Poise and the particle diameter and density are 0.2 mm and 1.01 g/cm^3, respectively. The fluid density is ρ_L = 1.0 g/cm^3. Gravity is ignored, as the density of particles is close to that of the fluid and the particle diameter is small. The initial fluid and particle velocities are set to zero.

7.3.1 Two Particle Case

First, a case where two particles are kept in a domain of size 2.4 mm x 0.4 mm x 1.0 mm in the x, y and z directions respectively is discussed. Three cases are considered in which the particles are moved closer and closer to the right side wall.

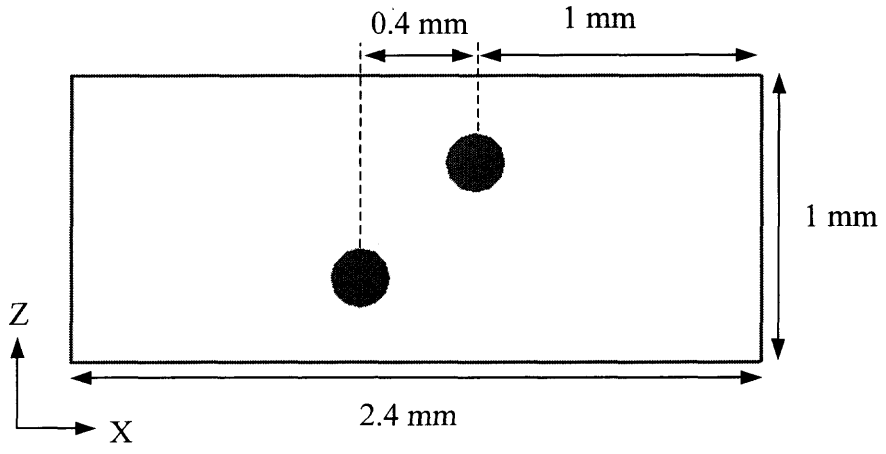

Figure 7.2 Figure showing the initial position of the particles where the right particle is at a distance of 1.0 mm from the right side wall.

In the first case, the initial positions of the particles are (x = 1.0 mm, y = 0.2 mm, z = 0.3 mm) and (x = 1.4 mm, y = 0.2 mm, z = 0.7 mm) respectively as shown in figure 7.2. The x distance of the second particle (right particle) from the right side wall is 1.0 mm. Once the simulation is started the two particles come together in a line parallel to the applied electric field, at z = 0.5 mm and remain stationary as shown in figure 7.3. In moving to their final positions, the particles exhibit both translational and rotational motion, which is due to the force and torque acting on the particles because of the electrostatic interaction. The time required for the particles to come to the final positions is 1.0375 s. The above case is compared to a similar one with only the dipole force acting on the

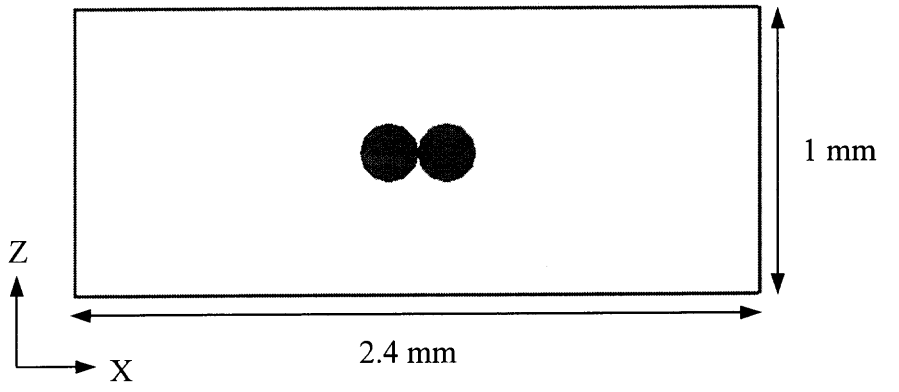

Figure 7.3 Final positions of the particles for the case with particle images. The particles are seen to come together as a chain at $z = 0.5$ mm in the direction of the applied electric field. The chain formation is completed in $t = 1.075$ s.

particles and no images of the particles. In this case also the particles are seen to come together as a chain at z = 0.5 mm, however, the time required by the particles to come together is seen to be 1.055 s, which is 0.0175 s more than that of the case with the images. It can be seen that the difference in time between the case with the images and that without the images is 1.68% of the total time taken by the particles to reach their final positions in the case with images.

Next, the particles are kept at positions (x = 1.4 mm, y = 0.2 mm, z = 0.3 mm) and (x = 1.8 mm, y = 0.2 mm, z = 0.7 mm) respectively as shown in figure 7.4. The right particle is at a distance of 0.6 mm from the right side wall in this case. Here also, once the simulation is started the particles come together in a line parallel to the applied electric field at z = 0.5 mm and then remain stationary. The time required for the particles to reach the final positions is 1.02 s, which is smaller than the first case.

Once again, the above case is compared to a case with just the particles and no images in the domain and the time required for the particles to reach their final positions

is seen to be 1.0625 s, which is more than the time required for the case with the images. Another important factor to be noticed is that the time difference between the case with the images and the case with only the particles, which is 0.0425 s, is more than the previous simulation where the particles were farther away from the right side wall. The difference in time between the case with the images and that without the images is 4.2 % of the total time taken by the particles to reach their final positions in the case with images.

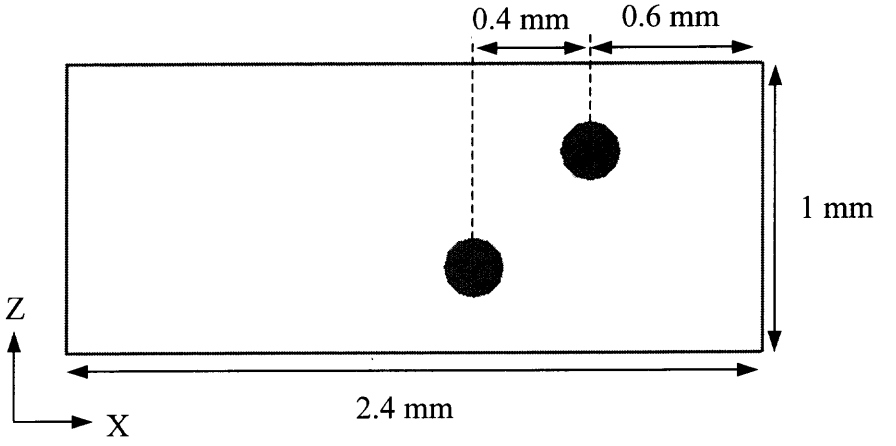

Figure 7.4 Figure showing the initial position of the particles where the right particle is at a distance of 0.6 mm from the right side wall.

Next, simulations are performed with the particles situated at (x = 1.85 mm, y = 0.2 mm, z = 0.3 mm) and (x = 2.25 mm, y = 0.2 mm, z = 0.7 mm) respectively as shown in figure 7.5. This time the right particle is situated only half a radius away from the right wall. In this case we find that the time required by the particles to come together is 0.925 s in the case with images and it is 1.15 s without the images. Again, upon comparison with the previous two cases we find that the time difference between the case with images and without images to arrive at their final positions is 0.225 s, which is more than

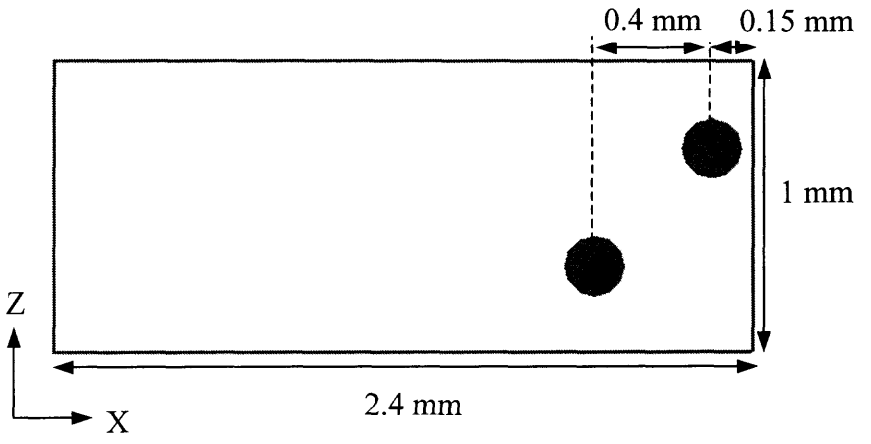

Figure 7.5 Figure showing the initial position of the particles where the right particle is at a distance of 0.05 mm from the right side wall.

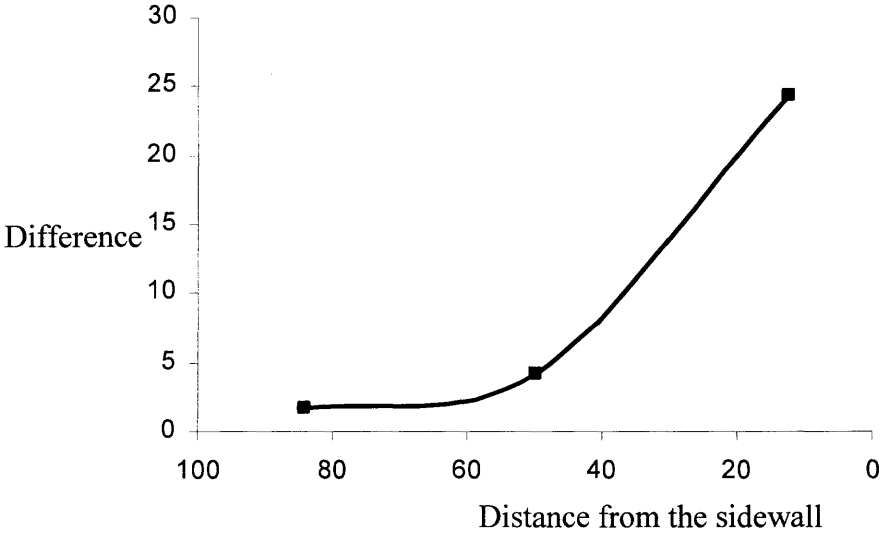

Figure 7.6 Plot showing the difference between the case with the images of the particles included and the case with no images. The dimensionless distance (nondimensionalized using half width of the domain) of a particle from the side wall is plotted on the x axis and the difference between the two methods as a percentage of the total time taken in the case with particle images is plotted in the y axis.

the previous two cases. The difference in time between the case with the images and that without the images can be seen to be 24.3 % of the total time taken by the particles in the

former case to reach their final positions. This shows that the influence of the images become more as the particles move closer to the walls.

A plot of the difference between the two cases, that is the case with the images of the particles included and the case with no images, for decreasing distance from the side wall where the potential boundary condition is applied is shown in figure 7.6.

7.3.2 Thirty Five Particle Case

Next, a case where 35 particles are arranged in a domain of size (1.6 mm x 0.7 mm x 2.1 mm) in a periodic manner is studied. The particles are arranged in the domain as shown in figure 7.7. The solids fraction is 0.062. Here also we compare a case having both

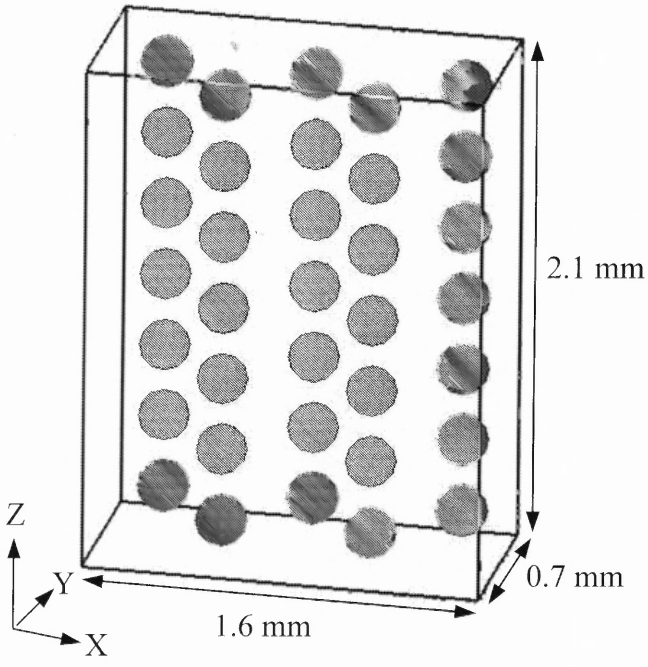

Figure 7.7 Initial periodic arrangement of 35 particles in the domain.

particles and images with a case having only particles and no images. In both the cases the particles are seen to arrange in chains and columns parallel to the external electric field. However, in the first case with images the particles are seen to be forming chains

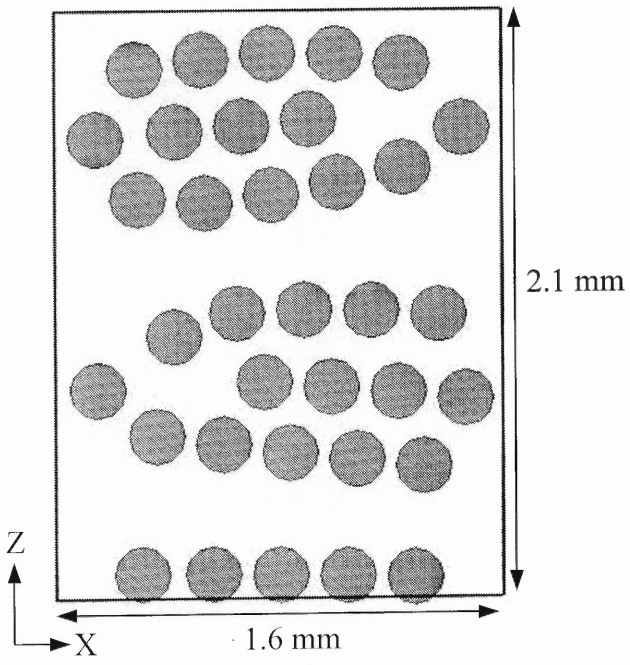

Figure 7.8 Final position of the particles in the case with images at time, $t = 3.75$ s.

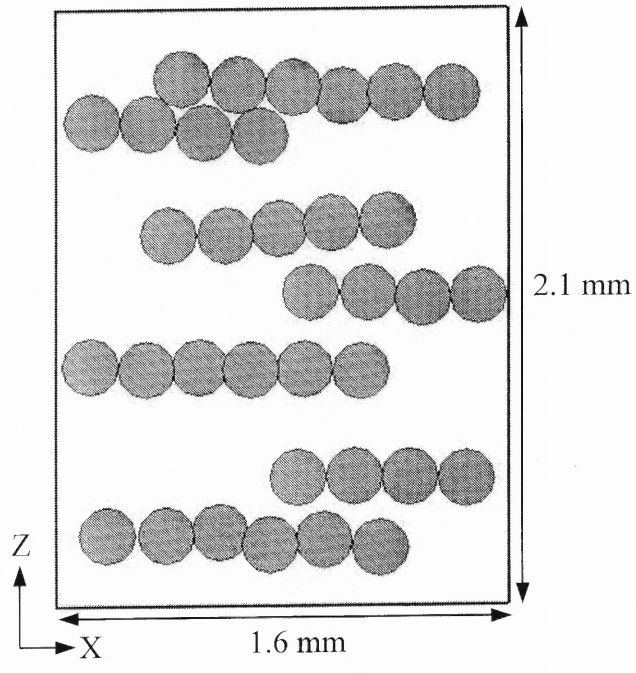

Figure 7.9 Final position of the particles in the case with no images at time, $t = 3.75$ s.

that have two branches which are held by a single particle from the side walls, as seen in figure 7.8, which shows the position of the particles at time t = 3.75 s, indicating that the inter particle interactions are enhanced near the walls due to the images. In the second case without the images the particles are seen to be aligned parallel to the direction of the electric field with out the formation of branches near the wall, as can be seen from figure 7.9, at time t = 3.75 s. In both the cases the chains are seen to form columns with the adjacent chains.

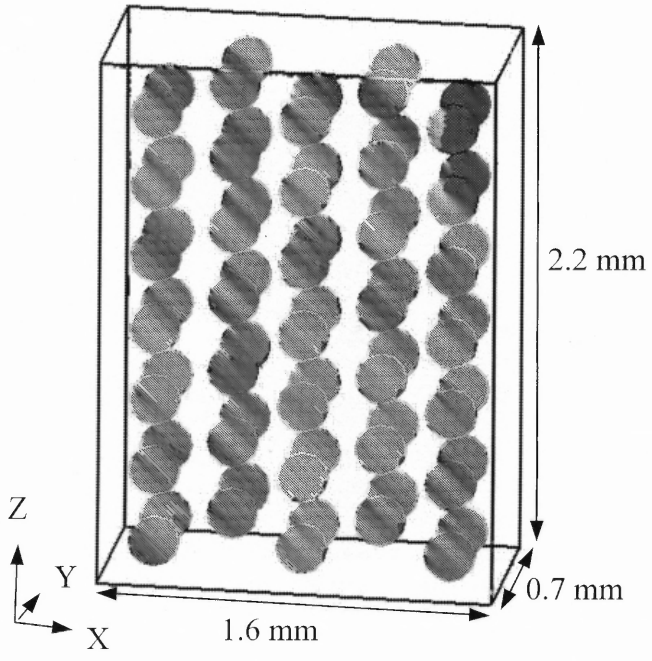

Figure 7.10 The initial periodic arrangement of the particles in the domain of size (1.6 mm x 0.7 mm x 2.2 mm)

7.3.3 Seventy Particle Case

In this section, the results of a case where 70 particles are arranged in a domain of dimensions (1.6 mm x 0.7 mm x 2.2 mm) are discussed.

The particles are arranged in the domain in a periodic manner as shown in figure 7.10. The solids fraction is 0.12. Like in the previous cases, comparison of a case with

particles and images to that of a case with no images is performed here also. It is seen that in the case with images, the particles form chains parallel to the applied electric field faster than the case with no images. The particle positions for both the cases at time, t = 2.0 s are shown in figures 7.11 and 7.12 respectively. From the figures it is clear that in the first case the chains are more organized as straight chains, where as in the second case the particles are organized more as broken chains. With the passage of time, the chains rearrange to form columns in both the cases. However, even the columns formed in the case with only the particles is seen to be less organized and broken than the other case with images. The particle positions at time, t = 4.0 s for the two cases is shown in figure 7.13 and 7.14.

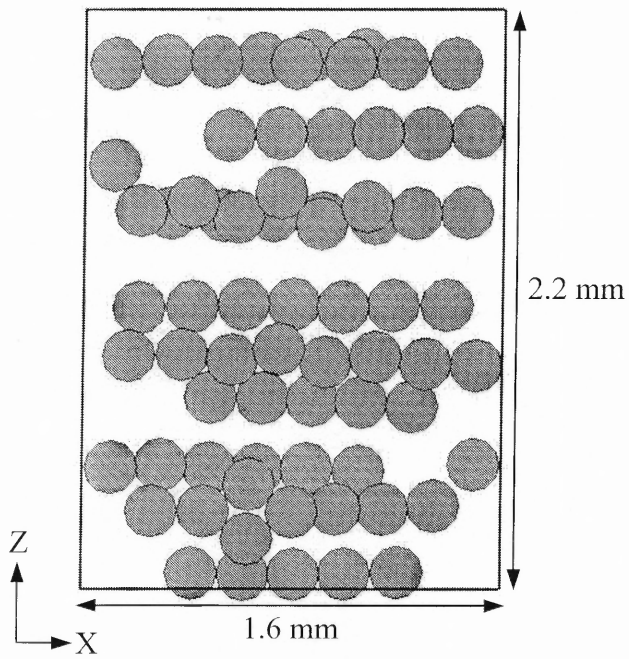

Figure 7.11 The position of the particles in the domain of size (1.6 mm x 0.7 mm x 2.2 mm), for the case with images at time, t = 2.0 s.

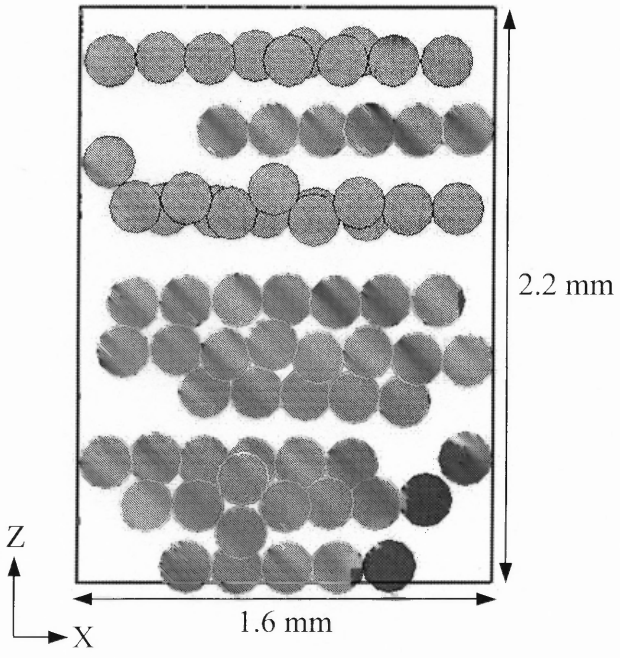

Figure 7. 12 The position of the particles in the domain of size (1.6 mm x 0.7 mm x 2.2 mm), for the case with no images at time, t = 2.0 s.

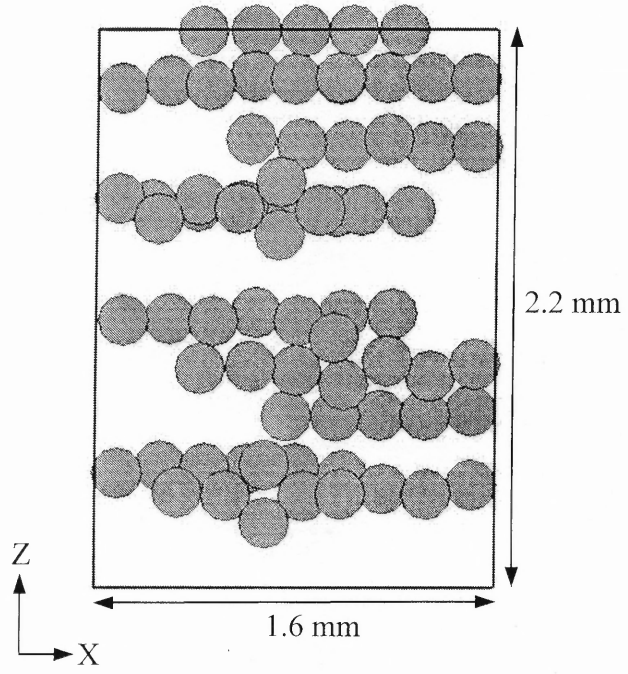

Figure 7.13 The position of the particles in the case with images at time, t = 4.0 s.

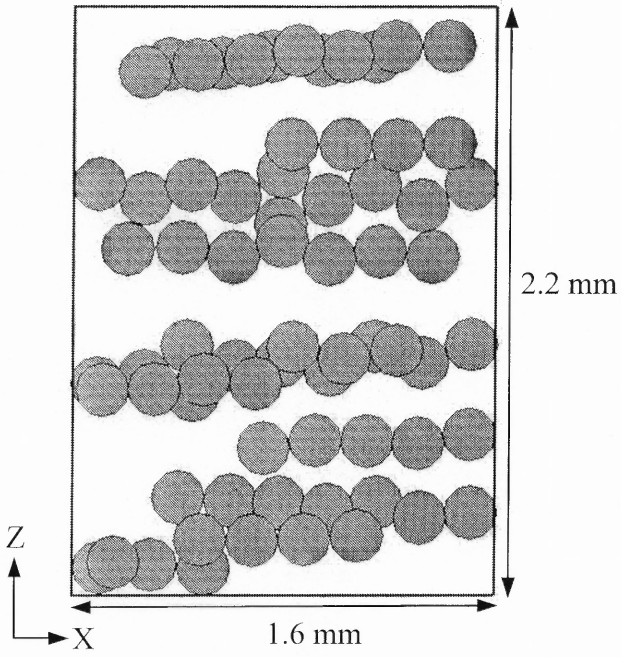

Figure 7.14 The position of the particles in the case with no images at time, t = 4.0 s.

7.4 Discussion

In this chapter the method of images was used to study the time dependent motion of particles when they are placed close to the electrodes. Simulations show that, as expected, the correction due to the method of images increases as the particles move closer to the boundaries where the electric potential boundary conditions are applied. It was seen that when the distance between the particles and wall is less than 10% of the size of the domain, the difference introduced by the images was 24.3%. Also it was seen that for suspensions of low solids fraction of 0.062, the simulation with the images of particles resulted in branched chains and columns with multiple chains of particles being held by single particles from the walls, where as in simulations with no images the particles were seen to form straight chains and columns without any branches. However, for higher

solid fractions this effect was not seen, but the chains and columns formed with the method using images were seen to be more organized and straighter spanning the entire length of the domain than the case with no images where the chains and columns were seen to be broken.

CHAPTER 8

CONCLUSIONS

The main objective of this work was to study the phenomenon of dielectrophoresis and investigate its effectiveness for separating and manipulating particles in applications such as particle separation and collection. The phenomenon has been investigated using both direct numerical simulations and experiments. The DNS approach provides a predictable capability which has been used to understand dynamics at particle scales, as well as to quantify the role of various dimensionless parameters. Experiments are used to qualitatively test the validity of simulations and to investigate the role of AC electroosmotic flow and other effects not included in the DNS approach. The experiments were carried out in microdevices that were manufactured by photolithography processes.

The DNS scheme used for studying the present fluid-particle system is based on the distributed Lagrange multiplier method. In this approach the fluid equations are solved both inside and outside the particle boundaries and rigid body motion is enforced inside the particle boundaries by using the distributed Lagrange multiplier. In the direct numerical scheme used the governing equations for the fluid and particles are solved exactly without using any models, and thus the physics contained in the equations of motion can be extended.

The numerical scheme was tested to ensure that the results converge in both time and space.

The numerical scheme was then used to study the importance of P_4, which is the ratio of the electrostatic particle-particle interactions and the dielectrophoretic force. The

numerical simulations revealed that when this parameter was less than O(1) the particles did not form interparticle chains, instead they moved individually to the regions of high electric field in the case of positive dielectrophoresis and collected there. Where as when this parameter was O(1) the particles formed inter particle chains extending from one electrode to the opposite one, thus entirely clogging the domain. It was not possible to collect or agglomerate the particles at the high electric field regions in this case. The above behavior in the two different regimes is due to the fact that when P_4 is less than O(1), the particle-particle interactions are negligible and the dielectrophoretic force dominates, where as when P_4 is O(1) both the dielectrophoretic force and particle-particle interaction force are comparable in magnitude.

In order to verify that the above results are indeed true and can be reproduced under physical conditions, experiments were conducted using viable yeast cells in MEMS devices. The experiments were conducted in a frequency range where the yeast cells exhibits positive dielectrophoresis. Experiments also showed that at frequencies away from the cross over frequency where the value of Clausius-Mossotti factor is large and thus the value of parameter P_4 is large, yeast cells came together as chains and these chains got collected at the edges of the electrodes, showing strong particle-particle interactions. On the other hand, at frequencies close to the cross over frequency where the value of Clausius-Mossotti factor is small and thus the value of parameter P_4 is small, yeast particles moved to the edges of the electrodes and got collected there without the formation of inter particle chains. These experimental results are in quantitative agreement with the results of numerical simulations.

Another interesting phenomenon studied using the simulation approach was the dielectrophoresis of nanoparticles. The importance of using dielectrophoresis for the manipulation of nanoparticles is increasing as the process involves no touching of the particles and the particles can be guided to any place we desire by adjusting the boundary conditions. The numerical simulation scheme was used to study the behavior of dielectric suspensions of nanoparticles in both uniform and nonuniform electric fields. In the case of uniform electric field it was found that Brownian force is dominant and it will result in the random arrangement of particles in the domain, where as when the Brownian force is absent particles will align themselves in long chains parallel to the electric field. In a nonuniform electric field it was found that the dielectrophoretic force will result in the deterministic motion of particles toward the regions of low or high electric field depending upon their polarities, even though the particle trajectories will be influenced by the Brownian motion. Brownian motion would prevent the particles following the force lines, however; it cannot hinder the particles from being eventually collected.

Simulations performed using the method of images correction to the applied electric field boundary conditions show that in uniform electric fields the influence of the particles on the boundary conditions is significant when the distance between the particle and the domain boundary is of the order of particle size.

In conclusion, an approach based on direct numerical simulation and experiments used here to study the motion and collection of particles in dielectrophoretic devices is optimal in the sense that the simulations allow us to efficiently explore the parameter space and experiments allow us to test the validity of the mathematical equations used for modeling the actual physical system.

REFERENCES

1. Winslow, M. W., (1949). Induced fibration of suspensions, Journal of Applied Physics, **20**, 1137- 1140.

2. Jones, T. B., (1995). Electromechanics of particles, New York City, NY: Cambridge University Press.

3. Pohl, H. A., (1978). Dielectrophoresis, Cambridge: Cambridge university press.

4. Hughes, M. P., and Morgan, H., (1998). Dielectrophoretic trapping of single sub-micrometer scale bioparticles, Journal of Physics D. Applied Physics, 31, 2205-2210.

5. Ramos, A., Morgan, H., Green, N. G., and Castellanos, A., (1998). AC electrokinetics: A Review of forces in microelectrode structures, Journal of Physics D. Applied Physics, 31, 2338-2353.

6. Hughes, M. P., (2000). AC electrokinetics: Applications for Nanotechnology, Nanotechnology, 11, 124-132.

7. Morgan, H., Hughes, M. P., and Green, N. G., (1999). Separation of submicron bioparticles by dielectrophoresis, Biophysical Journal, 77, 516-525.

8. Washizu, M., Kurosawa, O., Arai, I., Suzuki, S., and Shimamoto, N., (1995). Applications of electrostatic stretch and positioning of DNA, IEEE Transactions on Industrial Applications, 31, 447-4356.

9. Voldman, J., (2003). Design and analysis of extruded quadrupolar dielectrophoretic traps, Journal of Electrostatics, 57, 69-90.

10. Green, N. G., Ramos, A., Gonzalez, A., Morgan, H., and Castellanos, A., (2000). Fluid flow induced by nonuniform ac electric fields in electrolytes on microelectrodes. I. Experimental Measurements, Physics Review E, 61, 4011-4018.

11. Glowinski, R., Pan, T-W., Hesla, T. I., and Joseph, D.D., (1999). A distributed Lagrange multiplier/fictitious domain method for particulate flows, International Journal of Multiphase Flow, 25, 755-794.

12. Chen, C.S., and Pohl, H. A., (1974). Biological dielectrophoresis: the behavior of lone cells in a nonuniform electric field, Annals of the New York Academy of Sciences, 238, 176-185.

13. Gvozdiak, P.I., and Chekhovckaia, T.P., (1976). Electroretention of microorganisms, Mikrobiologiya, 45 (5), 901-905.

14. Fomcenko, V.M., and Gavriljuk, B.K., (1977). Dielectrophoresis of cell suspensions, Studia Biophysica 65 (1), 35-46.

15. Fomchenkov, V.M., and Gavrilyuk, B.K., (1978). The study of dielectrophoresis of cells using the optical technique of measuring, Journal of Biological Physics 6 (1-2), 29-68.

16. Glaser, R., Pescheck Ch., and Krause, G., (1979). Dielectro phoresis and preparative separation of cells, Zeitschrift fur Allgemeine Mikrobiologie 19 (9), 601-607.

17. Jones, T.B., and Bliss, G.W., (1977), Bubble dielectrophoresis, Journal of Applied Physics 48 (4), 1412-1417.

18. Jones, T.B., and Kallio, G.A., (1979), Dielectrophoretic levitation of spheres and shells, Journal of Electrostatics 6 (3), 207-224.

19. Zimmermann, U., and Scheurich, P., (1981). Fusion of Avena sativa mesophyll cell protoplasts by electrical breakdown. Biochimica et biophysica acta 641 (1), 160-165.

20. Pohl, H. A., (1982). Biological dielectrophoresis: applications to the determination of the dielectric properties of cells, to cell sorting, and to cell fusion, Conference on Electrical Insulation and Dielectric Phenomena (CEIDP), Annual Report, 71-78.

21. Pohl, H. A., Pollock, and Kent, J., (1983). Dielectrophoretic cell sorting, Electrochemical Society Extended Abstracts, 83-91.

22. Ohno-Shosaku, T., and Okada, Y., (1984). Facilitation of electrofusion of mouse lymphoma cells by the proteolytic action of proteases, Biochemical and Biophysical Research Communications 120 (1), 138-143.

23. Tsoneva, I., Zhelev, D.V., and Dimitrov, D.S., (1984). Electromagnetic fusion of membranes in cell dielectrophoresis, Extended Abstracts, Meeting - International Society of Electrochemistry, 1001-1003.

24. Ruthe, H.-J., and Adler, J., (1985), Fusion of bacterial spheroplasts by electric fields, Biochimica et Biophysica Acta - Biomembranes 819 (1), 105-113.

25. Groth, I., Jacob, H.-E., Kunkel, W., and Berg, H., (1987). Electrofusion of Penicillium protoplasts after dielectrophoresis, Journal of Basic Microbiology 27 (6), 341-344.

26. Glassy, M. C., (1988). Creating hybridomas by electrofusion, Nature 333 (6173), 579-580.

27. Sukharev, S.I., Bandrina, I.N., Barbul, A.I., Fedorova, L.I., Abidor, I.G., and Zelenin, A.V., (1990). Electrofusion of fibroblasts on the porous membrane, Biochimica et Biophysica Acta - General Subjects 1034 (2), 125-131.

28. Arnold, W.M., and Zimmermann, U., (1988). Electro-rotation: development of a technique for the dielectric measurements of individual cells and particles, Journal of Electrostatics 21 (2-3), 151-191.

29. Gherardi, L., Mognaschi, E.R., and Savini, A., (1985). Dielectrophoretic motion of a lossy dielectric sphere in a liquid of non-zero conductivity, IEEE Transactions on Electrical Insulation EI-20 (2), 385-388.

30. Mognaschi, E.R., and Antonio, S., (1985). Dielectrophoresis of lossy dielectrics, IEEE Transactions on Industry Applications IA-21 (4), 926-929.

31. Goossens, K., and Van Biesen, L., (1988). Computer-aided analysis of dielectrophoretic force calculations, IEE Conference Publication (289), 131-134.

32. Henry, F.S., and Teoman, A., (1986). Numerical calculation of particle collection in electrically enhanced fibrous filters, Particulate Science and Technology 4 (4), 455-477.

33. Adamson, Richard J., and Kaler, Karan V.I.S., (1988). Automated stream-centered dielectrophoretic system, IEEE Transactions on Industry Applications 24 (1), 93-98.

34. Masuda, S., Washizu, M., and Nanba, T., (1989). Novel method of cell fusion in field constriction area in fluid integrated circuit, IEEE Transactions on Industry Applications 25 (4), 732-737.

35. Washizu, M., and Kurosawa, O., (1990) Electrostatic manipulation of DNA in microfabricated structures, IEEE Transactions on Industry Applications 26 (6), 1165-1172.

36. Masuda, S., Washizu, M., and Nanba, T., (1990). Handling biological cells using a fluid integrated circuit, IEEE Transactions on Industry Applications 26(2), 352-358.

37. Pethig, R., (1984). Dielectric properties of biological materials: biophysical and medical applications, IEEE Transactions on Electrical Insulation EI-19 (5), 453-474.

38. Gascoyne, P. R. C., Huang, Y., Pethig, R., Vykoukal, J., and Becker, F. F., (1992). Dielectrophoretic separation of mammalian cells studied by computerized image analysis, Measurement Science and Technology 3 (5), 439-445.

39. Huang, Y., and Pethig, R., (1991). Electrode design for negative dielectrophoresis, Measurement Science and technology, 2, 1142-1146.

40. Price, J., A., Burt, J. P. H., and Pethig, R., (1998). Applications of a new optical technique for measuring the dielectrophoretic behavior of micro organisms, Biochimica et Biophsica acta, 964, 221-230.

41. Pethig, R., Huang, Y., Wang, X-B., and Burt, J. P. H., (1992). Positive and negative dielectrophoretic collection of colloidal particles using interdigitated castellated microelectrodes, Journal of Physics D: Applied Physics, 25, 881-888.

42. Wang, X-B., Huang, Y., Burt, J.P.H., Markx, G.H., and Pethig, R., (1993). Selective dielectrophoretic confinement of bioparticles in potential energy wells Journal of Physics D: Applied Physics 26 (8), 1278-1285.

43. Wang, X-B., Huang, Y., Holzel, R., Burt, J. P. H., and Pethig R., (1993) Theoretical and experimental investigations of the interdependence of the dielectric, dielectrophoretic and electrorotational behavior of colloidal particles, Journal of Physics D: Applied Physics 26, 312-322.

44. Wang, X-B., Pethig, R., and Jones, T.B., (1991). Relationship of dielectrophoretic and electrorotational behaviour exhibited by polarized particles, Journal of Physics D: Applied Physics, 25, 905-912.

45. Huang, Y., Holzel. R, Pethig, R., and Wang, X-B., (1992). Differences in AC electrodynamics of viable and non-viable yeast cells determined through combined dielectrophoresis and electrorotation studies, Physics in medicine and biology, 37 (7), 1499-1517.

46. Fuhr, G., Schnelle, T., and Wagner, B., (1994). Travelling-wave driven micro fabricated electrohydrodynamic pumps for liquids, Journal of Micromechanics and Microengineering, 4, 217-226.

47. Fuhr, G., Fiedler, S., Müller, T., Schnelle, T., Glasser, H., Lisec, T., and Wagner, B., (1994). Particle micromanipulator consisting of two orthogonal channels with travelling-wave electrode structures, Sensors and Actuators A, 41-42, 230-239.

48. Hagedorn, R., Fuhr, G., Muller, T., and Gimsa, J., (1992). Traveling-wave dielectrophoresis of microparticles, Electrophoresis 13 (1-2), 49-54.

49. Batchelder, J. S., (1983). Dielectrophoretic manipulator, Review of Scientific Instruments, 54, 300-302.

50. Huang, Y., Wang, X –B., Tame, J. A., and Pethig, R., (1993). Electrokinetic behavior of colloidal particles in traveling electric fields: studies using yeast cells, Journal of Physics D: Applied Physics, 26, 1528-1535.

51. Wang, X –B., Huang, Y., Becker, F. F., and Gascoyne, P. R. C., (1994). A unified theory of dielectrophoresis and traveling wave dielectrophoresis, Journal of Physics D: Applied Physics, 27, 1571-1574.

52. Talary, M. S., Burt, J. P. H., Tame, J. A., and Pethig, R., (1996). Electromanipulation and separation of cells using traveling wave electric fields, Journal of Physics D: Applied Physics, 29, 2198-2203.

53. Hughes, M. P., Pethig, R., and Wang, X-B., (1996). Dielectrophoretic forces on particles in traveling wave electric fields, Journal of Physics D: Applied Physics, 29, 474-482.

54. Washizu, M., and Jones, T.B., (1994). Multipolar dielectrophoretic force calculation, Journal of Electrostatics 33 (2), 187-198.

55. Jones, T.B., and Washizu, M., (1996). Multipolar dielectrophoretic and electrorotation theory, Journal of Electrostatics 37 (1-2), 121-134.

56. Washizu, M., Jones, T.B., (1996). Generalized multipolar dielectrophoretic force and electrorotational torque calculation, Journal of Electrostatics 38 (3), 199-211.

57. Gunji, M., Washizu, M., and Jones, T. B., (2000). Dielectrophoretic microfluidic devices, Proceedings of IEJ/ESA Joint Symposium on Electrostatics, Kyoto, Japan, September, 2000, 78-87.

58. Jones, T. B., (2004). Electrostatics and the Lab on a Chip, Institute of Physics Conference Series, 178, 1-10.

59. Jones, T. B., (2003). Influence of scale on electrostatic forces and torques in AC particulate electrokinetics, IEE Proc. Nanobiotechnology, 150, 39-46.

60. Gunji, M., Washizu, M., Feldman, M., J., and Jones, T. B., (2001). Dielectrophoretic liquid actuation and nanodroplet formation, Journal of Applied Physics, 89, 1441-1448.

61. Gunji, M., Washizu, M., and Jones, T. B., (2001). DEP Microactuation of Liquids, Proceedings of IEEE MEMS Conference, 385-388.

62. Burt, J.P.H., Pethig, R., Gascoyne, P.R.C., and Becker, F.F., (1990). Dielectrophoretic characterisation of Friend murine erythroleukaemic cells as a measure of induced differentiation, Biochimica et Biophysica Acta, 1034, 93-101.

63. Becker, F.F., Wang, X-B., Huang, Y., Pethig, R., and Vykoukal, J., (1994). The removal of human leukaemia cells from blood using interdigitated microelectrodes, Journal of Physics D: Applied Physics, 27, 2659-2662.

64. Becker, F.F., Wang, X-B., Huang, Y., Pethig, R., Vykoukal, J., and Gascoyne, P.R.C., (1995). Separation of human breast cancer cells from blood by differential dielectric affinity, Proceedings of the National Academy of Science, USA. 92, 860-864.

65. Gascoyne, P.R.C., Wang, X-B., Huang Y., and Becker, F.F., (1997). Dielectrophoretic separation of cancer cells from blood, IEEE Industrial Application Society, 33(3), 660-669.

66. Gascoyne, P.R.C., Huang, Y., Hughes, M.P., Wang, X-B., Pethig, R., and Becker, F.F., (1994). Manipulation of erythroleukemia cells using travelling electric fields, Proceedings of IEEE EMBS., 16, 772-773.

67. Wang, X-B., Huang Y., Gascoyne, P.R.C., and Becker, F.F., (1994). Particle dipole-dipole interactions in AC electric fields, Proceedings of IEEE EMBS., 16, 774-775.

68. Wang, X., Wang, X-B., and Gascoyne, P.R.C., (1997). General expressions for dielectrophoretic force and electrorotational torque derived using the Maxwell stress tensor method, Journal of Electrostatics, 39, 277-295.

69. Huang, Y., Wang, X-B., Becker, F.F., and Gascoyne, P.R.C., (1997). Introducing dielectrophoresis as a new force field for field-flow fractionation, Biophysical Journal, 73, 1118-1129.

70. Gascoyne, P.R.C., Wang, X-B, Vykoukal, J., Ackler, H., Swierkowski, S., and Krulevitch, P., (1998). A microfluidic device combining dielectrophoresis and field flow fractionation for particle and cell discrimination, Proceedings of Solid-State Sensor and Actuator Workshop, Hilton Head Island, South Carolina, June 8-11.

71. Yang, J., Huang, Y., Wang, X-B., Becker, F.F. and Gascoyne, P.R.C., (1999). Cell separation on microfabricated electrodes using dielectrophoretic/gravitational field-flow- fractionation, Analytical Chemistry, 71(5), 911-918.

72. Wang, X-B., Huang, Y., Vykoukal, J., Becker, F.F. andGascoyne, P.R.C., (2000). Cell separation by dielectrophoretic field-flow-fractionation, Analytical Chemistry, 72(4), 832-839.

73. Vykoukal, J., Gascoyne, P.R.C., Weinstein, R., Gandini, A., Parks, D., and Sawh, R., (2002). Magnetophoretic-Dielectrophoretic Field-Flow Fractionation, Micro Total Analysis Systems 2002: Vol I, Y. Baba et al. (eds) (Kluwer Academic Publishers, The Netherlands, 323-325.

74. Gascoyne, P.R.C., Vykoukal, J.V., Anderson , T., Noshari, J., Becker, F.F., Ratanachoo, K., Kandjanapa, K., Satayavivad, J. and Ruchirawat, M., (2003). Programmable dielectrophoretic μTAS sample handling, Micro Total Analysis Systems: Vol 2, M.A. Northrup, K. Jensen and J. Harrison (eds) (Transducers Research Foundation, Cleveland Heights, Ohio, 919-922.

75. Vykoukal, J. and Gascoyne, P.R.C., (2004), Dielectrophoretic Concepts for Automated Diagnostic Instruments, Proceedings of IEEE, 92(1), 22-42.

76. Morgan, H., Hughes, M. P., and Green, N. G., (1999). Separation of submicron bioparticles by dielectrophoresis, Biophysical Journal, 77, 516-525.

77. Hughes, M. P., and Morgan, H., (1998). Dielectrophoretic trapping of single sub-micrometer scale bioparticles, Journal of Physics D. Applied Physics, 31, 2205-2210.

78. Green, N. G., and Morgan, H., (1998). Separation of submicron particles using a combination of dielectrophoretic and hydrodynamic forces, Journal of Physics D. Applied Physics, 31, L25-L30.

79. Green, N. G., Ramos, A., and Morgan, H., (2000). AC electrokinetics: a survey of submicrometer bioparticles, Journal of Physics D. Applied Physics , 33, 632-641.

80. Green, N. G., Ramos, A., Gonzalez, A., Morgan, H., Castellanos, A., (2000). Fluid flow induced by nonuniform ac electric fields in electrolytes on microelectrodes. I. Experimental Measurements, Physics Review E, 61, 4011-4018.

81. Gonzalez, A., Ramos, A., Green, N. G., Castellanos, A., and Morgan, H., (2000). Fluid flow induced by nonuniform ac electric fields in electrolytes on microelectrodes. II. A linear double layer analysis, Physics Review E, 61, 4019-4028.

82. Green, N. G., Ramos, A., Gonzalez, A., Morgan, H., and Castellanos, A., (2000). Fluid flow induced by nonuniform ac electric fields in electrolytes on microelectrodes. III. Observation of stream lines and numerical simulation, Physics Review E, 66, 1-11.

83. Castellanos, A., Ramos, A., Gonzalez, A., Green, N. G., Morgan, H., (2003). Elecrohydodnamics and dielectrophoresis in Microsystems: scaling laws, Journal of Physics D. Applied Physics, 36, 2584-2597.

84. Hughes, M. P., (2000). AC electrokinetics: Applications for Nanotechnology, Nanotechnology, 11, 124-132.

85. Schwarz, G., (1963). General expression for the mean electrical energy of a dielectric body in an alternating electric field, Journal of Chemical Physics, 39, 2387.

86. Sher, L. D., (1968). Dielectrophoresis in lossy dielectric media, Nature, 220, 695.

87. Jones, T. B., (1979). Dielectrophoretic force calculation, Journal of electrostatics, 6, 69-82.

88. Sauer, F. A, in: Frohlich, H., Kremer, F., (Eds.), (1983). Coherent excitations in biological systems, Springer, Berlin.

89. Sauer, F. A, Schlogl, R. W., in: Chiabrera, A., Nicolini, C., Schwan, H. P., (Eds.),(1985). Interactions between electromagnetic fields and cells, Plenum Publications Co., New York.

90. Hughes, M.P., Wang, X.B., Burt, J.P.H., Pethig, R., and Watkins, L.R., (1994). Simulation of traveling electric field manipulation of bioparticles, IEEE Conference Publication, 384, 48-51.

91. Leonardi, A., Medoro, G., Manaresi, N., Tartagni, M., and Guerrieri, R., (2002). Simulation methodology for dielectrophoresis in microelectronic Lab-on-a-chip, International Conference on Computational Nanoscience and Nanotechnology - ICCN 2002, 107-110.

92. Green, N.G., Ramos, A., and Morgan, H., (2002). Numerical solution of the dielectrophoretic and travelling wave forces for interdigitated electrode arrays using the finite element method, Journal of Electrostatics, 56, 235–254.

93. Li, H., and Bashir, R., (2004). On the Design and Optimization of Micro-Fluidic Dielectrophoretic Devices: A Dynamic Simulation Study, Biomedical Microdevices, 6, 289–295.

94. Qiu, Z., Markarian, N., Khusid, B., and Acrivos, A., (2002). Positive dielectrophoresis and heterogeneous aggregation in high gradient ac electric fields, Journal of Applied Physics, 92, 2829-2843.

95. Morgan, H., Holmes, D., Green, N. G., (2003). 3D focusing of nanoparticles in microfluidic channels, IEE Proceedings – Nanobiotechnology, 150, 76-82.

96. Singh, P., Joseph, D. D., Hesla, T. I., Glowinski, R. T. and Pan, W., (2000). A distributed Lagrange multiplier/fictitious domain method for particulate flows, Journal of Non-Newtonian Fluid Mechanics, 91, 165-188.

97. Kadaksham, J., Singh, P., and Aubry, N., (2004). Dynamics of electrorheological suspensions subjected to spatially varying electric fields, Journal of Fluids Engineering, 126, 170 –179.

98. Kadaksham, J., Singh, P., and Aubry, N., (2004). Manipulation of particles using dielectrophoresis, Mechanics Research Communications, to appear.

99. Kadaksham, J., Singh, P., and Aubry, N., (2004). Dielectrophoresis of nanoparticles, Electrophoresis, 25, 3625-3632.

100. Vykoukal, J., and Gascoyne, P.R.C., (2002). Particle separation by dielectrophoresis, Electrophoresis, 23, 1973-1983.

101. Ermak, D. L., and McCammon, J. A., (1978). Brownain dynamics with hydrodynamic interactions, Journal of Chemical Physics, 69, 1352-1360.

102. Climent, E., Maxey, M. R., and Karniadakis, G. E., (2004). Dynamics of self-assembled chaining in magnetorheological fluids, Langmuir, 20, 507-513.

103. Parthasarathy, M., Klingenberg, D. J.,(1996). Electrorheology: Mechanisms and models, Material Science and Engineering, R17, 57-103.

104. Klingenberg, D. J., van Swol, S., Zukoski, C. F., (1989). Simulation of electrorheological suspensions, Journal of Chemical Physics, 91, 7888-7895.

105. Tao, R., Jiang Qi., (1994). Simulation of structure formation in an electrorheological fluid, Physics Review Letters, 73, 205-208.

106. Anderson, R. A., (1994). Electrostatic forces in an ideal spherical-particle Electrorheological fluid, Langmuir, 10, 2917-2928.

107. Klingenberg, D. J., van Swol, S., Zukoski, C. F., (1991). The small shear rate response of electrorheological suspensions. I. Simulation in the point-dipole limit, Journal of Chemical Physics, 94, 6160-6167.

108. Huang, J. P., Yu, K. W., (2004). Interparticle force in Elctrorheological solids: Many body dipole-induced dipole model, Physics Review E, 70, 1-5.

109. Lindell, I.V., Nikoskinen, K.I., (2001). Electrostatic image theory for the dielectric prolate spheroid, Journal of Electromagnetic Waves and Applications, 15, 1075-1096.